Utah State University
DigitalCommons@USU

All Graduate Theses and Dissertations | Graduate Studies

5-2007

Rayleigh-Scatter Lidar Observations at USU's Atmospheric Lidar Observatory (Logan,UT) - Temperature Climatology, Temperature Comparisons with MSIS, and Noctilucent Clouds

Joshua P. Herron
Utah State University

Follow this and additional works at: https://digitalcommons.usu.edu/etd

 Part of the Physics Commons

Recommended Citation

Herron, Joshua P., "Rayleigh-Scatter Lidar Observations at USU's Atmospheric Lidar Observatory (Logan,UT) - Temperature Climatology, Temperature Comparisons with MSIS, and Noctilucent Clouds" (2007). *All Graduate Theses and Dissertations*. 4686.
https://digitalcommons.usu.edu/etd/4686

This Dissertation is brought to you for free and open access by the Graduate Studies at DigitalCommons@USU. It has been accepted for inclusion in All Graduate Theses and Dissertations by an authorized administrator of DigitalCommons@USU. For more information, please contact digitalcommons@usu.edu.



RAYLEIGH-SCATTER LIDAR OBSERVATIONS AT USU'S ATMOSPHERIC LIDAR OBSERVATORY (LOGAN, UT)—TEMPERATURE CLIMATOLOGY, TEMPERATURE COMPARISONS WITH MSIS, AND NOCTILUCENT CLOUDS

by

Joshua P. Herron

A dissertation submitted in partial fulfillment
of the requirements for the degree

of

DOCTOR OF PHILOSOPHY

in

Physics

UTAH STATE UNIVERSITY
Logan, Utah

2007

Copyright © Joshua P. Herron 2007

All rights Reserved

ABSTRACT

Rayleigh-Scatter Lidar Observations at USU's Atmospheric Lidar Observatory (Logan, UT)—Temperature Climatology, Temperature Comparisons with MSIS, and Noctilucent Clouds

by

Joshua P. Herron, Doctor of Philosophy

Utah State University, 2007

Major Professor: Dr. Vincent B. Wickwar
Department: Physics

The Earth's atmosphere is typically characterized by its temperature structure, which naturally divides the atmosphere into several discrete regions. They are in order of increasing altitude the troposphere, stratosphere, mesosphere, and thermosphere. The first layer and a large portion of the second layer of the Earth's atmosphere are routinely measured via weather balloons that are launched twice daily around the globe. Satellites and their development have motivated the study of the thermosphere. It is the middle region of the Earth atmosphere, which is mainly composed of the mesosphere that lacks routine in situ measurements. Routine observations are therefore carried out via remote sensing. Ground-based instruments typically provide high resolution measurements of the atmosphere over a single point on the globe and space-based instrument capture a global picture at lower resolution.

A Rayleigh-scatter lidar has been in operation at Utah State University (41.7°N 111.8°N) starting in September 1993. Observations have continued from that point until the present when funding and observing conditions have permitted. Under normal observational conditions the backscattered photons are proportional to the atmospheric density. These relative density profiles can be used to derive absolute temperature profiles over much of the middle atmosphere. The resulting 11 years of temperature profiles have been combined into a single composite year which contains ~900 nights and ~5000 hours of observations. This climatology was compared to the mid-latitude climatology from the French lidar group at Haute Provence and relatively good agreement was obtained. It was also compared to the NRL MSIS empirical model to explore the model's validity at mid-latitudes. Some significant differences were found.

The coldest atmospheric temperatures are found at the mesopause near the summer solstice. Small ice crystals formed in this region and can grow to form noctilucent clouds (NLC) which are the highest naturally occurring clouds in the atmosphere. Previously, NLC observations have been limited to the region poleward of 50° but NLCs have been observed with the ALO lidar on two occasions. Their formation has been attributed to atmospheric dynamics, a large amplitude wave, rather than a general cooling of the atmosphere.

(173 pages)

ACKNOWLEDGMENTS

I would like to thank my major professor, Dr. Wickwar, for all of the time and support he has given in the completion of my dissertation. Foremost, I would like to thank Ann, my wife, for her love and support over the course of my graduate work. Her support has never been more evident than during the last year with the adoption of our daughter Elizabeth, who has brought such joy to our lives. I would also like to thank my parents for beginning my education early and allowing me to explore the world around me, and to thank them for putting up with the mischief that I caused in doing so.

I would also like the dedicated group of students students past and present for their time spent in making observations: Brian Anderson, Allyson Bares, Angela Bodrero Beecher, Kayla Brown, Nathan Bunderson, Courtney Butler, Casey Clegg, Steve Collins, Joel Drake, Scott Elkington, Will Fredin, Spencer Fuller, Joshua Herron, John James, Teresa Jones, Jeffrey Leek, Eric Lundell, John Maloney, Bethany Martineau, Dusty McEwen, Ian Monson, Patrick Neary, Karen Marchant Nelson, Spencer Nelson, Antony Pearson, Robert Ream, Ryan Smith, Joseph Andy Spencer, Kristina Thomas, Ashley Turner, Marie Westbrook, and Troy Wynn. Some of the equipment, without which we could not have made the observations, was made available by John Meriwether of Clemson University and Thomas Wilkerson of the University of Maryland and then of Utah State University.

This work was supported in part by Utah State University, NSF Grants ATM-0123145 and ATM-0531397, and a scholarship from the Rocky Mountain NASA Space Consortium. The data were acquired in part with support from Utah State University, several CEDAR grants from the Atmospheric Science Division of the NSF, and NASA

OSS grant NAG5-5022. I greatly appreciate Dr. Maura Hagen making the GSWM-00 tidal results available on the web.

Joshua P. Herron

CONTENTS

Page

ABSTRACT iii

ACKNOWLEDGMENTS vi

LIST OF TABLES x

LIST OF FIGURES xi

CHAPTER

1. INTRODUCTION 1

    Statement of Problem 2
    Overview 11

2. RAYLEIGH-SCATTER LIDAR SYSTEM 13

    Lidar Transmitter 13
    Lidar Receiver 17
    Data Acquisition System 22
    Relative Density Measurements 24
    Absolute Temperatures 25
    Measurement Uncertainty 27
    NLC Observations and Uncertainties 32

3. Mid-Latitude Mesospheric Temperature Climatology in the Mountain West Obtained from the Rayleigh-scatter Lidar at the Atmospheric Lidar Observatory (41.7° N, 111.8° W) 36

    Abstract 36
    Introduction 37
    Instrument Description and Data Analysis 38
    Observations and Comparisons 42
    Discussion and Conclusion 50

4. A Comparison of Mid-Latitude Mesospheric Temperatures — The ALO lidar Climatology and The NRL Empirical Model 56

    Abstract 56
    Introduction 57

Atmospheric Lidar Observatory 59

Rayleigh-scatter lidar 59
ALO Climatology 62

MSIS–00 Empirical Model 65

MSIS–00 Model Description 65
MSIS–00 Model Composite Year 67

Comparison of Composite Years 69

Temperature Differences 69
Annual, Semi-Annual, and higher order cycles 72

Discussion and Conclusion 77

5. Observations of a Noctilucent Cloud Above Logan Utah (41.7° N, 111.8° W) IN 1995 83

Abstract 83
Introduction 84
Instrument Description and Data Reduction 84
Observations and Data Analysis 86
Discussion 100

NLC Characteristics 100
Relationship between the NLC and Climate Change 104
Comparison of Large Amplitude Wave and Tides 106

Conclusions 109

6. Summary and Future Work 113

Summary and Conclusions 113
Future Work 118

REFERENCES 123

APPENDICES 132

APPENDIX A 133

APPENDIX B 136

CURRICULUM VITAE..... 167

LIST OF TABLES

Table Page

1. Monthly distribution of nightly observations included in the climatology..... 40

LIST OF FIGURES

Figure — Page

1. Idealized weighting function for a radiance measurement from above [Taylor, 2005]. 5

2. (a) Diagram of Limb scanning measurement at some arbitrary tangent height. (b) An example of the weighting function used for limb measurements [Taylor, 2005]. 6

3. The temperature profiles of the neutral atmosphere. Several of the observational techniques and atmospheric phenomena are illustrated. Note the range of the Rayleigh lidar technique and the radar gap in the middle atmosphere. 7

4. Simplified diagram of the USU Rayleigh-scatter lidar diagram. The 532nm light is illustrated in green with the 1064 in red. The dotted red line is the residual 1064 nm light hat is virtually eliminated from being transmitted by the second dielectric mirror. The laser output is directed vertical along with the field of view of the telescope but have been depicted horizontally for simplicity. 18

5. Transmission profile of the 532nm interference filter. The FWHM of the filter is approximately 1 nm. 19

6. Diagram of a 12 stage linear focus photomultiplier tube. Here the rolls quantum efficiency, QE, and collection efficiency, CE, are illustrated along with the individual dynodes. 20

7. Nighttime temperature averages, collected during the months of January and July. The horizontal error bars are the standard deviation plotted about the average temperature. 41

8. The ALO temperature climatology. The profile for each day of the composite year is the result of a multi-year, nighttime, temperature average over a 31-day window centered on the day. The vertical black lines represent the 15th of each month. 42

9. The ALO temperature climatology from Figure 8 presented at 3-km intervals for the 15th of each month. The contour lines are every 5 k. 44

10. Monthly temperature profiles. Each is the average of the nighttime temperatures in a multi-year, 31-day window. The error bars are derived from the measurement uncertainty assuming Poisson statistics. The annual temperature profile, obtained from averaging the monthly profiles, is also presented. 46

11. The ALO climatology of observed temperature standard deviations presented at 3-km intervals for the 15th of each month. The contour lines are every 2 K..... 48

12. Temperature differences between the ALO and the French climatologies presented at 3-km intervals for the 15th of each month. The contour lines are every 1 K..... 49

13. Data collected on 95-07-14 (a) is a nighttime average of the lidar photocount profiles. The opening of the mechanical shutter is visible along with the change of the PMT gain near 38 km. The Rayleigh-scatter region along with the background region is also indicated. The black curve is the average photocount profile with the associated error bars. (b) Average temperature profile with associated error bars for the night's observations. (c) Uncertainty for the temperature profile, (b), are given separately shows the strong altitude dependence of the uncertainties..... 61

14. The ALO temperature climatology. The profile for each day of the composite year is the result of a multi-year, nighttime, temperature average over a 31-day window centered on the day. Contour lines are every 5 K..... 63

15. An average of the standard deviation of the mean for the year composes plot (a). The contour plot is composed of the standard deviation of the mean for each 31-day period..... 66

16. MSIS–00 composite nighttime year. The profile for each day of the composite year is the result of a nighttime temperature average over a 31-day window centered on the day. Contour lines are every 5 K..... 68

17. ALO/MSIS–00 temperature differences. (a) Average annual temperature difference. (b) The MSIS–00 composite year temperatures have the ALO climatology subtracted from them. Contour lines are every 5 K. Blue indicates regions where MSIS is cooler than ALO and red warmer..... 71

18. The annual and semi-annual amplitudes and phases for the ALO and MSIS composite years. The red curves correspond to results from ALO and the blue curves to MSIS. The annual amplitude is shown in (a) with the phase given in (b). Likewise for the semi-annual oscillation the amplitude is shown in (c) and the phase in (d). The associated error bars are the uncertainties from the fitting routine..... 74

19. The 4-month, 3-month, and 2.4-month oscillations in the composite years. The red curves indicate the ALO climatology and blue indicate the MSIS–00 model. The amplitudes are given on the left with the phase on the right. The 4-month amplitude and phase are given in plots (a-b), 3-month in (c-d), and the 2.4-month

cycle in (e-f). The associated error bars are the uncertainties generated from the fitting routine. 76

20. The NLC enhancement on 22 June 1995 at ALO seen in the profiles of relative density (a) and the backscatter ratio (b). The data were averaged over 12 minutes, centered on 8:13 UT, and over 150 m. However, data points are plotted every 37.5 m. The uncertainties are based on the measurements, assuming Poisson statistics. 88

21. Backscatter ratios for the 22 June 1995 NLC. The inputs for the contour plot were created every 2 minutes using a 2-D running average with a width of 12 minutes and a height of 150 m applied to the raw data, which were measured every 2 minutes and every 37.5 m. A backscatter ratio of 1 indicates that there is no Mie-scatter enhancement. The time is in hours. 90

22. Backscatter ratios for the 1999 NLC [*Wickwar et al.*, 2002] analyzed and presented in the same way as for the 1995 NLC in Figure 21. It is at a lower altitude and the maximum backscatter ratio is smaller. 91

23. Relative density profiles before (4a) and during the NLC (4b). The thick black curves are the measured number density profiles; the thin red curves are the result of a 3rd order polynomial fitted to data in 3-km regions immediately above and below the NLC and then applied across the 3-km region in between. A 3-km running average was applied to both the measured number density profile and the profile with the polynomial fit. See the text for details about the fitting procedure. 93

24. Temperature profiles before, during, and after the NLC on 22 June 1995. Period 1 is for 6:30-8:00 UT, period 2 for 8:00-9:00 UT, and period 3 for 9:00-10:56. The fourth profile is the average June temperature from the ALO climatology, see Chapter 3. The corresponding density profiles for periods 1 and 2, from which the temperatures were derived, are shown in Figure 23. 94

25. Temperature differences between the observed values on 22 June 1995 and the climatological June average for ALO. The temperature profiles are from Figure 5. 96

26. Nighttime OH rotational temperatures at ~87 km from the Michelson Interferometer located at USU. The red curve denotes the values from 1995; the blue curve denotes those from 1996. The NLC night is identified. 98

27. OH rotational temperatures at ~87 km for the night of 22 June 1995. In addition, the time period when the lidar was operated is indicated in black and when the NLC was observed is indicated in grey. 100

28. Amplitude and phase of the diurnal tide compared to the NLC. The tidal results were derived from the CSU sodium lidar measurements [*She et al.*, 2002], Urbana sodium lidar measurements [*States and Gardner*, 2000], and GSWM-00 model calculations [*Hagan et al.*, 1999, 2001]. Local solar midnight corresponds to 7:27 UT. 106

29. Amplitude and phase of the semi-diurnal tides in relation to the NLC occurrence. The tidal results are derived from the CSU sodium lidar measurements [She et al., 2002], Urbana sodium lidar measurements [States and Gardner, 2000], and GSWM-00 model calculations [*Hagan et al.*, 1999, 2001]. The model values had to be multiplied by 10 to use the same scale as the two sets of observations. Local solar midnight corresponds to 7:27 UT. 107

CHAPTER 1

INTRODUCTION

The Rayleigh-scatter lidar technique has proven itself to be a powerful technique for measurements in the middle atmosphere. Routine observations of absolute temperature and relative density are possible over much of the middle atmosphere. The temperature measurements are especially important given the recent interest in global change. Typically, Rayleigh-scatter lidars are operated during the nighttime hours producing a nighttime temperature average. Daytime observations are possible but the separation of the solar background is a complex endeavor.

The absolute temperature measurements derived from Rayleigh-scatter lidar observation are independent of any system calibrations. This makes long-term observations spanning decades possible without routine system calibrations. The Atmospheric Lidar Observatory has completed an 11-year temperature climatology comprised of observations spanning from 1993 through 2004. The nighttime temperature profiles during this period have been combined into a single composite year. These climatological values are unique in that while extensive, long-term observations are straightforward very few groups have endeavored to make them.

The 11-year temperature climatology developed in this work provides a gold standard or reference for comparison. For instance, the dynamics of the atmosphere are such that the nighttime temperature structure on a particular night can be significantly different than the long-term average. An example, described in this work, is a large amplitude temperature wave observed in the upper mesosphere. Without the

climatological value for comparison the true amplitude of this oscillation would be an unknown quantity. In addition comparisons can be carried out with other climatologies to look for geographical or temporal differences, with atmospheric models to test their validity, and with first-principles models to explore the combination of physical, chemical, and radiative processes they are based on.

1. Statement of Problem

The structure of the Earth's atmosphere is typically described in terms of its temperature structure. In order of increasing altitude the layers of the atmosphere are the troposphere, stratosphere, mesosphere, and the thermosphere. The lowest region, the troposphere, is characterized by a decrease in temperature with altitude of 6.5 K/km and extends from the ground to an altitude of ~12 km. The majority of the Earth's atmosphere is located in this region along with the majority of it weather. The stratosphere is characterized by an increase in temperature with altitude. Between the troposphere and the stratosphere is the boundary region, the tropopause, which represents a balance between the cooling in the upper troposphere and heating in the lower stratosphere. The heating in the stratosphere is in part due to the absorption of solar radiation by ozone. The highest temperatures are reached at its upper boundary, the stratopause where the heating from ozone is balanced by the radiative cooling from CO_2. The mesosphere is characterized by a decreasing temperature with altitude due mainly to the cooling from CO_2 and the decreasing heating from ozone. The boundary between the mesosphere and the thermosphere is the mesopause. The mesopause is the coldest region in the atmosphere where the temperature at polar latitude is routinely as low as 130 K

during the summer. In the upper mesosphere, lower thermosphere region, atmospheric dynamics plays a major role causing the timing of the temperature minimum and maximum to be opposite what one would expect from radiative balance. The altitude of the mesopause is dependent upon season, but the boundary is typically between 85 and 100 km at mid-latitudes. Above the mesopause is the thermosphere where the temperature again increases, this time because of the absorption of solar energy by O_2 and because of its dependence upon solar and geomagnetic activity. It can reach an asymptotic temperature above 300 km between 500 K and 2000 K.

The term "lower atmosphere" typically refers to the troposphere and the lower half of the stratosphere. Routine measurements of this portion of the atmosphere are carried out twice daily via weather balloons that typically reach altitudes of 20 to 30 km well into the stratosphere.

The middle atmosphere is composed of the stratosphere, stratopause, mesosphere, and mesopause. Because the temperature structure of this region of the atmosphere is dependent upon the relative abundance of two greenhouse gases, CO_2 and O_3, the middle atmosphere has become an important area of study.

Measuring the middle atmosphere has proven to be a difficult proposition. The rarefied atmosphere of the middle atmosphere prevents the use of weather balloons or high altitude aircraft to probe much more than the lower boundary of this region. However, the atmospheric density is sufficiently great to prevent satellites orbiting in this region, which is illustrated by the fact that most small meteorites or shooting stars burn-up in the atmosphere between 80 and 110 km, giving rise to metal layers in this altitude range. The earliest measurements of the middle atmosphere were carried out by rockets

that could carry instruments into the mesosphere on a ballistic trajectory. This method is still in use today on a limited basis due to the cost of rocket campaigns. Routine measurements of the middle atmosphere are therefore carried out via remote sensing. These measurements can be made from either ground-based or satellite-based instruments.

Satellite-based instruments can provide a global picture, but make sacrifices in resolution to do so. Typically instruments for atmospheric measurements are either downward looking (nadir) or limb scanning. Each style of instrument has its own set of limitations. Nadir looking instruments can provide good horizontal resolution assuming that short integration times are used [e.g., *Christensen et al.*, 2003]. Several spectral bands are measured for each location. These measurements are combined with a knowledge of the absorption features in the atmosphere to produce a vertical profile. The vertical resolution is poor, ~10 km, due to the vertical width of the absorption features, Figure 1.

Limb scanning instruments are larger and mechanically more complex than nadir instruments, but provide for simpler data analysis. Data is collected on a tangent line through the atmosphere, Figure 2(a). Through careful weighting of the contributions from each altitude, Figure 2(b), vertical profiles of the atmosphere can be generated with an altitude resolution of 1 to 2 km. However, the horizontal resolution is poor especially in the direction of the tangent point where it is typically 200 km [e.g., *Remsberg et al.*, 2003; *Shepherd et al.*, 2004a; *Huang et al.*, 2006].

The vast majority of satellite measurements of the atmosphere use passive optical instruments. They rely on intensity measurements of various emission and absorption

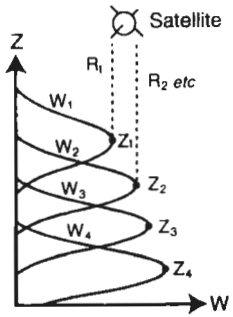


Figure 1. Idealized weighting function for a radiance measurement from above [*Taylor*, 2005].

spectra from various sources. These spectra are attenuated to varying degrees by the atmosphere. It is this attenuation that produces the vertical information in a nadir instrument, for example. Several of these emission spectra can also be observed by ground-based instruments.

Ground-based instruments do not have global coverage but produce high time-resolution measurements over a single point on the globe. Depending on the instrument, high resolution temporal and spatial measurements are possible. The higher resolution of ground-based instruments has proven useful in investigating the oscillations that occur in the atmosphere such as gravity waves, tides, and planetary waves. Ground-based instruments can be classified as either passive or active. Passive instruments include various optical devices such as photometers, imagers, spectrometers and interferometers to determine parameters from airglow in the middle and upper atmosphere. For example,

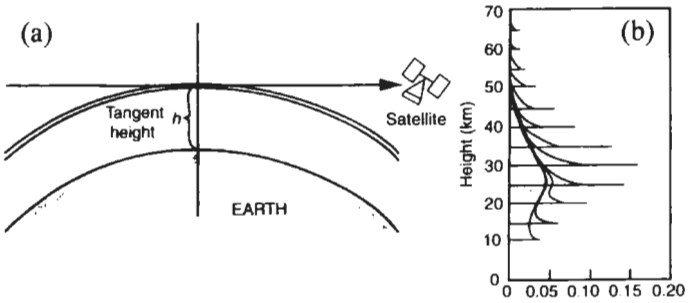


Figure 2. (a) Diagram of Limb scanning measurement at some arbitrary tangent height. (b) An example of the weighting function used for limb measurements [*Taylor*, 2005].

all-sky cameras produce height integrated images of the OH layer. The field of view of the camera at ~86 km is approximately 400 km [e.g., *Taori et al.*, 2005].

Active ground-based instruments rely on transmitting electromagnetic radiation either in the radio or optical spectrum. For measurements of the middle atmosphere the active instruments are limited to various lidar and radar techniques. There are several types of radars that are used for remote sensing of the middle atmosphere. The Stratosphere-Troposphere or ST radar provides coverage from 1 to 30 km and MF radar provides coverage from 60 to 100 km for daytime observations and 80 to 110 km for nighttime [e.g., *Tepley et al.*, 1981; *Lathuillere et al.*, 1983; *Kofman et al.*, 1984]. As a result, there is a coverage gap across the middle of the mesosphere, Figure 3. Furthermore, these radars do not measure temperature. Lidar, or as it has more traditionally been called "optical radar," is an acronym like radar that stands for LIght Detection And Ranging. Lidars are usually classified by their scattering mechanism: Mie scatter, Rayleigh scatter, Raman scatter, and resonance scattering.

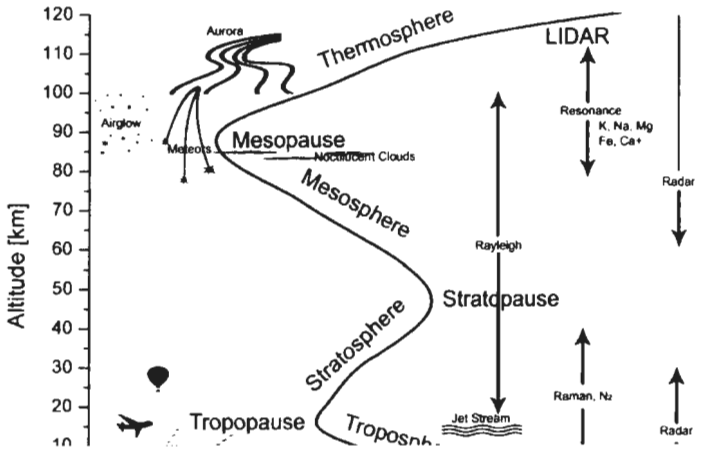


Figure 3. The temperature profiles of the neutral atmosphere. Several of the observational techniques and atmospheric phenomena are illustrated. Note the range of the Rayleigh lidar technique and the radar gap in the middle atmosphere.

Rayleigh-scatter lidar is capable of making measurements of relative density and absolute temperature from 30 to 110 km. The electromagnetic wave of an incident photon induces an oscillating dipole in the scattering molecule, elastically scattering the photon. The number of backscattered photons is linearly proportional to the atmospheric density. These relative density measurements can then be used to determine an absolute temperature profile, which is not dependent upon an absolute instrument calibration and provides a good standard for comparisons. In the case of molecules, rotational and vibrational Raman lines appear offset from the laser wavelength. The Raman lines can be used to measure the relative densities of molecular species because the energy offset, hence wavelength offset, is species dependent.

Several metal layers form because of the constant influx of micrometeorites. These micrometeorites burn up in the atmosphere between 80 and 110 km giving rise to the layers. In principle, lasers can be tuned to a resonance transitions in metals. Typically this is done with alkali metals, but has also been done with iron. The atmospheric density of these metals is fairly low, but the scattering cross section is quite large creating a strong lidar return. These layers can be used to determine temperatures and wind speeds between 80 and 110 km. In astronomy these lasers have been used as artificial guidestars for adaptive optical systems on large-aperture telescopes. For smaller systems Rayleigh scatter from 25 to 30 km can be used as a guide star.

Mie-scatter uses the same scattering mechanism as Rayleigh-scatter, but the scattering is due to particles that are much larger than the wavelength of the transmitted light. The aerosol particles are typically limited to the first 20 to 30 km of the atmosphere depending on volcanic activity.

The upper mesosphere and the lower thermosphere or the MLT region of the atmosphere hosts a variety of optical phenomena that can be measured from ground-based instruments. Of particular interest to lidars are noctilucent clouds (NLC), which occur typically near 83 km in the polar regions. They are ice clouds formed in the cold region near the summer mesopause. The term noctilucent is Latin for "night shining." Given the high altitudes of the clouds, they are illuminated by sunlight well after the sun has set. Shortly after civil twilight (6° solar depression angle) the background sky is sufficiently dark that the scattered light from the NLC can be seen by the naked eye. The first recorded sightings of NLC were during the summer of 1884 shortly after the eruption of Krakatoa in 1883. It is believed that the large amount of dust ejected into the

lower atmosphere was eventually transported into the mesosphere, where it served as nucleating agents for the ice crystals [*Thomas et al.*, 1994].

NLCs are observed during the summer in both the northern and southern hemispheres. Historically NLC observations are carried out by amateurs who have observed and noted the location, time, and angular spread of the NLCs. With the growing concern over global climate change, interest in NLCs has increased as two greenhouse gasses play an important role in their formation. Increases in methane increase the water vapor concentration, typically 2-4 ppm, in the mesosphere thereby increasing the temperature at which the deposition and subsequent growth of the ice crystals occurs. The second greenhouse gas is carbon dioxide which contributes to the temperature structure of the atmosphere. Carbon dioxide is typically attributed to warming the Earth's surface and lower atmosphere by absorbing and reemitting part of the infrared surface emissions that would otherwise normally pass into space, thereby cooling the Earth and atmosphere. While effectively insulating the lower atmosphere, CO_2 is an efficient emitter of IR, cooling the middle atmosphere. Increases in CO_2 and CH_4 are favorable for the formation of NLCs at lower latitudes. Their more frequent appearance or occurrence at lower latitudes might be a very sensitive indicator of climate change. As a result it has been debated whether NLCs have become the "Miner's Canary" for climate change [*Thomas and Olivero*, 1989; *Thomas et al.*, 1989; *Thomas*, 1996a, b; *von Zahn*, 2003].

The ice crystals that form the NLCs have large scattering cross sections and produce a strong Mie-scatter signal. The short pulse lengths of the laser enable high vertical resolution observations of NLCs. Unlike satellites or rockets, lidar observations

measuring the same volume, over a particular location, for an extended period, in short intervals, give a time progression for NLC development. The earliest observation of an NLC by lidar was in 1989 [*Hansen et al.*, 1989]. Lidar measurements of NLCs are typically given as the backscatter ratio, which is the ratio of the Mie signal to the standard Rayleigh signal. If the relative density measurements for the lidar are normalized to an absolute density measurement then the NLC's volume backscatter coefficient can be calculated.

The results in this research are from a Rayleigh-scatter lidar systems designed to detect the Rayleigh backscatter from molecules in the middle atmosphere. Vertical soundings of relative density are available above 41 km. In addition to the temperature determinations, NLC backscatter ratios are also available. As most Rayleigh-scatter lidar facilities are at permanent locations, they provide high-time resolution but provide limited geographical coverage. Temperatures from the lidar are typically provided as hourly or nightly profiles. The high temporal and vertical resolution of the lidar system are important for the study of the middle atmosphere as they enable the study of a wide range of important atmospheric phenomena, including gravity waves, tidal variation, stratospheric warmings, planetary waves, noctilucent clouds, mesospheric inversion layers, solar rotation 28-day variation, seasonal variations, sunspot cycle effects, and long-term trends, all of which contribute to the general climatology and dynamics of the middle atmosphere.

2. Overview

The objectives of this dissertation are to

1) Provide a temperature climatology from the measurements made with the ALO Rayleigh-scatter lidar between 1993 and 2004. This climatology is made from the second longest dataset of mid-latitude Rayleigh-scatter measurements to date. The longer one is from a very different longitudinal region. A comparison between these two climatologies explores possible longitudinal and temporal differences.
2) The recently updated NRL MSIS global climate change is a widely used empirical model composed of historical observations from a variety of sources. How well does this model compare to mid-latitude, mesospheric observations? A comparison between the ALO climatology and the MSIS model is presented and explores this question.
3) Previous NLC observations occurred poleward of 50° latitude. Climate change predicted their appearance equatorward of this region later this century as CO_2 concentrations increase [*Thomas*, 1996a]. Their appearance 8° more equatorward was unexpected and raises a number of questions. Presented here are the observations and characteristics of the two lidar observations of NLCs at 42° N from the ALO Rayleigh-scatter lidar:
    a. NLC observation from 1995, and
    b. NLC observation from 1999, re-analyzed to compare with the 1995 results.

They lead to a likely explanation for the NLC occurrence.

This dissertation is organized with a background into the Rayleigh-scatter temperature lidar theory and error analysis in Chapter 2 along with the error analysis and theory for NLC measurements via Rayleigh lidar. Chapter 3 details the results from the ALO temperature climatology and compares them to a second Rayleigh-scatter climatology from France [*Hauchecorne et al.*, 1991]. Chapter 4 details the results from the comparison of the MSIS model to the ALO climatology. Chapter 5 details the NLC observations made by the ALO Rayleigh-scatter lidar and includes a discussion of the large amplitude waves observed during this period that were essential for the production of the mid-latitude NLCs. The summary and future works are detailed in Chapter 6.

CHAPTER 2

RAYLEIGH-SCATTER LIDAR SYSTEM

The Atmospheric Lidar Observatory (ALO) is located on the Utah State University (USU) campus and has operated a Rayleigh-scatter lidar since 1993. This Rayleigh-scatter lidar system can produce relative density measurements that extend from the stratopause to the mesopause (45 to 95 km). These relative measurements of density can be used to derive absolute temperatures without the necessity of instrument calibration. This and its unique coverage of the mesosphere are the main strengths of the Rayleigh-scatter technique. The block diagram for a lidar system is comparable to that of a radar system. In the case of a lidar, the transmitted electromagnetic radiation is typically in or near the visible spectrum of light. The radio transmitter and receiver antenna of a radar system are replaced by a laser and an optical telescope. Lidar systems are characterized by their scattering method and their power-aperture product. The power-aperture product is a measure of the transmitted power and the collecting area of the system's receiver. A more complete measurement of the sensitivity of a lidar system would include the backscatter cross-section as another factor times the power-aperture product. A more detailed description of the transmitter and receiver of the USU Rayleigh-scatter lidar system follows.

1. Lidar Transmitter

The transmitter for a Rayleigh lidar is typically a pulsed laser with high pulse energy. The acronym laser stands for Light Amplification by the Stimulated Emission of Radiation. Two different lasers have been used in the ALO Rayleigh-scatter lidar over

the course of its operation. Both lasers were solid state Nd:YAG (neodymium:yttrium aluminum garnet) lasers. In the case of lasers, solid state refers to the lasing medium. A Nd:YAG laser suspends the lasing medium, in this case neodymium, inside of an artificially grown crystal. Other lasers are available where the lasing medium is suspended in a gas or liquid. Typically the fundamental wavelength of the Nd:YAG lasers is 1064 nm, but can be modified to generate other fundamental wavelengths. The two lasers used in the ALO systems were a GCR-5 and a GCR-6 from Spectra Physics. They shared the same oscillator-cavity design and components with the main difference being that the GCR-6 has two amplifiers each with a single flash lamp. The GCR-5 has a single amplifier with two flash lamps. The additional gain medium in the GCR-6 produces nearly 48 watts at 1064 nm compared to 36 watts for the GCR-5. The GCR-5 was a replacement for the larger GCR-6 laser. Both lasers have a pulse length of 7-8 ns, which is produced by use of a Q-switch in the oscillator cavity. A Q-switch is an opto-electrical component that relies on a crystal that lacks inversion symmetry. It introduces loss into the optical cavity through cross polarization. This is accomplished by rotating the polarization so that it is cross polarized relative to a linear polarizer. This introduces a high loss into the cavity that prevents lasing. This allows for a large population inversion to build up inside the lasing medium, after which time a high-voltage pulse is applied to the Q-switch changing the polarization by 90° to allow the cavity to lase. The resulting laser pulse is significantly shorter and more intense than what is produced when the Q-switch is not employed. A second result of the Q-switch is to linearly polarize the output. The use of lasers with a short pulse and high energy density is vital in the middle atmosphere lidar applications. The short-pulse length allows for high resolution range

information to be collected and the high pulse energy produces a high ratio of signal to noise. The pulse used to trigger the Q-switch is also used as the start trigger for the data-acquisition system. It provides an accurate measurement for the zero range, ignoring the insignificant delay introduced by the cables carrying the trigger and data signals. Typically, when the laser is operated with an open Q-switch, the laser is said to be long-pulsing. Under this condition, the laser output is only a few watts and the pulse length increases dramatically to ~200 milliseconds. Long pulsing the laser allows for the optical setup and alignment to be done at moderately safe energy levels.

The pulse energy and repetition rates of the laser are not the only selection criteria in choosing the laser for a Rayleigh lidar. The first consideration is its reliability and ease of use. The Nd:YAG laser is a solid-state laser that needs very little maintenance. The routine maintenance involves replacement of the flash lamps used for the excitation source. That takes approximately 1 hour and does not affect the alignment of the system and it is done only after ~40,000,000 pulses or 370 hours of operation. The ease of maintenance is important as routine and consistent measurements are necessary to produce long-term temperature observations for the climatology.

The backscatter cross section for Rayleigh scattering varies as λ^{-4}, Eq. 2.1.1, the scattering favoring shorter wavelengths [*Measures*, 1992]

$$\sigma_{\pi}^{Ray} = 5.45\left\{\frac{550nm}{\lambda(nm)}\right\}^{4} \times 10^{-28}\ cm^{2}\ sr^{-1}. \qquad 2.1.1$$

The fundamental wavelength of Nd:YAG lasers is typically 1064 nm, well beyond the visible light range. Frequency doubling and tripling enables the generation 532-nm and 355-nm light in addition to the 1064-nm fundamental. The maximum efficiency of the

frequency doubling from 1064 nm to 532 nm is typically near 50%. The power of the lasers therefore drops to 18 watts or 24 watts depending on the laser. This loss in the transmitted power is more than made up for by a factor of sixteen increase in the backscatter cross section at 532 nm for an overall increase in the return signal by a factor of 8. To triple the fundamental frequency requires that it first be doubled, then mixed with the fundamental, making the overall tripling efficiency much lower than that for doubling. At 355 nm, the tripling moves the wavelength outside of the visible spectrum making the system difficult to work with. In addition to the lower pulse energy for doubling and tripling, the laser reduces the number of photons per watt because each photon now has more energy. These factors along with the atmospheric transmittance make the gain in return signal marginal for tripling the wavelength. As a result, 532 nm is the dominant wavelength used in Rayleigh lidar. As laser technology develops, making available additional wavelengths, the driving force in laser selection may be the detector quantum efficiency.

The frequency doubled output pulse from the Nd:YAG laser is a combination of two beams, one at 532 nm and the other at 1064 nm. As the receiver is blind to the 1064-nm light there is no advantage to transmitting this wavelength into the night sky. A dielectric beam splitter, a dichroic, is used to separate the two wavelengths. It possesses a high reflectance at 532 nm, $R > 99.5\%$, and a high transmittance at 1064 nm, $T > 90\ \%$. A second dichroic is used to further reduce the 1064-nm radiation and to direct the beam vertical to align it with the field of view of the receiving telescope. The two 1064-nm beams that are separated from the transmitted beam are absorbed by beam stops and, on occasion, a power meter to monitor the laser performance.

2. Lidar Receiver

The receiver system is composed of the telescope, optics, mechanical chopper, interference filter, and the detector and its cooled housing. A simplified diagram of the ALO Rayleigh-scatter lidar is given in Figure 4. The telescope and associated optics are used to increase the collecting area of the detector system and to limit the field of view. The optical layout for the lidar is co-axial, using the same optical axis for the transmitter and receiver. Various optical elements are used to direct the output of the telescope into the photon detection system and co-align the optical axis of the telescope and the laser.

A Newtonian telescope with a 44-cm diameter and a 201-cm focal length is used to collect the backscattered light. The telescope is mounted horizontally on the same optical table as the transmitter, minimizing the relative motions between the transmitter and receiver. A large turning mirror is placed at a 45° angle to direct the return signal into the telescope, as illustrated in Figure 4. The transmitted signal, to be co-axial with the receiver, passes through a small circular aperture in the center of the turning mirror. The loss of the center of the turning mirror has little effect on the system sensitivity as this region is already obscured by the secondary mirror in the Newtonian telescope. The output of the Newtonian telescope comes to a focus slightly beyond the telescope's tube. Here the light collected by the telescope passes through a field stop, which limits the field of view to triple that illuminated by the laser. This allows for small fluctuations in the pointing of the laser system due to thermal effects within the laser and small misalignments between the two optical axes. A wider field of view would only increase the background noise without increasing the number of backscattered photons collected, decreasing the signal-to-noise ratio. After the field stop, a small lens is used to collimate

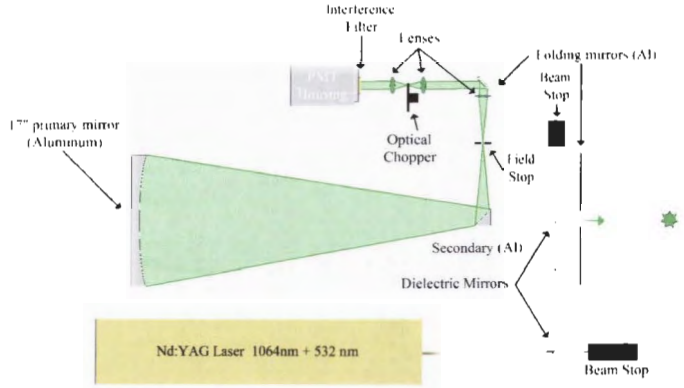


Figure 4. Simplified diagram of the USU Rayleigh-scatter lidar diagram. The 532nm light is illustrated in green with the 1064 in red. The dotted red line is the residual 1064 nm light that is virtually eliminated from being transmitted by the second dielectric mirror. The laser output is directed vertically along with the field of view of the telescope but has been depicted horizontally for simplicity.

the return signal and a folding mirror directs the collimated light into the rest of the detector system. The collimated beam is focused onto the plane of a mechanical chopper by a second lens. The chopper operates at a multiple of the 30-Hz repetition rate of the laser and blocks the strong low-altitude signals from the atmosphere, which could damage the detector. After the chopper, the light is re-collimated by a third lens and sent into the detector housing.

Before the light enters the detector, it passes through a narrow band-pass interference filter. For Rayleigh-scatter, the incident and scattered photons are of the same wavelength and the transmitted pulse from the laser is spectrally very narrow. An interference filter reduces the amount of "white" light that enters the receiver system from the background sky. The transmission profile of one of the interference filters is

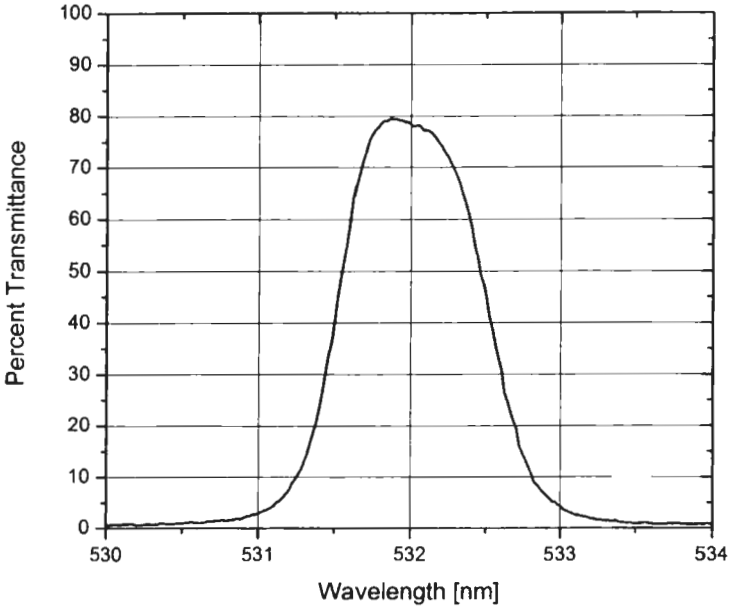


Figure 5. Transmission profile of the 532nm interference filter. The FWHM of the filter is approximately 1 nm for normal incidence.

given in Figure 5, showing a peak transmittance of 80% and a width of 1 nm (FWHM). This is a compromise between the width of the band pass and its transmittance and cost.

The photon detector for this system is a green sensitive bi-alkali photomultiplier tube (Electron Tubes 9954 B), which converts the incoming photons into pulses of electrons. The conversion of the photons to electrons is done by the photocathode through the photoelectric effect. These photoelectrons are then amplified through a dynode string with a typical gain of 10^6, Figure 6. Each successive dynode in the string is maintained at a higher potential than the previous one. The potential difference

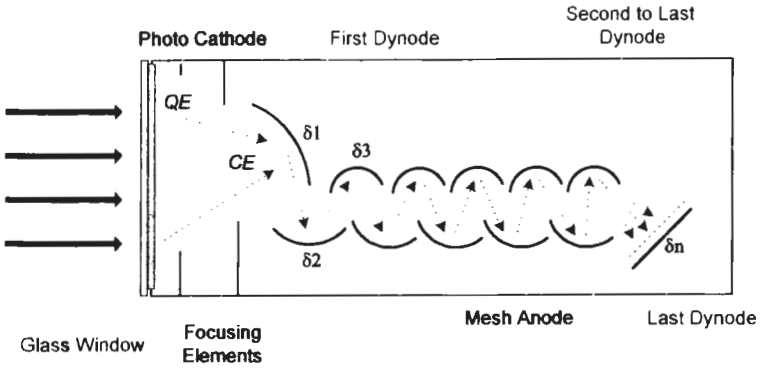


Figure 6. Diagram of a 12 stage linear focus photomultiplier tube. Here the roles of quantum efficiency, QE, and collection efficiency, CE, are illustrated along with the individual dynodes.

between the photocathode and the first dynode is typically 300 volts. Focusing elements, at the cathode voltage, increase the collection efficiency by directing the photoelectrons towards the first dynode. The amplification of the photoelectrons in the pulse is done through the generation of secondary electrons at each dynode with the total gain being a product of the gain at each stage. A PMT with a linear dynode string was chosen because it provides a linear response over a large dynamic range. The effective quantum efficiency of the photomultiplier tube is ~13 percent at 532 nm. While other detectors have higher quantum efficiency, they are not well suited for photon counting in a lidar system. A CCD for example would have to be read at a rate of 4 MHz to provide adequate range resolution. However, the maximum read-out rate is at least two orders of magnitude slower. In addition, the readout noise generated would overwhelm the returns which are from single-photon events.

The signals generated from the PMT include a certain amount of spurious noise that is referred to as the dark count of the tube. This spurious noise is a product of a few thermal electrons from the photocathode and each of the dynodes in the amplifier chain. These thermal electrons are then amplified by the subsequent dynodes in the dynode chain and can be mistaken as photon events. Several steps are taken to reduce the number of thermal electrons that are measured by the system. The first is to minimize the generation of the thermal electrons by cooling the PMT. The PMT is placed inside a housing that provides the necessary cooling and electro-magnetic shielding. Two different PMT housings were used during the period of the lidar observation in this work. Both housings are from Products for Research and use thermoelectric (Peltier) coolers. The first housing relied on an air heat exchanger and cooled the PMT to −10 C. The second housing used a liquid heat exchanger using liquid at 5 C and was able to cool the PMT to -25 C. The second step is to discriminate between photons generated at the photocathode and those generated by the dynodes. A thermal electron produced by the cathode is indistinguishable from a photoelectron, but those produced within the dynode chain are not as strongly amplified. The peak voltage from a pulse of electrons measured at the anode can therefore be used to discriminate the pulses from the photocathode and those generated in the dynode chain.

The PMT must provide a linear response to the large dynamic range of the lidar returns. In addition to the style of PMT used, the high-voltage power supplied to the dynode chain is another critical component. A high-voltage power supply provides a cathode voltage of −1850 and a resistive voltage divider is used to create the potential differences between each stage of the chain. For high linearity, the current flow down the

dynode chain, from the secondary electrons, must be a small fraction, <1%, of the current flow in the resistor chain. This ensures that the potential difference across each dynode remains constant giving a constant gain. However, in the last few stages of the dynode, the current increases dramatically and it is necessary to add several capacitors into the voltage divider to maintain the dynode voltage.

The gain of the PMT can be altered, or gated, by changing the voltage on one or several dynodes to equal that of the previous stage, thereby preventing the propagation of the photoelectrons down the dynode chain. The PMT is gated off in the USU system below an altitude of 38 km, below which, the intensity of the returns is sufficient to cause resistive heating of the mesh anode, leading to eventual failure. (Actually the gain is not turned off, but reduced by a factor between 500 and 1000.) After the PMT is gated back on, a short period is required for the dynode voltages to return to normal values and the cloud of photoelectrons to dissipate. Typically good results are measured above 41 km.

3. Data Acquisition System

The output of the PMT is a short negative pulse with a rise time of 2 ns and a pulse width (FWHM) of 3 ns. Once the signal leaves the PMT, it passes through a fast pre-amplifier that is located just outside the PMT housing. This is a non-inverting pre-amp with a gain of 200 and a 1-ns rise time. The distance between the PMT and the pre-amp is kept to a minimum to reduce possible electromagnetic interference with the small voltages produced by the PMT.

The lidar records the number of photon-induced pulses in each time bin digitally. This is done with a Multi-Channel Scalar or MCS. An MCS unit is basically a time

correlated photon counter, which is used widely in time-of-flight measurements. The previously mentioned voltage discriminator, is part of the MCS unit and once the voltage drops below this threshold level (the voltage output of the PMT is negative) a single photon count is registered. The maximum count rate for the MCS is 150 MHz or ~7 ns between photons. The system will undercount the returns if the time separation between arriving photons is less than 7ns, effectively defining the dead time for the system, all other elements being faster. The largest count rate is at 45 km with an average rate not exceeding 1 MHz. To account for the system dead time, the correction between the actual count rate and the measured count rate would be

$$R' = \left(\frac{R}{1 - RT_d} \right), \qquad 2.3.1$$

where R is the measured count rate, T_d is the dead time and R' is the actual count rate. Given the dead time of the MCS unit and the expected count rate, this correction is less than 1% and is not applied. If the minimum altitude were lowered to 30 km, the undercounting would have a measurable effect on the temperature results requiring the correction Eq. 2.3.1 be applied.

The MCS unit is able to measure the count rate as a function of time. The arriving photons are not recorded with a time stamp, but are binned together by small time increments. The minimum time bin is 5 ns or a range bin of 0.75 m; the upper limit is 18 hours. The MCS has sufficient memory for 16,000 bins and a maximum value of 1.6×10^7 counts/bin. For the ALO lidar, the bin width is 250 ns or a range of 37.5 meters. The returns are measured out to a distance of 540 km using 14,400 range bins. An atmospheric profile is obtained 30 times a second and would produce about 1.7

Megabytes/sec if each profile were recorded individually. In this manner, a single hour of data would occupy 6 gigabytes of hard drive space. To reduce the file sizes, each of the 14400 range bins is summed with the corresponding bin from the previous pulse over 3600 laser pulses (2 minutes). This produces a single 56 KB file generated every 2 minutes. As the Brunt-Väisälä frequency in the middle atmosphere is approximately four minutes, averaging the returns over two minutes will not produce aliasing in the returns. A similar argument could be made for less vertical resolution because the scale height in the middle atmosphere is on average about 7 km. 37.5-m is overkill for the neutral atmosphere, but the results can be averaged in altitude afterwards and this high resolution is valuable for measurements of cirrus clouds, noctilucent clouds and other layers.

4. Relative Density Measurements

According to the lidar equation the number of backscattered photons $N(h)$ scattered from a laser pulse of N_0 photons will be proportional to the product of the square of the atmospheric transmission, $T(h)$, at the laser wavelength between the lidar and the scattering altitude, the molecule cross section for Rayleigh backscatter, σ_π^R, the efficiencies of the receiver system, Q, and the range squared correction as follows

$$N(h) = \frac{N_o A Q T^2(h)}{h^2}\left(n(h)\sigma_\pi^R\right). \qquad 2.4.1$$

The lidar equation may be inverted to give the relative molecular density as a function of altitude in terms of the measured quantities above a reference altitude h_o.

The relative density can be found by taking the ratio of the atmospheric number density at two altitudes

$$n(h) = n(h_o)\frac{N(h)h^2T^2(h_o)}{N(h_o)h_o^2T^2(h)} \qquad 2.4.2$$

Unlike the basic lidar equation, the measurements of the relative density have no dependence upon the optical efficiency of the lidar system, or the backscatter cross section. These parameters can be assumed constant over the short period when the observations are made. The lower altitude for the ALO lidar is 45 km which is above the majority of the atmosphere and is above the ozone absorption from the Chappius bands. The amount of energy scattered out of the laser beam between 45 and 95 km is much less than 1 percent such that $T(h_o) \approx T(h)$ and N_0, the transmitted photons, are constant over the observational range as the atmosphere has become optically thin.

5. Absolute Temperatures

Under the assumption that the atmosphere is composed of an ideal gas in hydrostatic equilibrium, it is possible to derive temperature from relative density [*Hauchecorne and Chanin*, 1980; *Chanin*, 1984; *Chanin and Hauchecorne*, 1984; *Gardner et al.*, 1989]. Hourly averages or night averages of the relative densities are used in calculating the temperature profiles. Given the long integration times, the assumption that the atmosphere is in hydrostatic equilibrium is valid.

The steady-state diffusion equation or hydrostatic equilibrium equation is the balance between the gravitational force and the pressure gradient

$$\frac{dP(h)}{dh} + n(h)m(h)g(h) = 0. \qquad 2.5.1$$

Here $m(h)$ is the mean molecular mass of the atmosphere, $n(h)$ is the number density, $P(h)$ is pressure, and $g(h)$ is gravitational acceleration which varies with height. The equation for hydrostatic equilibrium may be combined with the ideal gas law,

$$P(h) = n(h)k\,T(h), \tag{2.5.2}$$

to give the relationship

$$k\frac{d(n(h)T(h))}{dh} = -n(h)m(h)g(h). \tag{2.5.3}$$

Here $T(h)$ is the temperature, and k is Boltzman's constant. This equation is easily integrated over the altitude region from h, the altitude of interest, to some particular reference altitude h_0,

$$k\left[n(h_0)T(h_0) - n(h)T(h)\right] = -\int_h^{h_0} n(h')m(h')g(h')\,dh'. \tag{2.5.4}$$

It is now possible to solve for the temperature $T(h)$ at our altitude of interest.

$$T(h) = T(h_0)\frac{n(h_0)}{n(h)} + \frac{1}{k\,n(h)}\int_h^{h_0} n(h')m(h')g(h')dh'. \tag{2.5.5}$$

In this form any error in the measurement of relative density will enter into the equation. The error in the measurement may even cause the temperatures to diverge through the $\frac{n(h_0)}{n(h)}$ ratio. If however, we choose h_0 to be some initial maximum starting altitude h_{max} and the integration is done to some lower altitude

$$T(h) = T(h_{max})\frac{n(h_{max})}{n(h)} + \frac{1}{k}\frac{n(h_{max})}{n(h)}\int_h^{h_{max}} \frac{n(h')}{n(h_{max})}m(h')g(h')dh'. \tag{2.5.6}$$

In this form, any of the system-dependent parameters divide out of the temperature calculations. The measurements of density are relative. However, as the temperature is

derived from the ratio of two relative measurements, the temperature becomes an absolute measurement (except for the 1st term, which decreases rapidly with decreasing altitude).

The temperature algorithm is based upon an initial temperature at the chosen h_{max}. Typically we choose h_{max} to be the altitude at which the signal is 16 times its own standard deviation. The initial temperature for this altitude must be provided from some source outside of the Rayleigh lidar. Ideally, this measurement can be taken from a co-located instrument that can provide simultaneous measurements such as a resonance lidar or a hydroxyl temperature detector at 87 km. This initialization temperature can also be taken from a model or in the case of the ALO lidar from another mid-latitude temperature climatology. Currently if the altitude is above 83 km, the starting temperatures are taken from the sodium lidar climatology from Colorado State University (CSU) and interpolated for the correct date and altitude. However, if the starting altitude is below 83 km, the starting temperature is based on a combination of both the MSISe00 model and the sodium climatology. The offset between the climatology and the model at 83 km at midnight is used to offset the model temperature at lower altitudes.

6. Measurement Uncertainty

The return profiles, as previously mentioned, are a sum of 3600 separate soundings of the atmosphere made by the lidar system. These profiles can be considered to consist of two different signals, the Rayleigh-scatter signal S and the background noise signal N. It is then possible to separate the Rayleigh-scatter signal averaged over a small altitude region from the total if the background is known and constant with altitude

$$S_j = \frac{1}{I}\sum_{i=i_0}^{i_0+(I-1)}(S+N)_{ij} - \frac{1}{K}\sum_{k=k_0}^{k_0+(K-1)} N_{kj} = \overline{(S+N)_{ij}} - \overline{N_{ij}} \qquad 2.6.1$$

Here I and K correspond to space (the number of height intervals for signal and background, respectively) and J corresponds to time (the number of 30-second time intervals). The background at each altitude is unknown and is approximated by the total signal at high altitude where there is no Rayleigh-scatter signal and, again, is assumed to be constant in altitude. This assumption places certain requirements on the data selection described in Chapter 3.

Variations in the return signal and the background can also be calculated. First is the background variance

$$d\overline{N_j} = \sum_{k=k_0}^{k_0+(K-1)} \frac{\partial \overline{N_j}}{\partial N_{kj}} dN_{kj} = \frac{1}{K}\sum_{k=k_0}^{k_0+(K-1)} dN_{kj}. \qquad 2.6.2$$

Square and add, assuming each measured N_{kj} is independent. Then, letting

$$\sigma_x^2 = (dx)^2, \qquad 2.6.3$$

the average background variance is

$$\sigma_{N_j}^2 = \frac{1}{K^2}\sum_{k=k_0}^{k_0+(K-1)} \sigma_{N_{kj}}^2, \qquad 2.6.4$$

which reduces to,

$$\sigma_{N_j}^2 = \frac{\sigma_{N_{kj}}^2}{K} \qquad 2.6.5$$

when the background variance, i.e., $\sigma_{N_{kj}}^2$, is constant over K altitudes. The variance of the combined signal and noise can be calculated in the same way

$$d\overline{(S+N)_j} = \sum_{i=i_0}^{i_0+(I-1)} \frac{\partial \overline{(S+N)_j}}{\partial (S+N)_{ij}} d(S+N)_{ij} = \frac{1}{I}\sum_{i=i_0}^{i_0+(I-1)} d(S+N)_{ij}. \qquad 2.6.6$$

Square and add, assuming each measured $(S+N)_{I,J}$ is independent,

$$\sigma^2_{(S+N)_J} = \frac{1}{I^2}\sum_{i_0}^{i_0+(I-1)} \sigma^2_{(S+N)_{I,J}} \qquad 2.6.7$$

We now have calculations for the variance of the noise and the combined signal and noise. The variance for the signal alone averaged over I range bins (Eq 2.6.1) is given by

$$\sigma^2_{S_J} = \sigma^2_{(S+N)_J} + \sigma^2_{N_J} = \frac{1}{I^2}\sum_{i_0}^{i_0+(I-1)} \sigma^2_{(S+N)_{I,J}} + \frac{\sigma^2_{N_{K,J}}}{K} \qquad 2.6.8$$

Due to the fact the return signal follows Poisson statistics $\sigma_x^2 = x$, we can substitute the return signal in place of the variance,

$$\sigma^2_{S_J} = \frac{1}{I^2}\sum_{i_0}^{i_0+(I-1)}(S+N)_{I,J} + \frac{1}{K^2}\sum_{k=k_0}^{k_0+(K+1)} N_{k,J} \qquad 2.6.9$$

Or, noting that the terms on the right include the average of $(S+N)_{I,J}$ over I altitudes and $N_{k,J}$ over K altitudes, this can be rewritten as

$$\sigma^2_{S_J} = \frac{1}{I}\overline{(S+N)_{I,J}} + \frac{1}{K}\overline{N_{K,J}} \qquad 2.6.10$$

If there are other factors adding to the variability in the measurements, then our uncertainties will be underestimates. Ignoring the assumption of hydrostatic equilibrium for a moment, the temperature profile derived from a single two-minute period would not have enough precision to obtain useable temperatures at higher altitudes. A temporal average is also required to do so. This temporal averaging of the return signal enters into the averages

$$\overline{\langle (S+N)\rangle_{I,J}} = \frac{1}{J\,I}\sum_{J=J_0}^{J_0+(J-1)}\sum_{i=i_0}^{i_0+(I-1)}(S+N)_{I,J} = \frac{1}{J}\sum_{J=J_0}^{J_0+(J-1)}\overline{(S+N)_{I,J}} \qquad 2.6.11$$

$$\overline{\langle N \rangle_{KJ}} = \frac{1}{JK} \sum_{J=J_0}^{J_0+(J-1)} \sum_{k=k_0}^{k_0+(K-1)} N_{kj} = \frac{1}{J} \sum_{J=J_0}^{J_0+(J-1)} \overline{N_{KJ}} \qquad 2.6.12$$

and the variances

$$\sigma^2_{\overline{\langle (S+N) \rangle_{IJ}}} = \frac{1}{JI} \overline{\langle (S+N) \rangle_{IJ}} \qquad 2.6.13$$

and

$$\sigma^2_{\overline{\langle N \rangle_{KJ}}} = \frac{1}{JK} \overline{\langle N \rangle_{KJ}} . \qquad 2.6.14$$

Recalling the Rayleigh-scatter signal is the difference between these two averaged measurements, it is given by

$$\overline{\langle S \rangle_{IJ}} = \overline{\langle (S+N) \rangle_{IJ}} - \overline{\langle N \rangle_{KJ}} , \qquad 2.6.15$$

and its variance is given by

$$\sigma^2_{\overline{\langle S \rangle_{IJ}}} = \sigma^2_{\overline{\langle (S+N) \rangle_{IJ}}} + \sigma_{\overline{\langle (N) \rangle_{KJ}}} = \frac{1}{JI} \overline{\langle (S+N) \rangle_{IJ}} + \frac{1}{JK} \overline{\langle (N) \rangle_{KJ}} . \qquad 2.6.16$$

Thus the standard deviation of the signal is

$$\sigma_{\overline{\langle S \rangle_{IJ}}} = \sqrt{\frac{1}{JI} \overline{\langle (S+N) \rangle_{IJ}} + \frac{1}{JK} \overline{\langle N \rangle_{KJ}}} . \qquad 2.6.17$$

As stated earlier, the downward integration is started at the altitude where the signal is 16 times its standard deviation. The number of standard deviations is given by

$$\frac{\overline{\langle S \rangle_{IJ}}}{\sigma_{\overline{\langle S \rangle_{IJ}}}} = \frac{\overline{\langle (S+N) \rangle_{IJ}} - \overline{\langle N \rangle_{KJ}}}{\sqrt{\frac{1}{JI} \overline{\langle (S+N) \rangle_{IJ}} + \frac{1}{JK} \overline{\langle N \rangle_{KJ}}}} . \qquad 2.6.18$$

Having calculated the variance of the measurement, it is now possible to find the uncertainty for the temperature measurements. The temperature variance is found in

much the same way as the backscatter signal variance. Using the temperature calculation Eq 2.5.6, we can propagate the uncertainties in the return signal and derive an uncertainty for the temperature profile [*Gardner*, 1989]

$$dT = \frac{\partial T}{\partial T_{\max}} dT_{\max} + \frac{\partial T}{\partial n_{\max}} dn_{\max} + \frac{\partial T}{\partial n} dn, \qquad 2.6.19$$

$$dT = \frac{n_{\max}}{n(h)} dT_{\max} + \frac{T_{\max}}{n(h)} dn_{\max} - \left(\frac{T_{\max} n_{\max}}{n(h)} + \frac{m g(h)}{k n(h)} \int_h^{h_{\max}} n(h') dh' \right) \frac{dn}{n(h)} + \frac{m g(h)}{k n_{\max}} \frac{\partial}{\partial n} \left(\int_h^{h_{\max}} n(h') dh' \right) dn. \qquad 2.6.20$$

The last term on the right in Eq 2.6.20 can be simplified. Letting

$$c = \frac{m g}{k} \text{ and } \frac{\partial}{\partial n} = \frac{d}{dn} \Rightarrow dn = \left(\frac{dn}{dh} \right) dh. \qquad 2.6.21$$

The number density n increases with decreasing altitude by the scale height H given by

$$n(h) = n_{\max} e^{-\frac{h_{\max} - h}{H}}. \qquad 2.6.22$$

As such, assuming H is constant,

$$\frac{dn}{dh} = -\left(\frac{n}{H} \right). \qquad 2.6.23$$

And

$$\frac{c}{n(h_{\max})} \frac{\partial}{\partial n} \left(\int_h^{h_{\max}} n(h') dh' \right) dn = \frac{c}{n(h_{\max})} \left[n(h_{\max}) \frac{dh_{\max}}{dn} - n(h) \frac{dh}{dn} \right] = -\frac{c}{n(h_{\max})} \left[n(h_{\max}) \frac{H_{\max}}{n(h_{\max})} - n(h) \frac{H}{n(h)} \right] = -\frac{c}{n(h_{\max})} \left[H_{\max} - H \right]. \qquad 2.6.24$$

The final term is zero for a constant scale height. The temperature variance becomes

$$\sigma_{T(h)}^2 = \left[\frac{n(h_{\max})}{n(h)} \right]^2 \sigma_{T(h_{\max})}^2 + \left[\frac{T(h_{\max})}{n(h_{\max})} \right]^2 \sigma_{n(h_{\max})}^2 + \left[\frac{T(h)}{n(h)} \right]^2 \sigma_{n(h)}^2. \qquad 2.6.25$$

Substituting Eq 2.6.22 into Eq 2.6.25 we find the final calculation of the temperature variance

$$\sigma_{T_h}^2 = T_h^2\left(\frac{\sigma_{n_h}}{n_h}\right)^2 + \left[\sigma_{T_{max}}^2 + T_{max}^2\left(\frac{\sigma_{n_{max}}}{n_{max}}\right)^2\right] e^{\frac{2(h_{max}-h)}{H}}, \qquad 2.6.26$$

where T_h and n_h are the temperature and number density at h, T_{max} and n_{max} are the temperature and number density at the top altitude, h_{max}, and H is the atmospheric scale height, which is assumed to be a constant 7 km. The first term in the equation is derived from the ideal gas law. The second term is based upon the uncertainty of the initial temperature, and decreases with height. Typically, the uncertainty of the starting temperature is unknown and is assumed to be zero as it has a limited range of influence because the exponential term causes it to decrease rapidly with decreasing altitude. Likewise, the uncertainty from the third term also decreases rapidly with decreasing altitude.

7. NLC Observations and Uncertainties

The ice particles that form noctilucent clouds are of comparable size to the transmitted wavelength of atmospheric lidars. This produces a strong Mie scatter signal in addition to the Rayleigh-scatter signal in the altitude region of the NLC. When the profile with the combined signal C_1 is referenced to the Rayleigh only signal C_2 it produces the backscatter ratio,

$$B_R = \frac{C_1}{C_2}, \qquad 2.7.1$$

which is greater than unity where the Mie-scatter contribution exists. Here C_1 and C_2 denote the backscattered photon counts given by

$$C_1 = \left\langle \overline{C_1} \right\rangle^2 = \left\langle \overline{(S+N)_1} \right\rangle_{I_1 J_1} - \left\langle \overline{N_1} \right\rangle_{K_1 J_1} \qquad 2.7.2$$

$$C_2 = \left\langle \overline{C_2} \right\rangle = \left\langle \overline{(S+N)_2} \right\rangle_{I_2 J_2} - \left\langle \overline{N_2} \right\rangle_{K_2 J_2}, \qquad 2.7.3$$

where $S+N$ is the measured combination of backscattered photons, S, and background noise, N. Here I and K are the number of points in the altitude average and J is the number of points in the time average. The brackets and the horizontal bar denote, respectively, that the values have been averaged in time and space (altitude). These expressions are equivalent to Equations 2.6.15, where the altitude average was over I bins for the signal and K bins for the background, and the time average was over J 30-second (bins).

To refine the measurement of the backscatter ratio a normalization factor f is used to account for variations in the atmospheric transmittance and differences in the laser power in the two measurements. The normalization factor for each altitude j is,

$$f_j = \frac{C_{2j}}{C_{1j}}. \qquad 2.7.4$$

It follows that the average normalization factor is

$$\langle f \rangle = \frac{1}{J}\sum_{1}^{J} f_j = \frac{1}{J}\sum_{1}^{J} \frac{C_{2j}}{C_{1j}}, \qquad 2.7.5$$

The first value used in the average is from 45 km and the J^{th} value is from 70 km, which is well below the NLC altitude. The average value for f should be very close to unity and has been included for completeness. So many independent observations contribute to the value of this normalization constant, that its uncertainty is taken to be negligible. Therefore, the best estimate for the backscatter ratio at each altitude, j, becomes

$$B_{R_j} = \langle f \rangle \frac{C_{1_j}}{C_{2_j}}. \qquad 2.7.6$$

Like the previous derivation of uncertainty for the temperature calculation the measurement uncertainty for the Mie scatter is simply dependent upon the photon counts assuming a Poisson distribution. We can therefore define the variations in the backscatter ratio assuming that C_1 and C_2 are independent measurements and that $\langle f \rangle$ is a well-determined constant,

$$dB_r = \frac{\partial B_R}{\partial C_1} dC_1 + \frac{\partial B_R}{\partial C_2} = \frac{\langle f \rangle}{C_2} dC_1 + \frac{\langle f \rangle C_1}{C_2^2} dC_2. \qquad 2.7.7$$

The variance for the backscatter ratio at each altitude then becomes

$$\sigma_{B_r}^2 = \frac{\langle f \rangle^2}{C_2^2} \sigma_{C_1}^2 + \langle f \rangle^2 \left(\frac{C_1}{C_2^2} \right)^2 \sigma_{C_2}^2 = \langle f \rangle^2 \left(\frac{C_1}{C_2} \right)^2 \left(\frac{\sigma_{C_1}^2}{C_1^2} + \frac{\sigma_{C_2}^2}{C_2^2} \right), \qquad 2.7.8$$

where the subscript j has been dropped for convenience. The updated backscatter ratio B_R, Eq 2.7.6 can be substituted back into Eq 2.7.8 to give

$$\sigma_{B_R}^2 = B_R^2 \left(\frac{\sigma_{C_1}^2}{C_1^2} + \frac{\sigma_{C_2}^2}{C_2^2} \right). \qquad 2.7.9$$

The standard deviation then becomes

$$\sigma_R = B_R \sqrt{\frac{\sigma_{C_1}^2}{C_1^2} + \frac{\sigma_{C_2}^2}{C_2^2}}. \qquad 2.7.10$$

The variance in each of the profiles used to calculate the backscatter ratio can be calculated assuming Poisson statistics. The counts are dependent upon the average values of the signal and the background values. The uncertainty in the count rates are similar to those derived for the density calculations, Equation 2.6.16,

$$\sigma^2_{C_1} = \sigma^2_{\langle \overline{C_1} \rangle} = \sigma^2_{\langle \overline{(S+N)_1} \rangle} + \sigma^2_{\langle N_1 \rangle} = \frac{1}{J_1 I_1} \left\langle \overline{(S+N)_1} \right\rangle_{I_1 J_1} + \frac{1}{J_1 K_1} \left\langle \overline{N_1} \right\rangle_{K_1 J_1} \qquad 2.7.11$$

and

$$\sigma^2_{C_2} = \sigma^2_{\langle \overline{C_2} \rangle} = \sigma^2_{\langle \overline{(S+N)_2} \rangle} + \sigma^2_{\langle N_2 \rangle} = \frac{1}{J_2 I_2} \left\langle \overline{(S+N)_2} \right\rangle_{I_2 J_2} + \frac{1}{J_2 K_2} \left\langle \overline{N_2} \right\rangle_{K_2 J_2}. \qquad 2.7.12$$

Short integration times and limited vertical averaging are necessary to accurately represent the NLC properties. As such, the variance in the measurement profile is much larger than the variance from the reference profile and is the limiting factor in the uncertainty.

CHAPTER 3

MID-LATITUDE MESOSPHERIC TEMPERATURE CLIMATOLOGY IN THE MOUNTAIN WEST OBTAINED FROM THE RAYLEIGH-SCATTER LIDAR AT THE ATMOSPHERIC LIDAR OBSERVATORY (41.7° N 111.8° W)[1]

Abstract

Over 900 nights of observations from a Rayleigh-scatter lidar have been reduced and used to derive nighttime temperature profiles between 45 and 90 km spanning the 11-year period from late 1993 through 2004. They have been combined to derive an annual climatology of the temperature and the temperature variability for the mesosphere above Logan, Utah. The variations of temperature with altitude and time are examined. The transition between radiative and dynamical behavior occurs near 63 km. The strong mesospheric inversion layers in winter appear in the results. In altitude, the variability has a minimum below the transition altitude. In addition to winter, the variability has maxima high in the mesosphere near the equinoxes and summer solstice. The temperature climatology is compared to the one from the French lidars at Haute Provence and Biscarrosse obtained between 1984 and 1989. Winter comparisons show large differences, which might have a longitudinal origin. During the summer months below the transition region, the ALO temperatures are systematically ~1.5 K colder than the French temperatures, which might reflect long-term mesospheric cooling.

1. Introduction

The temperature structure of the atmosphere is a very distinctive feature, serving

[1] Coauthored by Joshua Herron and Vicent B. Wickwar.

as the basis for defining the different atmospheric regions. The temperature climatology provides fundamental information about the energetics of the regions and serves as a reference for evaluating first-principle models. It is also a reference for detecting and exploring unusual events or phenomena. Regular measurements of much of the middle atmosphere were very difficult prior to the advent of Rayleigh-scatter lidar. Balloons, which are used in the troposphere and stratosphere, typically reach altitudes less than 30 km. Likewise, special high-flying aircraft have a similar altitude ceiling. Airglow observations only begin above 85 km. Rocket soundings are infrequent because of their expense. Until recently, satellites observations have had poor altitude resolution and, in any case, are unable to provide time evolution above individual locations. Rayleigh-scatter lidar [*Hauchecorne and Chanin*, 1980] changed this situation. Regular observations between 40° and 45° N latitude have been undertaken by the French [*Hauchecorne et al.*, 1991; *Keckhut et al.*, 1993] since 1978, by our group [*Wickwar et al.*, 2001] since 1993, and by the Canadians [*Sica et al.*, 1995] since 1993. Such long-term measurements are necessary to produce good climatologies of temperature and temperature variability. In this paper, we present the mesospheric temperature climatology above Logan, Utah, based on ~5000 hours of Rayleigh lidar observations spanning 11 years. This is the second longest climatology in the 40°-45° mid-latitude region and the one with the densest observations. The lidar and data analysis are described in Section 2; the observations and comparisons are presented in Section 3; and the discussion and conclusions are given in Section 4.

2. Instrument Description and Data Analysis

A Rayleigh-scatter lidar has been operated on the USU campus at the Atmospheric Lidar Observatory, ALO, (41.74°N, 111.81°W, and 1466 m) since August of 1993. The lidar consists of a frequency-doubled Nd:YAG laser operated at 532 nm with a repetition rate of 30 Hz. The initial laser operated with an average power of 24 watts and was replaced by a slightly smaller laser with an average power of 18 watts. The laser is Q-switched to provide a short pulse of ~8 ns. The backscattered light is collected by a 44-cm diameter Newtonian telescope, which gives the system a power-aperture product of 2.7 or 3.6 W-m2 depending on the laser. The light is focused on a field stop, giving a field of view approximately 3 times that of the 1-mrad laser divergence. It is then focused onto the plane of a mechanical chopper and then collimated before passing through a narrow-band interference filter to the cooled photomultiplier tube (Electron Tubes 9954). The basic altitude resolution is 37.5 m, corresponding to a range bin of 250 ns. The returns from 3600 pulses are summed before they are recorded to disk, giving a minimum time resolution of 2 minutes. A more detailed description of the lidar is given elsewhere [*Wickwar et al.*, 2001; *Herron*, 2004].

The lidar returns are composed of backscattered photons, background signal, and dark counts. To protect the PMT from the large, low-altitude signals, a mechanical chopper blocks returns from below 20 km and electronic gating reduces the gain by about 500 below 38 km. Good data are acquired starting at approximately 41 km. At and above this altitude, extinction by aerosols and absorption by O_3 can be neglected. Consequently, the altitude-dependent signal is due only to Rayleigh-scattering and is proportional to density. The returns are measured out to an altitude of 500 k, where the

extended region between 120 and 500 km is used to enable an accurate determination of the background and to provide a diagnostic tool for the detector system. Once a suitable background level is determined and subtracted, the signal is corrected for the $1/\text{Range}^2$ fall off. The resulting profile is proportional to density and can be integrated downward to determine profiles of absolute temperature by assuming the atmosphere is in hydrostatic equilibrium and obeys the ideal gas law [*Hauchecorne and Chanin*, 1980; *Gardner et al.*, 1989]. The temperature profiles are independent of variations in the atmospheric transmittance and do not have to be calibrated. They depend on good observational and analysis procedures.

To calculate the absolute temperature, an a priori knowledge of the temperature at the start of the downward integration is necessary. The initial values were taken from the 8 year climatology from the sodium lidar at Colorado State University (CSU) [*She et al.*, 2000], which is only 575 km away and just over 1° equatorward of ALO. The CSU temperatures were from 1990 to 1999, covering much of the same time period as the ALO data. The use of this climatology to initiate the calculation for the ALO climatology should greatly reduce the uncertainty in the initial values. However, any remaining uncertainty from this initial temperature decreases rapidly with the downward integration.

The starting altitude for the temperature integration is determined as the point where the signal is 16 times its standard deviation. The average starting altitude for the nighttime temperature profiles is 87 km, but even for the best data the maximum altitude is set to 95 km. Any difference between the starting temperature and the actual temperature decreases by a factor of 4 after 10 km of integration. This decrease in

systematic error, coupled with the use of the CSU climatology for the starting values, should ensure that accurate temperatures are obtained for altitudes below 80 km and that reasonable temperature values are obtained even above 80 km.

At the upper limit of the lidar's range, the background becomes a large portion of the total signal. Its accurate determination in the region above 120 km is most important for the data selection, because a bad background leads to systematic temperature errors at all altitudes [*Herron*, 2004]. Observationally, bad backgrounds can have slopes, oscillations, or spikes. To minimize potential background problems, the background region was chosen specifically for each night and each night reduced separately. Subsequent averaging of many nighttime temperatures further reduced any adverse effects from the background selection. Nights were rejected because of low signal strength, typically due to poor viewing conditions. Between 1993 and 2004, observations were obtained on approximately 950 nights; of these, approximately 903 nights were of sufficient quality for temperature reduction. Figure 7 (a and b) show the nighttime temperature measurement from January and July with their associated average and standard deviation. The monthly distribution of the nighttime observations is given in Table 1.

Table 1. Monthly distribution of nightly observations included in the climatology

Month	Nights	Month	Nights
Jan	49	July	118
Feb	62	Aug	126
Mar	85	Sep	114
Apr	56	Oct	86
May	58	Nov	38
June	103	Dec	24

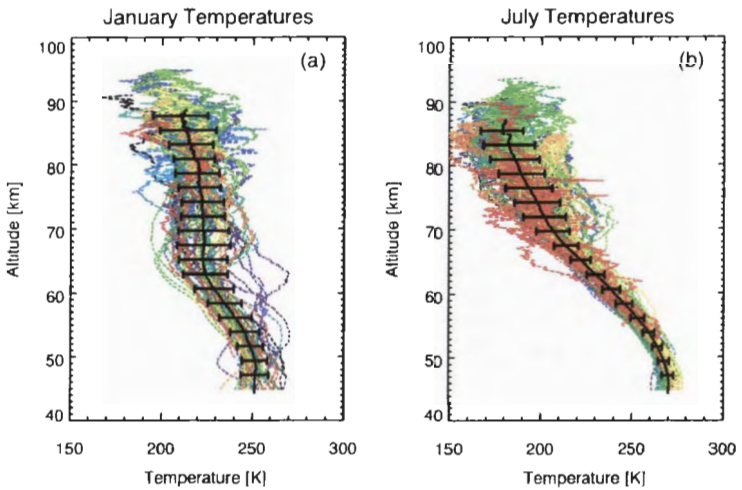


Figure 7. Nighttime temperature averages, collected during the months of January and July. The horizontal error bars are the standard deviation plotted about the average temperature.

An average temperature profile is found for each night of the composite year by averaging the nighttime temperature profiles in a multi-year, 31-day window centered on the particular night of the year. Because each of the nighttime profiles included in the average has a different starting altitude, the maximum altitude for the average is dependent upon the number of profiles available at each altitude. The average is started at 45 km and continues upward until only half of the maximum number of profiles in the 31-day window, remains. Seventy-five percent of the nighttime temperature profiles have starting altitudes between 95 and 84 km with the average starting altitude being ~87 km. The average maximum altitude for the 31-day average works out to be 88 km.

3. Observations and Comparisons

The temperature climatology derived for each day of the composite year is given in Figure 8. The maximum temperature at 45 km is 273 K in June and the minimum is 252 K in January, a 21 K difference. The altitude of the stratopause also varies over the

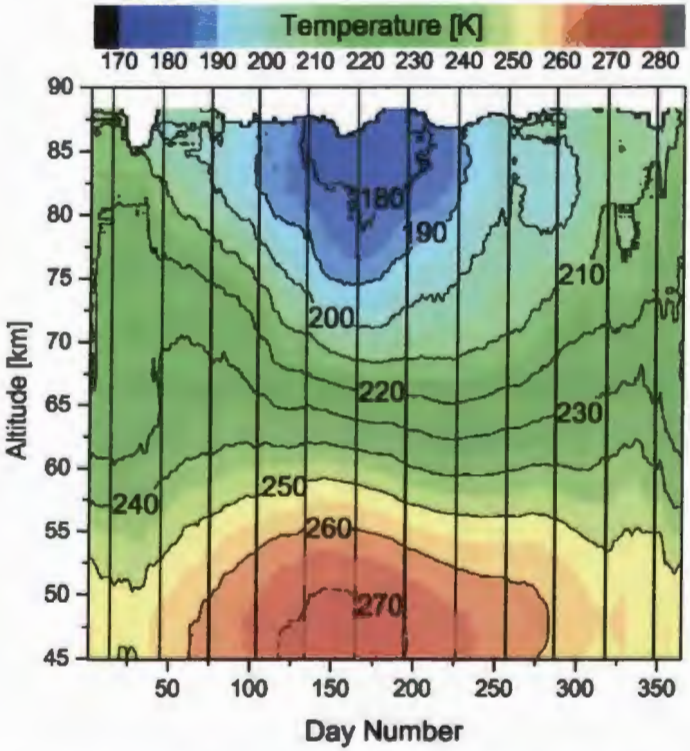


Figure 8. The ALO temperature climatology. The profile for each day of the composite year is the result of a multi-year, nighttime, temperature average over a 31-day window centered on the day. The vertical black lines represent the 15th of each month.

course of the year, at ~ 47 km from September to January, but at or below 45 km during the rest of the year. The warm summer and cool winter of the lower mesosphere at mid-latitudes is the opposite of what is observed in the upper mesosphere. Here the seasonal dependence is reversed with a warm winter and a cool summer, a behavior that is usually attributed to the effect of gravity waves and planetary waves on the global meridional circulation, leading to compressional heating in winter and adiabatic cooling in summer. At 84 km, the summer-winter variation is 42 K with a maximum of 216 K in January and a minimum of 174 K in June. The lowest temperature in the mesopause region appears to be at 81 km in June, but the slope of the profile suggests that the actual mesopause is at a higher altitude.

Because of the 31-day averaging window, independent profiles occur every 31 days, at approximately one-month intervals. Accordingly, 12 profiles representing approximately the 15th of each month were selected and are presented in Figure 9. The uncertainties are based on propagating the uncertainties in the photon counts assuming a Poisson distribution [*Gardner*, 1989]. They do not include an estimate of the uncertainty in the starting temperature, nor of the geophysical variability. Because of the great amount of temporal averaging, the temperature standard deviation of the mean below 84 km is <1 K, with some slight variation from month to month. This set of temperature profiles clearly shows the warm summer and cold winter at 45 km, near the stratopause, and the reverse seasonal behavior at 85 km. The transition between these two behaviors occurs at 63 km, where all months except January and August exhibit almost the same temperature.

The initial impression from Figures 8 and 9 is that the mesosphere is characterized by monotonically decreasing temperatures with increasing altitude. However, despite the great amount of averaging, January and February show inflections, almost reversals, in the lapse rate from mesospheric inversion layers [*Schmidlin*, 1976; *Meriwether et al.*, 1998]. While inversion layers are not a permanent feature of the wintertime mesosphere above ALO, they are observed with enough frequency that they have a significant impact in these two months and a barely discernable impact in December and March. Furthermore, the apparent impact varies, with January temperatures as much as 10 K colder than the February temperatures between 60 and 75

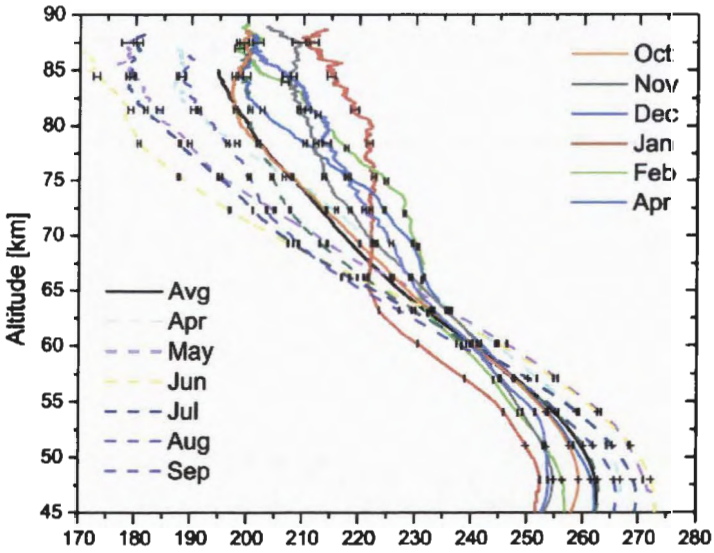


Figure 9. The ALO temperature climatology from Figure 8 presented at 3-km intervals for the 15th of each month. The contour lines are every 5 k.

km and as much as 10 K warmer above that. A large isothermal region between 65 and 75 km in January and a small region between 63 and 66 km in February also is another result of the inversion layers.

Another significant feature is that October and November in the fall have temperature minima near 85 km. This minimum may also occur in the spring in March. These minima are most likely the lower altitude relative minimum in the two-level mesopause [*She and von Zahn*, 1998].

These twelve profiles shown in Figure 9 also provide a combination contour plot and data tabulation at one-month and 3-km intervals, shown in Figure 10. This tabulation is in the tradition of other climatologies [e.g., *Hauchecorne et al.*, 1991; *She et al.*, 2000; *States and Gardner*, 2000b]. It provides values that can be used for future comparisons.

Because the temperatures given in Figures 8 through 10 are heavily averaged, they filter out much of the geophysical variability. However, an estimate of this variability is obtained by calculating the RMS variation or estimated standard deviation of the individual nights relative to their multi-year average in the 31-day window. The differences or variability arise from waves with periods greater than half a day that are not coherent within a 24-hr period, random sampling of episodic events such as inversion layers, year-to-year variability, and a temperature trend. The differences also include the measurement uncertainties. The number of data points included in the RMS calculation varies with altitude. As mentioned previously, the number of profiles at the highest altitude shown is half the maximum number. This measure of the geophysical variability of the mesospheric temperatures is shown in Figure 11. As would be expected, it is much

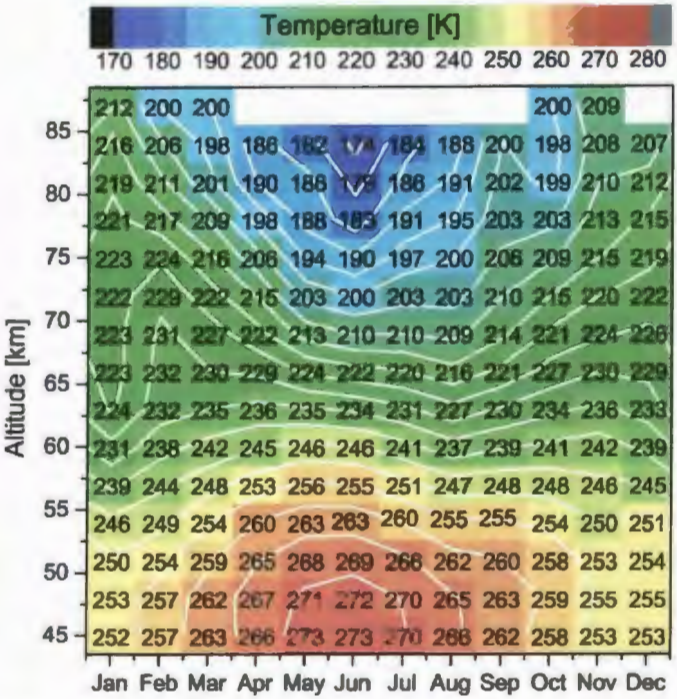


Figure 10. Monthly temperature profiles. Each is the average of the nighttime temperatures in a multi-year, 31-day window. The error bars are derived from the measurement uncertainty assuming Poisson statistics. The annual temperature profile, obtained from averaging the monthly profiles, is also presented.

larger at all times and altitudes than the measurement uncertainty shown as error bars in Figure 9.

The minimum variability is not at 45 km, but is found 3–12 km higher. It is as though there are two sources of variability, one that propagates up from below and is damped out, and one that develops at higher altitudes. The geophysical variability below

the transition altitude is 2–5 K between March and October. During the winter months, from December through February, it increases to 4–13 K, with structure in time and altitude. In those months it has a relative maximum at 45 km, essentially the stratopause. Between 45 and 54 km it is greater in December than in January and February. For December, the variability decreases with a localized minimum of 7 K at 60 km. The variability in January and February decreases slightly with localized minima at 51 km followed by a steady increase with altitude to a local maximum at 69 km of 14 K in January and 11 K in February. These months and the others have local maxima at even higher altitudes. The high variability in winter at these altitudes presumably reflects the inversion layers observed during this period.

Above the transition altitude and between March and October, the variability is typically 4–7 K near the transition region, increasing to 10–14 K by 84 km. Throughout this period, the variability is considerably greater above the transition region than below it. On finer time scales, the variability is also very structured. For instance, above 70 km in July it is significantly greater than in either June or August. Similarly, at and above 78 and 81 km, it is large in March and October, respectively, close to the fall and spring equinoxes. In December, it is significantly greater than for the other months above 70 km, reaching 14–15 K. This large value probably arises from the great inter-annual variability during winter and the relatively few observations during this month.

It is instructive to compare the ALO lidar climatology to the only other published Rayleigh-scatter lidar climatology from the 40°–45° mid-latitude region with tabulated results. It is from the French Rayleigh-scatter lidars located at the Haute Provence Observatory, OHP, (44°N, 6°E) and at Biscarrosse, BIS, (44°N, 1°W). Their

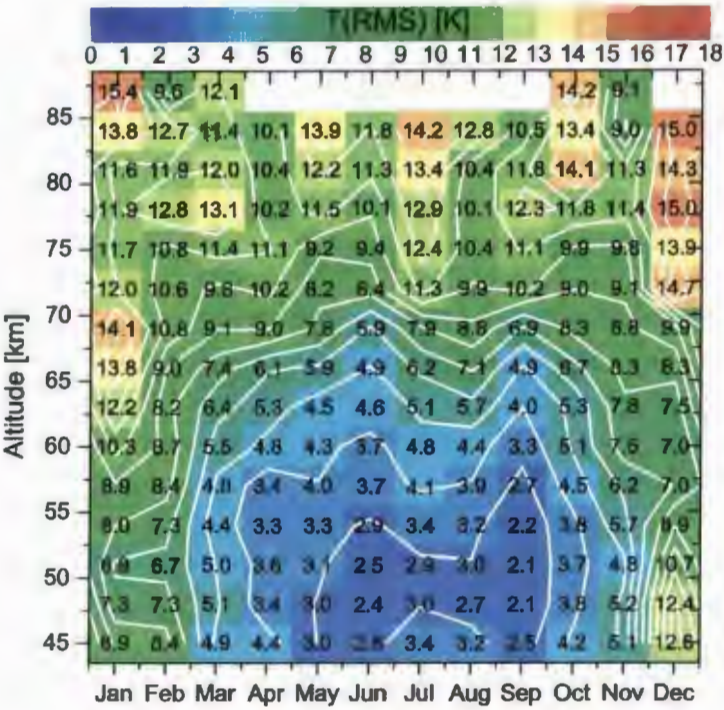


Figure 11. The ALO climatology of observed temperature standard deviations presented at 3-km intervals for the 15th of each month. The contour lines are every 2 K.

temperatures have been combined into a single temperature climatology [*Hauchecorne et al.*, 1991]. While the ALO and French results are from almost the same latitude, they are from different longitude regions separated by almost 120°. In addition, the midpoints of the two data sets are separated in time by just over 12 years. The difference between the ALO and French temperature climatologies are shown in Figure 12. These

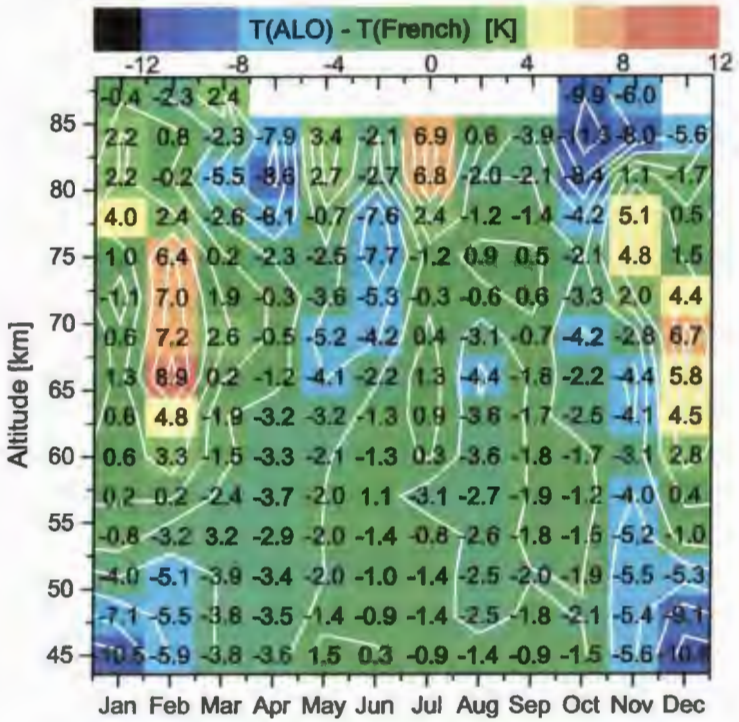


Figure 12. Temperature differences between the ALO and the French climatologies presented at 3-km intervals for the 15th of each month. The contour lines are every 1 K.

differences should be highly significant. An important point about the lidar technique, as already mentioned, is that the temperatures are absolute: no calibration is needed. The impact of the initial temperature value on the downward integration in the data reduction is minimal after 10 km or so. At these altitudes, above 45 km, the overlap function for the laser beam and telescope field of view is unity. (It only becomes significant at much

lower altitudes or for bistatic systems.) Finally, in both locations, the observations are at nighttime, often extending through the whole night. This minimizes potential geophysical differences from migrating tides.

The most striking feature is that between March and October and below the transition region, the temperature differences are systematically between −1 and −4 K, the ALO temperatures being less than the French temperatures. In the winter months, including November, the differences increase to between −5 and −11 K near 45 km, but become positive in December through February by up to 3 K by the transition altitude. In January the differences remain small at higher altitudes, presumably indicating similar sized inversion layers. However, in February and December, the differences reach 7–9 K just above the transition altitude. They presumably reflect a larger positive phase in the inversion layers at ALO.

Between March and October above the transition region, the ALO temperatures are on average slightly colder than the French temperatures, but with considerable structure in time and altitude. Above 75 km, the differences reach −9 K in April and October, while they reach almost 7 K in July.

4. Discussion and Conclusions

We have presented mid-latitude climatologies of nighttime mesospheric temperatures and of their variability derived from nighttime Rayleigh-scatter lidar measurements at ALO. With over 5000 hours of data from over 900 nights, the most of any published lidar climatology, this analysis has the best opportunity for extracting the basic features from various sources of variability. This ALO climatology is important for

investigating the vertical structure of the mesosphere, temporal variations, longitudinal differences, and long-term trends. In addition, the climatology is important as a reference for identifying and investigating special or unusual events. To facilitate others using these climatologies, they are presented, in part, in tabulated form.

Near the stratopause and in the lower mesosphere, the temperatures have a maximum in summer and minimum in winter, consistent with radiative control. At 45 km, this difference is 21.0±0.4 K. High in the mesosphere the temperatures have a maximum in winter and a minimum in summer, consistent with dynamical control. At 84 km, this difference is 42.5±1.3 K. This winter temperature maximum appears to propagate down from January to June. A crossover or transition altitude with minimal seasonal variation occurs at 63 km. The mesospheric inversion layers are frequent, strong, and consistent enough in December through February that they appear in the temperature climatology.

As for using the climatology to examine special events, NLCs were observed above Logan, Utah, on two occasions [*Wickwar et al.*, 2002; *Herron et al.*, 2007] (see Chapter 5). For the 1995 event, comparison of the observed temperatures to the climatological temperatures for June showed that the NLC occurred at the minimum of a large temperature oscillation, which behaved similarly to an amplified diurnal tide.

Great variability in altitude and time occurs for the observed standard deviations. In general there is a relative maximum at 45 km, near the stratopause. It then decreases to a minimum and increases again at higher altitudes. Between December and February, this low-altitude variability is the order of 10 K, consistent with the upward propagation of planetary waves. However, significant variability on the order of 3 to 4 K also occurs

throughout the rest of the year, presumably because of upward propagating waves. Throughout much of the year, this variability diminishes by the order of a degree within the next 6–12 km, suggesting that the waves with periods greater than a day, are dissipating. In winter, because of the MILs, this variability then grows with altitude to 15 K. The occurrence of inversion layers appears to be closely related to the large stratopause variability. They have been shown to be closely related to large amplitude diurnal tides and planetary waves [*Nelson and Wickwar*, 2007]. An interannual component of this variability, which is apparent in the annual temperatures, may account for why the ALO January 1995 temperatures exceeded those from other sources in a comparison with WINDII temperatures [*Shepherd et al.*, 2001]. During the rest of the year, the variability starts to increase just below the transition region and continues to do so to the highest altitudes, occasionally reaching as much as 14 K. While the variability increases with altitude, the rate of increase appears to slow down in the last 3 to 6 km. While this may be real, it may also reflect that some of the profiles used for the average had their initial values at altitudes close to these.

In addition, there is considerable variability in time. Maxima near the two equinoxes high in the mesosphere, Figure 11, may account for the so-called equinox transition periods [e.g., *Taylor et al.*, 2001; *Shepherd et al.*, 2004b]. The timing suggests that they arise because the zonal wind of the mesospheric jet, which filters out the upward propagation of gravity waves, goes back and forth through zero as the mesospheric jet transitions from eastward to westward in late March and from westward to eastward in late September. Without the jet, more gravity waves grow to a large amplitude before breaking at these higher altitudes. In July, and perhaps late June, another maximum

occurs. In Chapter 5, the existence of large amplitude temperature waves, which appear to come from the interaction of gravity waves and the diurnal tide, was established in the upper mesosphere. If these enhanced waves are a common feature of the summer mesosphere and only persisted for a few days, they would contribute directly to this variability. They could also contribute indirectly by affecting the upward propagation of gravity waves, which would affect the adiabatic cooling.

The comparison with the French temperature climatology [*Hauchecorne et al.*, 1991] shows both significant similarities and differences. In general, very similar temperature behavior is exhibited in both climatologies (see Figure 12). However, the ALO temperatures are systematically cooler than the French temperatures. For the well behaved data below the transition altitude and excluding the winter period from November through February, it is useful to look for trends over the 12.3 years between the mid points of the two data sets. In the summer, May through August, between 45 and 63 km, the average temperature difference is −1.46 K, suggesting a trend of −1.2±0.2 K per decade. In the equinox periods, March, April, September, and October, in the same altitude region, the average temperature difference is −2.21 K, suggesting a 50% greater trend of −1.8±0.2 K per decade. (In both cases, the uncertainty is the standard deviation of the mean.) Thus, there appear to be significant cooling trends. The summer trend is similar to what has been deduced in other ways [e.g., *Beig et al.*, 2003] and attributed to climate change. The equinox trend, though larger, is consistent with some results suggesting different trends in different seasons [e.g., *Beig et al.*, 2003]. However, other factors, which might argue against a trend attributable to climate change, need to be examined. While the ALO data span an 11-year solar cycle, the French data only span

about half a solar cycle. However, the average F10.7 solar index is similar for the two periods, 123 for the ALO period and 115 for the French period. And, there is little evidence for a strong temperature dependence on solar flux in this altitude region [e.g., *Keckhut*, 1995; *Keckhut et al.*, 1995]. This supposed trend then is probably not a significant factor.

Another consideration is that both data sets were acquired starting shortly after major volcanic eruptions—El Chichon in 1982 and Mt. Pinatubo in 1991. Several results indicate the possibility of significant heating for a few years after a major eruption [e.g., *Keckhut et al.*, 1995; *She et al.*, 1998; *She et al.*, 2000] followed by cooling. Because the French data is a shorter dataset, the influence of the heating may appear more pronounced in this dataset.

Another consideration is the large longitudinal separation, almost 120°, which puts the two lidars in very different topological regions—ALO in the Mountain West and the French lidars to the east of the Atlantic Ocean. This could significantly affect the orographic generation of gravity waves in the troposphere and their subsequent interactions with tides and planetary waves. That this might happen is suggested by the significant difference in size and altitude of the MILs in December, January, and February, and by NLCs having been observed twice in summer at ALO [*Wickwar et al.*, 2002; *Herron et al.*, 2007] (see Chapter 5), but apparently not by the French lidars. It also might be a factor in the greater differences at the equinoxes. To distinguish between the effects of climate change, volcanic activity, and longitudinal differences, a comparison between temperatures from the two lidars using more contemporaneous data will be needed.

While much has been learned from this extended mesospheric dataset from ALO, many questions have been raised that require new and improved data. These include the possibility of significant longitudinal variations and of significant long-term trends. The atmospheric system is variable enough that long-term observations are needed to properly separate any long-term trends from other variations. Frequent observations are also needed to observe and then examine additional special or unusual events. A more powerful or more sensitive lidar system is needed to improve the temperatures in the upper mesosphere and to extend the observations across the mesopause into the lower thermosphere. Downward extensions of the lidar detector system are needed to relate mesospheric temperatures and variability to temperatures and variability in the tropospheric and stratospheric source regions. A daytime capability is needed to find a mesospheric climatology as opposed to a nighttime mesospheric climatology.

CHAPTER 4

A COMPARISON OF MID-LATITUDE MESOSPHERIC TEMPERATURES— THE ALO LIDAR CLIMARTOLOGY AND THE NRL EMPIRICAL MODEL[2]

Abstract

The temperature climatology from the Rayleigh-scatter lidar at the Atmospheric Lidar Observatory, (ALO), operated by the Center for Atmospheric and Space Sciences on the campus of Utah State University (41.74° N, 111.81° W) at an altitude of (1465.8 m) has recently been published (Chapter 3). The Rayleigh-scatter lidar technique provides absolute measurements of temperature and serves as an excellent reference for comparisons. The Naval Research Laboratory MSIS--00 empirical model calculated for the ALO location and time periods is compared to the ALO climatology. The comparison shows that the model captures the average temperature structure, with an average annual difference of less than 5 K over much of the mesosphere. However, the model fails to reproduce or fails to correctly reproduce some significant features in the ALO climatology: the winter mesospheric inversion layers are not shown; the apparent summer mesopause temperatures are 11 K cooler than the climatological values and the minimum occurs 17 days earlier; the summer maximum near the stratopause at 45 km is 273 K in agreement with the climatology, but then occurs 10 days earlier in the model. The spectral composition of the temperatures shows additional differences: the strong annual amplitudes and the phases show relatively good agreement except for the model exhibiting the opposite phase progression with altitude through the phase reversal near 63

[2] Coauthored by Joshua Herron and Vincent B. Wickwar

km; the semi-annual amplitudes and phases are very different, with the model being up to 127 degrees out of phase with the climatology; and the model does not include the higher order harmonics that exist in the climatology.

1. Introduction

Measurements of the temperature structure of the middle atmosphere provide information about the energetics in the region, the roles of radiative heating and cooling, of chemical heating, and of dynamical heating and cooling. Much of the dynamics are related to the generation, filtering, and breaking of gravity waves, tides, and planetary waves. These waves in turn drive the general circulation giving rise to an inter-hemispheric flow that leads to adiabatic heating in winter and cooling in summer in the upper mesosphere. Several observational techniques are used to make temperature measurements in the middle atmosphere.

The Rayleigh-scatter lidar technique, in particular, provides temperature measurements over much of the mesosphere with high temporal and vertical resolution. Temperature profiles derived from these observations make an ideal reference as they are absolute temperatures, independent of any system calibrations. The earliest climatology of Rayleigh-scatter temperatures was obtained by *Hauchecorne et al.* [1991]. While these mid-latitude observations began in 1978, the climatology depended on the data from 5 years, 1984 to 1989. Recently another mid-latitude temperature climatology based upon Rayleigh-scatter lidar measurements has been published. The Atmospheric Lidar Observatory (ALO) at Utah State University (USU) was used to produce an 11-

year, mid-latitude climatology of Rayleigh-scatter lidar temperatures that span the period from 1993 to 2004, see Chapter 3 and *Herron* [2004].

The vast majority of ground-based measurements are done at fixed installations which can also be said for sounding rockets. To develop a comprehensive, global picture of the middle atmosphere, it is necessary to combine these sparse observations with satellite observations into an empirical model. Such models have been of considerable importance for geophysical research. In particular, the empirical models have been used to validate new measurements and first principle models [*Roble and Ridley*, 1994; *Roble*, 1996; *Meier et al.*, 2001]. In addition, several Rayleigh-scatter lidars along with a few satellites have used empirical models for the initialization temperature for their data reductions [*Clancy and Rusch*, 1989; *Hauchecorne et al.*, 1991; *Clancy et al.*, 1994; *Sica et al.*, 1995; *Fiedler et al.*, 1999; *Shepherd et al.*, 2001; *Collins et al.*, 2003]. The most recent version of the MSIS series of empirical models, MSIS–00, is derived from a collection of historical observations [*Picone et al.*, 2002] between the surface and the thermosphere. This model, along with its predecessors, suffers from a dearth of observations in the middle atmosphere, particularly between 30 and 85 km. It is therefore important to compare this model to existing, independent, middle atmosphere climatologies. Accordingly, we are comparing the MSIS–00 model to the ALO lidar climatology.

In this paper we compare nighttime temperature averages from the MSIS–00 empirical model to the ALO temperature climatology. The comparison includes an analysis of the temperature differences and a comparison of the 12, 6, 4, 3, and 2.4 month oscillations found in each. The ALO Rayleigh-scatter lidar and climatology are

described in Section 2. The MSIS–00 model and the temperature-generation method are described in Section 3. The model temperatures are compared to the climatological temperatures in Section 4. Conclusions are given in Section 5.

2. Atmospheric Lidar Observatory

2.1 Rayleigh-Scatter Lidar

A Rayleigh-scatter lidar has been operated on the USU campus by the Atmospheric Lidar Observatory, ALO (41.74° N, 111.81° W), since August of 1993. The recent climatology, Chapter 3, used ~5000 hours of lidar observations that had sufficient quality to produce accurate temperatures at high altitudes. The Rayleigh-scatter lidar technique relies on elastic scatter of a transmitted laser pulse at the incident wavelength from molecular nitrogen and oxygen. The lidar returns are composed of these backscattered photons, background signal from the sky, and PMT dark counts, Figure 13(a). To protect the PMT from the large, low-altitude signals, a mechanical chopper blocks the returns from below 20 km. In addition to the mechanical chopper, electronic gating also reduces the gain by ~1000 below 38 km with good data typically acquired above 41 km. At and above this altitude, extinction by aerosols and absorption by O_3 can be neglected. Consequently the altitude-dependent signal is due only to Rayleigh-scattering and is proportional to the molecular number density. The returns are measured out to an altitude of 540 km, where the extended region between 120 and 500 km is used determine an accurate background level and provides a diagnostic tool for the detector system. Once a suitable background level is determined and subtracted, the signal is corrected for the $1/R^2$ fall off, where R is the range from the lidar. The resulting profile is

proportional to density and can be integrated downward to produce profiles of absolute temperature by assuming the atmosphere is in hydrostatic equilibrium and obeys the ideal gas law [*Hauchecorne and Chanin*, 1980; *Gardner*, 1989]. This technique requires an initialization temperature at the start of the downward integration. For the ALO climatology, initial temperatures are taken from the sodium lidar climatology from Colorado State University (CSU) [*She et al.*, 2000]. A more extensive description of the lidar is given in [*Wickwar et al.*, 2001; *Herron*, 2004].

As previously mentioned, the Rayleigh-scatter lidar technique relies on range-resolved backscattered photons. The total photon counts are a combination of these backscattered photons, photons from the background sky, and any dark counts from the photomultiplier tube. The nighttime temperature average for July 14, 1995 is shown in Figure 13(b), along with the associated measurement uncertainty in Figure 13(c).

Also as previously mentioned, the starting point for each nighttime average is the point where the signal is 16 times its own standard deviation. Because of that, the uncertainty at the starting point is similar from one night to the next, but the altitude of the starting point varies from night to night, because it is dependent upon the length and quality of the night's observations. At the initialization point the temperature uncertainty, based solely on the measurement uncertainty, is ~11 K. As the temperature profile is integrated downward the temperature uncertainty decreases with the associated increase in signal due to the increase in density and decrease in range. The uncertainty in a nighttime profile will decrease to ~4 K after 5 km and ~2 K after 10 km. The uncertainties illustrated in Figure 13(c) are fairly typical for an individual night.

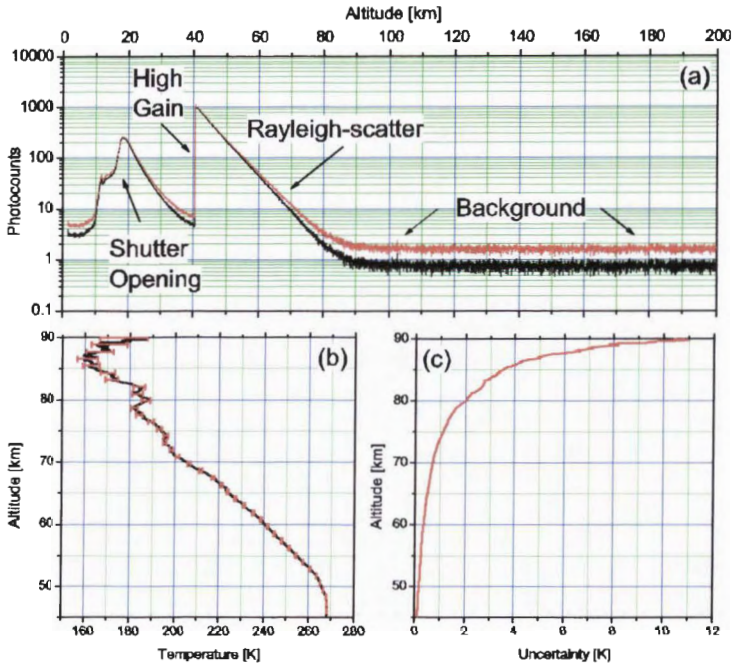


Figure 13. Data collected on 95-07-14 (a) is a nighttime average of the lidar photocount profiles. The opening of the mechanical shutter is visible along with the change of the PMT gain near 38 km. The Rayleigh-scatter region along with the background region is also indicated. The black curve is the average photocount profile with the associated error bars. (b) Average temperature profile with associated error bars for the night's observations. (c) Uncertainty for the temperature profile, (b), are given separately shows the strong altitude dependence of the uncertainties.

The temperature used to seed the temperature reduction also introduces an unknown uncertainty in the temperature profiles. As previously mentioned, the starting temperatures are taken from the climatology from the CSU sodium lidar [*She et al.*,

2000]. Fortunately, the uncertainty due to the starting temperature is range dependent and as the profiles are integrated downward the uncertainty decreases rapidly. As a result, the top 10 km of the ALO climatology are influenced by the CSU climatology.

Alternatively, the seed temperature can be taken from the MSIS–00 model directly. This would result in the temperatures at 85 km being approximately equal to those from MSIS–00. However, as previously mentioned the influence is range dependent and decreases significantly with altitude. The two starting temperatures result in a 4 K temperature difference at 80 km and diminishes to less than 1 K by 74 km. Thus, changing the initial temperatures would have little effect on the comparisons, especially below 75 km.

As the CSU and ALO facilities are separated by only ~575 km we do not suspect the climatological temperatures above ALO to be significantly different than those above CSU. (On a given day, however, they might differ significantly because of wave activity.) Given, the large overlap in the observing periods the CSU climatology provides more appropriate starting values for the ALO climatology than MSIS–00.

2.2 ALO Climatology

The temperature climatology is composed of the nighttime temperature profiles measured by the lidar. They are initiated at the altitude where the signal drops to sixteen times its own standard deviation, which is on average 87 km with a maximum altitude of 95 km. They are averaged over a moving 31-day window, without regard to year, generating a single composite year. The maximum altitude for each day of the composite year is dependent on the starting altitudes of the individual nights. The averaging is

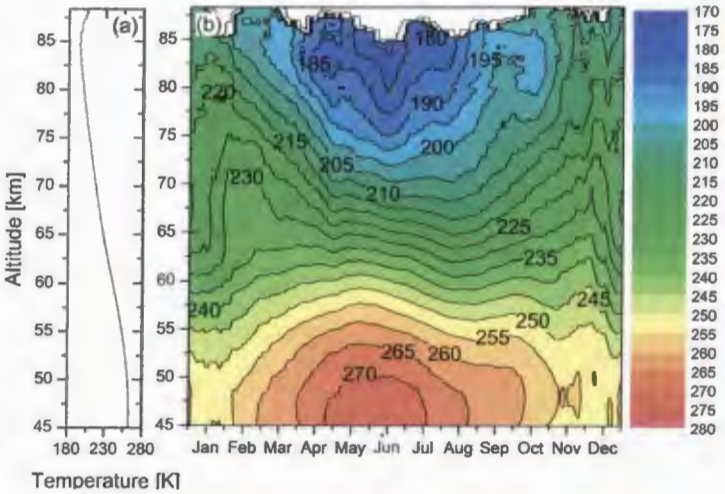


Figure 14. The ALO temperature climatology. The profile for each day of the composite year is the result of a multi-year, nighttime, temperature average over a 31-day window centered on the day. Contour lines are every 5 K.

started at 45 km and is continued upward until half the total number of profiles remain. For reference, Figure 8 has been reproduced here as Figure 14.

Near the stratopause the ALO climatology has a maximum temperature of 273 K at 45 km that extends from late May to early July. As this peak region is not centered about the summer solstice, June 21st, this suggests that the temperatures are modified by a weak semi-annual oscillation. The temperature varies by 21 K during the year at this altitude with a minimum of 252 K. In the upper mesosphere the temperature minimum for the climatology, 172 K, is found at 85 km in mid June. While the upper mesosphere is nearly 180° out of phase with the lower mesosphere, it also has a strong annual oscillation. During June when the temperatures are sufficiently cool, at 85 km, the

mesopause descends into the range of the lidar. The occurrence of the minimum in summertime and maximum in wintertime is indicative of the effects of gravity waves and planetary waves on the global meridional circulation, leading to adiabatic cooling in summer and compressional heating in winter.

In the middle mesosphere, near 60 km, the temperature structure has very little annual variation, but a strong semi-annual component as indicated by peaks in both May and November. The temperature peaks however are not symmetric about the summer solstices and the temperature of the November peak is significantly warmer than that in May. The difference in the peak temperatures and the smaller peaks suggest the presence of higher order oscillations.

A common feature observed in the winter nighttime temperatures above ALO are mesospheric inversion layers or MILs [*Schmidlin*, 1976; *Hauchecorne et al.*, 1987; *Whiteway et al.*, 1995; *Meriwether et al.*, 1998; *Meriwether and Gerrard*, 2004]. While the inversion layers are not a permanent feature of the winter, nighttime temperature profiles, they are observed with enough frequency that they have left a discernable impact on the ALO winter climatology, namely an isothermal region between 65 and 70 km in February.

The temperature variations in the upper portion of the climatology, above 75 km, are very chaotic with several short warming and cooling periods in addition to the general temperature variations. In this region the first strong cooling occurs in early February and extends into late April with periods of cooling rates greater than 15 K/month. A short period of warming is observed in late June, but the first significant heating is from August to mid-September with a heating rate greater than 10 K/month above 80 km. A

second heating period occurs between mid-October and mid-November with a heating rate greater than 15 K/Month. These two periods are separated by a region of constant temperature. The lower portion of the climatology, 45 to 65 km, is less variable with a general warming occurring between January and May and a general cooling between July and December. The exceptions occur during the winter months. In particular there is a very strong cooling trend in December centered around 65 km, followed by a very strong warming trend in January.

The temperature climatology is composed from a running 31-day average of the nighttime temperature profiles. Each of the nighttime averages has an associated uncertainty profile based on the above measurement uncertainty. For each of the 31-day temperature averages, the standard deviation of the mean was calculated. In the same manner as in the temperature calculation, the standard deviation of the mean calculation started at 45 km and continued upward until half of the total profiles were included. The average value for the 31-day standard deviation of the mean is given in Figure 15(a), and the associated contour plot of the 31-day values is shown in Figure 15(b). At 45 km the temperature uncertainty is on average less than 0.2 K. On average, the temperature uncertainty is very small. Looking at the contour profile, Figure 15(b), the standard deviation of the mean for each 31-day period is less than 1 K below an altitude of 80 km.

3. MSIS–00 Empirical Model

3.1 MSIS–00 Model Description

The MSIS–90 empirical model is an extension of the MSIS–86 model of the

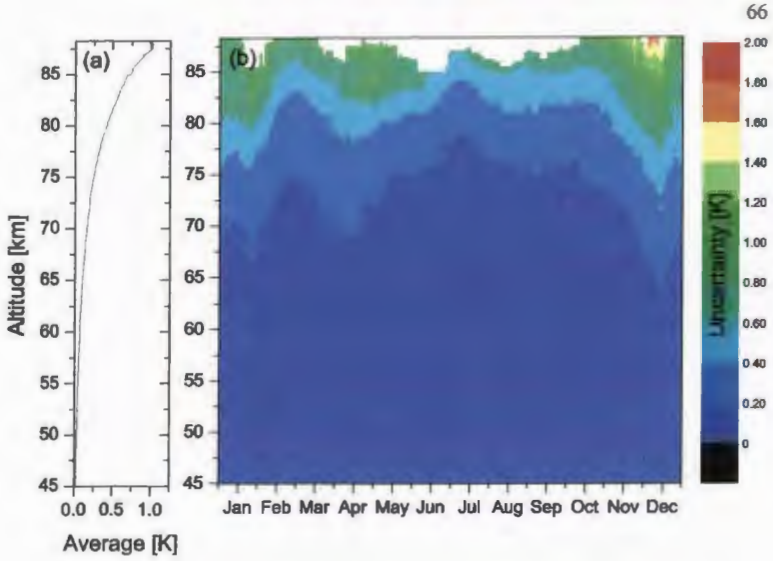


Figure 15. An average of the standard deviation of the mean for the year composes plot (a). The contour plot is composed of the standard deviation of the mean for each 31-day period.

thermospheric temperature, density, and composition into the lower atmosphere [*Hedin*, 1987, 1991]. The recent release of the MSIS–00 empirical model builds on the previous iterations [*Picone et al.*, 2002]. In the mesosphere, the MSIS database, to a great extent, remains unchanged. The database contains the same dataset as the MSIS–90 model, based on the zonally averaged satellite observations (limb and nadir viewing IR) compiled by Barnett and Corney [*Barnett and Corney*, 1985] that became the basis of the low-altitude portion of the CIRA–1986 model [*Fleming et al.*, 1990] and on the MSIS–86 thermospheric model [*Hedin et al.*, 1988] that became the high-altitude portion

of the CIRA–86 model. The database also includes results from balloon-borne observations (radiosondes), rocket-borne instruments (grenade detonations, falling spheres, pressure gages, and mass spectrometers), high-latitude Na lidar, accelerometers on the space shuttle, and 90-130 km data from incoherent-scatter radars. The full data set includes data acquired between 1947 and 1986, but the core satellite data set comes from 1973-1981 [*Barnett and Corney*, 1985]. The database for the thermosphere was expanded for the MSIS–00 model by including measurements from satellite drag, accelerometers, solar occultation measurements, and additional incoherent-scatter radar measurements of both thermospheric and exospheric temperatures. For the mesosphere the dataset remained the same. The physical assumptions were modified between the two versions in that the region where hydrostatic equilibrium is assumed was extended upward to include the region between 80 and 300 km in MSIS–00. One result of this change discussed by *Picone* [2002] is the presence of inflections in the winter temperature profiles that are reminiscent of a MIL.

3.2 MSIS–00 Composite Year

The effects of variations in the solar input have little influence on the temperature profiles in the mesosphere. For comparison with the ALO climatology a similar composite year was created with the MSIS–00 model temperatures. The model temperatures were calculated hourly for each hour of each day that the lidar was in operation between 1993 to 2004. These hourly temperature profiles were then averaged to create nighttime averages corresponding to the nighttime averages used to form the ALO climatology. This averaging was done to remove any tidal offsets that could arise

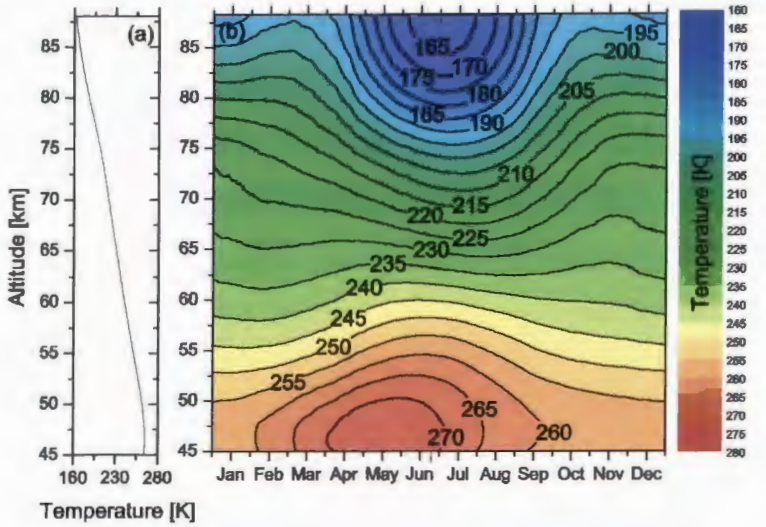


Figure 16. MSIS–00 composite nighttime year. The profile for each day of the composite year is the result of a nighttime temperature average over a 31-day window centered on the day. Contour lines are every 5 K.

between the ALO climatology and a nighttime average of MSIS–00 and to weight the days in the MSIS–00 average in the same way as in the climatology. These nighttime temperature profiles were then averaged over the same 31-day window as the climatology. This process was applied to each day of the year thereby forming a composite year similar to that produced for the ALO climatology, shown in Figure 16. The annual average temperature profile is shown in Figure 16(a) and the contour plot in Figure 16(b).

The temperatures from the MSIS–00 model show a strong annual signature at the stratopause. At 45 km the minimum to maximum temperature variation is ~20 K

between 254 and 274 K. The temperature maximum associated with the stratopause is above the 45-km level for the entire composite year. The model calculations were carried out to 88 km to match the range of the ALO climatology. While no mesopause is present, the minimum mesospheric temperature is 161 K at 88 km on day number 180. At 88 km the semi-annual signature is clearly present in addition to the large annual term. The two peaks in the temperature are on day numbers 65 and 306 respectively.

Near 65 km the temperature variation in the model composite year reaches a minimum. Two peaks are evidence of an increasing apparent semi-annual oscillation with maximums in April and November. However, the peaks are asymmetric in that the November temperatures are greater than those in April. This asymmetry in the temperature peaks continues into the upper mesosphere.

The upper mesosphere above 75 km in the MSIS–00 model shows a strong period of cooling, greater than −10K/Month, occurring in April/May. The warming period in the same region is of the same magnitude as the cooling but occurs in August/September. The temperature structure as a result is very symmetric about the summer solstice. The lower portion of the mesosphere is not as symmetric with the warming occurring mainly in March/April with a slower cooling from May/June until December/January.

4. Comparison of Composite Years

4.1 Temperature Difference

To quantitatively compare the MSIS–00 model to the ALO climatology the climatology temperatures were subtracted from the model. The average temperature differences are given in Figure 17(a). This average shows that the model is

systematically warmer than the climatology between 45 and 51 km. The local minimum at 46 km is ~ −2 K. Between 51 and 61 km the model shows cooler temperatures than the climatology with a local maximum at 55 km of approximately 2 K. The region between 61 and 78 km shows model temperatures warmer than the climatology with a maximum difference of −4 K at 72 km. Above 78 km the model becomes increasingly cooler than the climatology with the average difference reaching 8 K at 85 km near day number 180.

Between 51 and 61 km the model is on average up to 2 K cooler than the climatology. A closer look at Figure 17(b) shows that there are two regions that are significantly cooler. The first extends from February and late June and has a maximum of −6 K. The second extends from early September to mid-December and has a maximum of −4 K. The increase to the summer maxima is later in the model than in the ALO observations accounting for the first period The second period of cooling can also be attributed to a temperature increase in the climatology that is not apparent in this altitude range in MSIS-00.

The differences for the 31-day averages are given as a contour plot in Figure 17(b), with the maximum differences between the two composite years being greater than 15 K. There is a noticeable structure to the temperature differences with large negative and positive departures from the climatology.

As previously mentioned, the model is on average warmer than the climatology, between 45 and 51 km by up to 3 to 5 K. The exception is a four month period from mid-June to mid-October when the model is up to 2 K cooler than the climatology. The maximum temperatures in this region are 274 K for the model and 273 for the

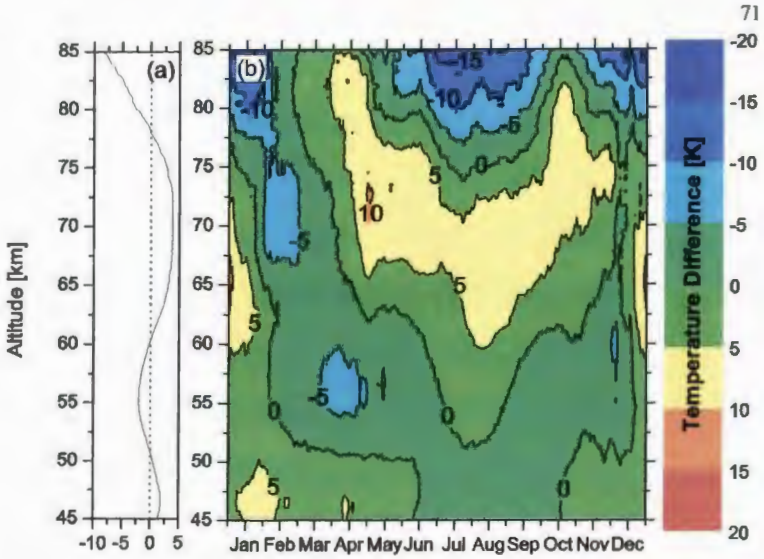


Figure 17. ALO/MSIS–00 temperature differences. (a) Average annual temperature difference. (b) The MSIS–00 composite year temperatures have the ALO climatology subtracted from them. Contour lines are every 5 K. Blue indicates regions where MSIS is cooler than ALO and red warmer.

climatology during the May/June period. However, the model reaches its maxima 10 days prior to the climatology, day numbers 137 and 147, respectively. This offset extends the region where the model is warmer than the climatology. The cooling in the stratopause temperature after the summer solstice is faster in the model than what is observed from the climatology. The temperatures reach 260 K, for example, in late September in the model but not until mid-October in the climatology. The faster onset and the offset of the maxima extend the region where the model is cooler than the climatology into mid-October. The coolest temperatures in this range differ by 7 K, and

are 249 K for the climatology and 256 K for the model. These minima occur in late January for the climatology and early January for the model. The 7 K difference, in addition to the temporal offset, creates the ~5 K region in January/February from 45 to 50 km.

From 61 to 78 km there is a single region from mid-January to late March where the model is significantly cooler than the climatology. For the rest of the year the model is typically warmer than the climatology with the largest difference, greater than 10 K, occurring in early May. Above 78 km, there are two regions where the model is cooler than the climatology. The winter period extends from early November to mid-March and a summer period from May to October. The greatest differences are found in late December, mid-January, and July with temperatures of the climatology warmer by more than 15 K than the model. During the summer solstice the mesopause descends into the range of the ALO lidar. The maximum temperature difference during this period at 84 km is ~17 K, significantly greater than the 11 K difference in the minimum mesopause temperatures. The equinox periods show relatively good agreement in comparison.

4.2 Annual, Semi-Annual, and Higher Order Cycles

The ALO climatology and the MSIS model show structures that are not simply centered on 21 December and 21 June, or any other dates 6 months apart. The asymmetries and secondary maxima suggest that other harmonics in addition to the annual term are present. To look for these differences, the average, annual, and semi-annual components from the two composite years were separated by fitting the results to a function of the form:

$$T(t,z) = T_0(z) + \sum_{n=1}^{4} T_n(z)\cos\left(\frac{n\,2\pi[t-\Phi_n(z)]}{365\ days}\right) \qquad \text{Eq 4.4.1}$$

where T_0 is the average and T_n and Φ_n are the amplitude and phase of the annual and the higher order terms (6-month, 4-month, 3-month, and 2.4-month). A Levenberg-Marquardt least-squares fit was used to find these terms. The standard deviation of the mean, Figure 15(b), was used to appropriately weight the fit to the ALO climatology. For every day of the MSIS–00 composite year, temperatures and equal weightings were used. The averages, T_0, found from the fitting routine were equivalent to the annual averages of the composite years shown in Figures 14(a) and 16(a). The annual and semi-annual oscillations are shown in Figure 18(a-d). In addition to the annual and semi-annual variation, the 4-month, 3-month, and 2.4-month periods were included and are shown in Figure 19(a-f).

There is relatively good agreement in the amplitude and phase of the annual terms for ALO and MSIS–00, Figure 18 (a and b). At the lowest altitude, 45 km, the amplitudes of the annual terms are 9 K and 10 K for MSIS and ALO, respectively. There is a minimum in the amplitude of the annual cycle for both ALO and MSIS–00 at 64 and 63 km. For MSIS–00, the amplitude approaches zero whereas for ALO it is ~2 K. The amplitude from MSIS–00 remains smaller than for the ALO climatology below 78 km. Between 80 and 85 km both the model and the climatology have maximum amplitudes of ~17 K. The phasing of the annual terms is such that it occurs during the summer in the lower mesosphere and the winter in the upper mesosphere as expected. At 45 km there is a difference in the phase between MSIS–00 and ALO with the model leading by 24 days, day numbers 144 and 168, respectively. By 60 km, the reverse is true with the

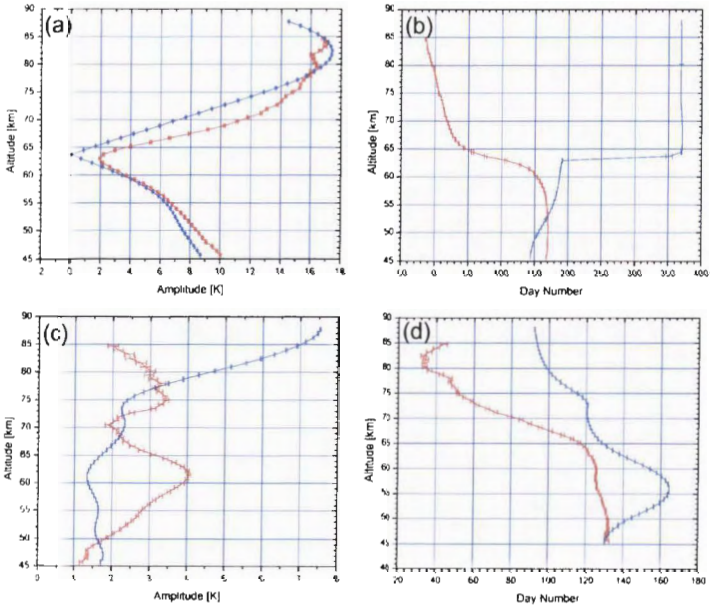


Figure 18. The annual and semi-annual amplitudes and phases for the ALO and MSIS composite years. The red curves correspond to results from ALO and the blue curves to MSIS. The annual amplitude is shown in (a) with the phase given in (b). Likewise for the semi-annual oscillation the amplitude is shown in (c) and the phase in (d). The associated error bars are the uncertainties from the fitting routine.

climatology leading the model by 38 days, day numbers 149 and 187, respectively. The phase inversion in the model is abrupt, occurring between 63 and 64 km, shifting to later in the year at higher altitudes, with a constant phase above 65 km at about 3 January. Unlike MSIS–00, ALO has a less abrupt phase transition that moves to earlier in the year

at higher altitudes with the largest change occurring between 60 and 65 km followed by a gradual change from mid-February at 65 km to mid-December at 85 km.

The amplitude of the semi-annual oscillation is smaller than that of the annual, as seen in Figure 18(c). The exception is near the altitude of the phase inversion in the annual cycle where the ALO semi-annual amplitude has a maximum. MSIS–00 has no corresponding relative maximum at this altitude. However, it does have a large maximum at 85 km that is not in the ALO observations. The phase shows good agreement at 45 km in both MSIS–00 and ALO, day numbers 130 and 132, respectively. At higher altitudes, ALO leads MSIS–00. By 55 km, the MSIS–00 phase has significantly increased to day number 165 while the ALO phase has decreased to day number 127. The increasing amplitude of the semi-annual amplitude and the large phase difference, 75 degrees, accounts for much of the temperature differences seen between MSIS–00 and the temperature climatology between 55 and 60 km, as shown in Figure 17 (a and b). The phase differences decrease near 63 km where the annual term has a phase inversion, and then increases at higher altitudes. The largest phase differences are found in the upper mesosphere near 75 km where ALO leads the model by as much as 64 days or 128 degrees.

The 31-day average of the ALO database does not average out the higher order harmonics in the ALO climatology, Figure 19. The largest of these is the 4 month oscillation that has a maximum of 2.7 K near 67 km slightly above the minimum in the annual cycle. The 3-month and 2.4-month oscillation in comparison have amplitude maxima at ~ 63 km where the annual cycle has its minimum. The amplitudes are also similar with values of 1.4 and 1.2 K respectively. Above 80 km, data sampling may be

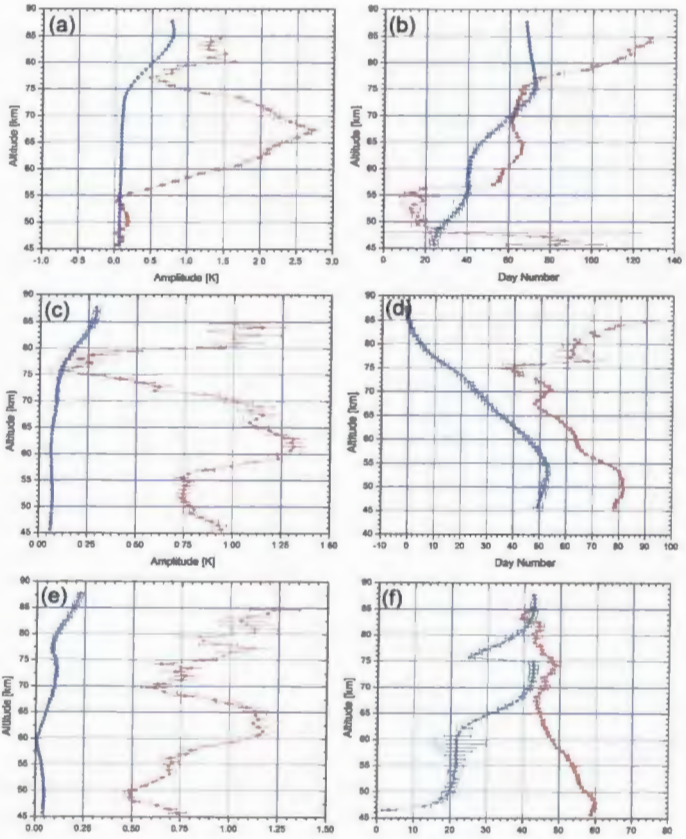


Figure 19. The 4-month, 3-month, and 2.4-month oscillations in the composite years. The red curves indicate the ALO climatology and blue indicate the MSIS–00 model. The amplitudes are given on the left with the phase on the right. The 4-month amplitude and phase are given in plots (a-b), 3-month in (c-d), and the 2.4-month cycle in (e-f). The associated error bars are the uncertainties generated from the fitting routine.

contributing to the increased amplitudes of the shorter periods. The fits to higher order harmonics of the annual oscillation have amplitudes that are less than 1 K for MSIS–00 This occurs because these harmonics were never included in the model parameterization. The 3-month and 2.4-month oscillations in particular have amplitudes that are typically less than 0.2 K in the mesosphere.

5. Discussion and Conclusions

Temperature profiles from the recently updated MSIS–00 empirical global model were compared to the mid-latitude, mesospheric temperature climatology from the ALO Rayleigh-scatter lidar. This is a significant "reality" check for the model because the ALO temperatures are completely independent of those used in the model. Moreover, for this part of the atmosphere, only limited data were available for inclusion in the model. The climatology is presented as a composite year made up of nighttime observations spanning a period of 11 years, as shown in Figure 14(b). Each data point in a profile represents a 3-km average in altitude. Each day (night) in this year contains an average of all the temperatures within a 31-day window centered on that day. To make this comparison, model temperatures were generated for each hour of each night included in the lidar climatology and were then averaged together in the same way as in the climatology. In addition to these two composite years, the 31-day temperature profiles were averaged together to produce two annual profiles.

The annual profiles, while similar, show systematic differences as large as 5 K. Statistically, these are significant. In the climatology, the error or standard deviation of the mean for the temperatures in a 31-day window is less than 1 K below 80 km. For a

year, it is less than 0.3 K. The temperature differences between the two composite years are more pronounced and are very structured with large regions where MSIS–00 is warmer or colder than the ALO climatology.

The largest temperature differences are found in the upper mesosphere, especially near the summer mesopause. In general, the model becomes increasingly cooler than the climatology above 78 km. While the mesopause is usually above the range of the ALO lidar, during the period near summer solstice, it becomes visible at ~84 km. In contrast, the minimum mesopause altitude in the model is ~87 km, an altitude more appropriate for polar latitudes. This model mesopause is 11 K cooler than the climatological mesopause minimum. However, the climatological minimum occurs ~20 days prior to the summer solstice. As such, during the solstice, the model is ~17 K cooler than the climatology by 84 km.

If the derivation of the lidar temperatures were initialized using MSIS–00 temperatures instead of the independent CSU sodium lidar temperatures, these differences would be greatly reduced. Clearly, that would be the case at the highest lidar altitudes. 85 km is close enough to the initialization altitude on many nights in the 31-day averages that the difference between the lidar and model temperatures remains very small. However, by 75 km that situation has changed. The two sets of initial values produce differences in the lidar profile that are less than 1 K. At this point, the lidar temperatures are independent of the initial values used in their derivation.

Thus, much of this large difference at 85 km can be traced back to the CSU climatology used to initialize the ALO temperature derivation. Nonetheless, these inferred warmer temperatures near the mid-latitude, summer mesopause are consistent

with other observations which describe the MSIS temperatures as cold [*Leblanc et al.*, 1998; *Leblanc et al.*, 1999; *Liu and Meriwether*, 2004]. The cold model temperatures appeared in the CIRA–86 km model and were carried forward into the MSIS–90 and MSIS–00 models. The mid-latitude mesopause temperatures in the model are also highly dependent on early resonance lidar temperatures [*Lübken and von Zahn*, 1991], although those observations were made at polar latitudes [*Hedin*, 1996].

Below 75 km a big qualitative difference is the stratopause. The maximum stratopause temperatures from the climatology and the model differ by 1 K, 274 and 273 K, respectively. The largest differences were found during the winter periods when the minimum stratopause temperatures differ by 7 K, at 249 K and 256 K, respectively. These differences are large enough to cause the model to be on average warmer than the climatology near the stratopause. In addition to the overall temperature differences there are also differences in the stratopause altitudes. During the composite year, the stratopause altitudes from the model are clearly between 45 and 48 km. However, in the climatology the stratopause is above 45 km for only part of the year.

Both the ALO climatology and the MSIS–00 model show strong annual cycles. Below 60 km, the phase of the annual cycle follows that of the solar flux. Above 65 km, the annual cycle is out of phase with the solar flux. The amplitude of the annual cycle in the model in both these regions, the upper mesosphere and near the stratopause, is smaller in the model than in the ALO climatology. In going to higher altitudes, above the 63-km transition region, the phase of the annual cycle shifts towards the first of the year in the ALO climatology. In contrast, in the model, it shifts towards the end of the year. Moreover, the model transition is much more abrupt. These differences in the phase

transitions appear to be related to the presence of mesospheric inversion layers (MILs) that are characteristic of winter observations at ALO [e.g., *Meriwether et al.*, 1998; *Nelson and Wickwar*, 2007] and are routinely observed at mid-latitudes [*Hauchecorne et al.*, 1987; *Leblanc et al.*, 1995; *Whiteway et al.*, 1995; *Meriwether and Gerrard*, 2004]. When MSIS was extended from the thermosphere into the lower atmosphere, the geographical and temporal distributions of the mesospheric inversion layers were not well known and as a result were excluded from MSIS–90 [*Hedin*, 1996] and subsequently MSIS–00. While changes to the parameterization of the MSIS database have created a slight signature of MILs in MSIS–00 [*Picone et al.*, 2002], to be properly included, new data with better altitude resolution needs to be included in future model revision.

The observed semi-annual cycle is almost everywhere stronger than in the model below 80 km. In particular the observed semi-annual oscillation has a maximum at 63 km where the annual cycle has its minimum. This behavior is also present in the French mid-latitude lidar climatology [*Leblanc et al.*, 1998]. However, it is not seen in MSIS–00. Above 80 km, the model's semi-annual amplitude increases dramatically to values well above the observations. This difference may arise from the over influence of high-latitude data on mid-latitude model values discussed above. It might also arise from the new interpolation across the region between the rocket and radar observations.

At certain altitudes the higher frequency (shorter period) oscillations, 4 month and shorter, make a small but statistically significant contribution to the temperature structure of the ALO climatology. However, they make almost no contribution to MSIS–00 temperatures because they were not included in the model's parameterization [*Hedin*, 1991]. Finding these oscillations to be significant supports a similar result found at

higher latitudes from a much smaller database [*Gardner et al.*, 2005]. Now the question becomes finding the origin of these short period oscillations.

To some extent the magnitude of these temperature differences are not terribly large, but they are large enough to impact inferences about the physical and chemical processes in this region. Discrepancies in upper mesospheric temperatures could affect, for instance, what could be learned about the meridional summer-to-winter flow, chemical heating, and radiative cooling. Differences in stratopause height could affect inferences about heating and cooling rates. The greater ALO height suggests larger stratospheric heating or smaller mesospheric cooling rates. That this difference persists for the whole year might suggest greater solar input. The inferred role of MILs is more significant in the ALO data than in the empirical model. This greater role shows up in the different winter temperatures, the different phase progression of the annual component in the high-to-low-altitude transition, and the differences in the semi-annual amplitudes and phases. This, in turn, puts more emphasis on trying to understand the life cycle of MILs.

This type of comparison or validation of an empirical model by independent observations is very important. The MSIS–00 rendering of the mid-latitude mesosphere could be significantly improved in the next revision by including more data from this region. For most of the mesosphere, data could be provided by Rayleigh-scatter lidars. Above 80 km, some could be provided by resonance scatter lidars. It may take data from a much more sensitive Rayleigh-scatter lidar and a combination of Rayleigh and resonance lidars, both of which are being implemented at ALO, to provide continuous altitude coverage through the transition region represented by the mesopause. In

addition, new measurements are necessary to keep the model in step with the possible effects of climate change.

CHAPTER 5

OBSRVATIONS OF A NOCTILUCENT CLOUD ABOVE LOGAN UTAH (41.7° N, 111.8° W) IN 1995[3]

Abstract

A Rayleigh-scatter lidar has been operated at the Atmospheric Lidar Observatory (ALO) on the Utah State University (USU) campus (41.7° N, 111.8° W) since August 1993. During the morning of 22 June 1995, lidar returns from a noctilucent cloud (NLC) were observed for approximately one hour, well away from the twilight periods when NLCs are visible. This detection of an NLC at this latitude shows that the first reported sighting, in 1999 [*Wickwar et al.*, 2002], was not a unique occurrence. This 1995 observation differs from the 1999 one in that temperatures could be deduced. Near the 83-km NLC altitude the temperatures were found to be up to ~23 K cooler than the 11-year June climatology for ALO. This analysis shows that these cool temperatures arose, not because the whole profile was cooler, but because of a major temperature oscillation or wave with a 22 km vertical wavelength and a ~0.9 km/hr downward phase speed. This large-amplitude wave has many of the characteristics of the diurnal tide. However, the amplitude would have to be enhanced considerably. These lidar observations were supplemented by OH rotational temperature observations from approximately 87 km. These NLC observations equatorward of 50° have been suggested to be significant harbingers of global change. However, if that were the case, the mechanism is more complicated than a simple overall cooling or an increase in water vapor. Accordingly, we propose enhanced generation of gravity waves that would interact with the diurnal tide to

[3] Coauthored by Joshua Herron, Vincent B. Wickwar, Pat Espy, and Jonathan Meriwether.

produce a large-amplitude wave, the cold phase of which would give rise to low enough temperatures to produce the NLC. The gravity wave source might be orographic in the Mountain West or convective far to the east or south.

1. Introduction

Noctilucent clouds (NLCs) typically occur during the summer months between 80 and 86 km in the polar regions or, more specifically, at latitudes greater than 50° [*Gadsden and Schroder*, 1989; *Thomas and Olivero*, 1989; *Chu et al.*, 2003]. They most likely consist of ice particles [*von Cossart et al.*, 1999; *Hervig et al.*, 2001]. NLC observations are important as they may serve as tracers of global change [*Thomas*, 2003]. Lidar observations of NLCs provide information about their altitude, thickness, and magnitude, and about the variability of these parameters. The first reported lidar observation of an NLC below 50° was by the ALO lidar group in 1999 [*Wickwar et al.*, 2002]. Because of the possibility that other NLCs might have been observed, but not previously identified; the entire ALO database was searched. A second event was found on 22 June 1995, four years earlier than the first reported event.

The lidar and a Michelson Interferometer (Fourier transform spectrometer) are described in Section 2 along with their basic data reduction. The 1995 lidar observations, the special data analysis procedures, and their results are given in Section 3. The NLC results are discussed in Section 4, and the conclusions from the observations and discussion are presented in Section 5.

1. Instrument Descriptions and Data Reduction

The Rayleigh-scatter lidar at ALO is located in Logan, UT (41.7° N, 111.8° W) on

the Utah State University (USU) campus, 1.46 km above sea level. It has been operated as much as possible since August 1993, giving rise to an extensive database of nighttime mesospheric profiles of relative densities and absolute temperatures.

The lidar is a coaxial system that had a power-aperture product of 3.3 Wm^2 in 1995. The system is composed of a Spectra Physics Nd:YAG laser operating at 30 Hz generating 20–22 watts at 532 nm and having a 44-cm diameter Newtonian telescope. The signals from below ~18 km are blocked by a mechanical chopper and the gain is reduced by almost 1000 by an electronic gate for altitudes below 38 km, leading to good data above 41 km. A narrow-band interference filter (1 nm) is used to remove most of the background light from stars, moon, and scattered city lights. The single, gated detector is a green-sensitive, bialkali photomultiplier tube (Electron Tubes 9954B) in a Peltier-cooled housing. A more extensive description of this system is given in *Wickwar et al.* [2001] and *Herron* [2004].

The observations were made in the zenith with an altitude resolution of 37.5 m (250-ns sampling interval) and a temporal resolution of 2 minutes (3600 laser pulses). In the usual data reduction, the data are averaged over 3 km and 1 hour prior to determining relative densities and temperatures. When the signal from the background light and thermionic emission, determined near 130–180 km, is subtracted from the observed signal and the difference is multiplied by the square of the range, the result is usually proportional to the molecular number density. However, the exception, discussed in the next section, occurs when an NLC is present and added signal is generated by Mie scattering from ice crystals. Temperatures are determined from the relative number densities by using hydrostatic equilibrium and the ideal gas law. The details, as applied

to this lidar, are reviewed in *Herron* [2004] and Chapter 3. However, this data reduction procedure had to be modified to find temperatures in the presence of the NLC. This special analysis is described in the next section.

Temperature data were also available for June 1995 and June 1996 from a Michelson Interferometer that was located approximately 100 m from the lidar and also observing in the zenith. Temperatures were derived at roughly 10-minute intervals from the rotational structure of the OH(3,1) Meinel band [*Espy and Stegman*, 2002]. They apply to approximately 87 km, the altitude of the centroid of the OH airglow emission layer [*von Zahn et al.*, 1987; *Baker and Stair*, 1988; *She and Lowe*, 1998], although WINDII observations frequently show the layer peak anywhere between 85 and 90 km [*Liu and Shepherd*, 2006]. The precision of the individual temperature determinations is, on average, 3%, and a minimum of ten measurements are used to determine a nightly average. Unfortunately, because of uncertainties in the OH transition probabilities [e.g., *Burns et al.*, 2003], the OH rotational temperatures cannot be compared directly to the kinetic temperatures from the lidar. However, temporal variations in the OH temperatures are reliable.

3. Observations and Data Analysis

During the early morning hours of 22 June 1995 the lidar was operated from 6:30 UT (00:30 Mountain Daylight Time, MDT) until 10:56 UT (04:56 MDT). An enhancement in the photocount profile above what was expected from Rayleigh scatter alone was observed in 2-minute profiles between 8:03 and 8:54 UT (from the beginning of the first 2-minute observation to the end of the last 2-minute observation) and more

weakly between 9:39 and 9:48 UT. It is presumed that these enhancements arose from Mie scatter from an NLC. These time periods with the Mie scatter correspond to solar depression angles between 17.3° and 24.3° for which the shadow heights are between ~300 and ~600 km, well above the observed Mie scatter enhancements. Accordingly, the NLC, at altitudes below 85 km, was in the Earth's shadow and could not have been observed visually from the ground. Nonetheless, we still take the liberty of calling it an "NLC."

The lidar raw photocount profiles typically include contributions from background light and photomultiplier-tube dark count as well as from Rayleigh backscatter, which is proportional to atmospheric number density. When an NLC is present, there is an additional contribution from Mie scatter from the large particles that make up the NLC, which is seen as an enhancement in the photocount profile. When the background light and dark counts are subtracted from this profile and the values are multiplied by range squared, this becomes the relative density profile, which is shown in Figure 20a. The signal from the peak of the NLC layer is equivalent to the Rayleigh-scatter density at an altitude of ~70 km.

The backscatter ratio $R(z)$ is commonly used as a measure of the NLC strength. It is the ratio of the measured signal $S(z)$, as contributed to Figure 20(a), to the Rayleigh-backscattered signal $S_R(z)$:

$$R(z) = \frac{S(z)}{S_R(z)} = \frac{S_R(z) + S_m(z)}{S_R(z)} \qquad 5.3.1$$

where $S_m(z)$ is the Mie-backscattered signal. To reduce the variability, the photocount profiles were smoothed by making running averages in both altitude and time. To

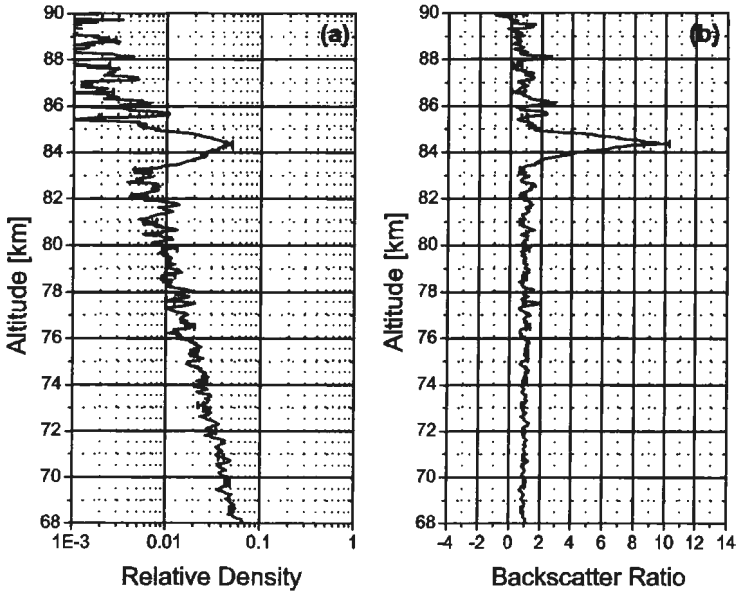


Figure 20. The NLC enhancement on 22 June 1995 at ALO seen in the profiles of relative density (a) and the backscatter ratio (b). The data were averaged over 12 minutes, centered on 8:13 UT, and over 150 m. However, data points are plotted every 37.5 m. The uncertainties are based on the measurements, assuming Poisson statistics.

minimize distorting the NLC parameters, the averaging was carried out over only 4 points in altitude (150 m) and 6 points in time (12 minutes). However, the profile for the Rayleigh-scattered signal S_R used to calculate the backscatter ratio R in Equation 1 was found by averaging all the periods without evidence of the NLC during the night of 22 June. To further minimize the possibility of contamination by Mie scatter, a 3rd order

polynomial was fitted to the average photocount profile, S_R, at 37.5-m intervals from 79 to 82 km and from 85 to 88 km, excluding the region of the NLC. The polynomial was then used to replace the observations between 82 and 85 km. A smoothing function over 41 points, 1.5 km, was then applied to minimize the fluctuations in this Rayleigh profile.

These 12-minute profiles of the backscatter ratio were derived every 2 minutes. From them it was determined that the maximum backscatter ratio for the NLC was 9.6 and it was centered on 8:13 UT. The corresponding profile is shown in Figure 20(b). These profiles also were used to create a contour plot of the backscatter ratios, Figure 21. This shows the main body of the NLC between 7:54 and 8:58 UT (from the beginning of the first 12-minute observation to the end of the last 12-minute observation), and an additional small enhancement in the backscatter ratio between 9:31 and 9:54 UT at ~83.1 km. During the period that the main body of the NLC had a BSR of 2 or more, the NLC descended very slowly from 84.4 to 84.3 km, fairly rapidly to 83.4 km, and then slowly to 83.2 km. Between 8:01 and 8:16 UT, a least-squares fit gives a rate of −0.08 m/s, between 8:18 and 8:32 UT a rate of −3.3 m/s, and between 8:34 and 8:51 UT, a rate of −0.9 m/s. While several small regions with a BSR of 2 exist and are shown in Figure 21, the largest of them is at this lowest altitude, 83.2 km. Because of its greater extent in altitude and time, this was identified as a small NLC enhancement. The other regions are considered to be noise fluctuations.

At the height of the NLC, the diameter of the laser beam is ~40 m, which means that only a very small portion of the cloud is sampled at any instant. Furthermore, the beam is fixed in the zenith direction preventing any knowledge of the horizontal extent or

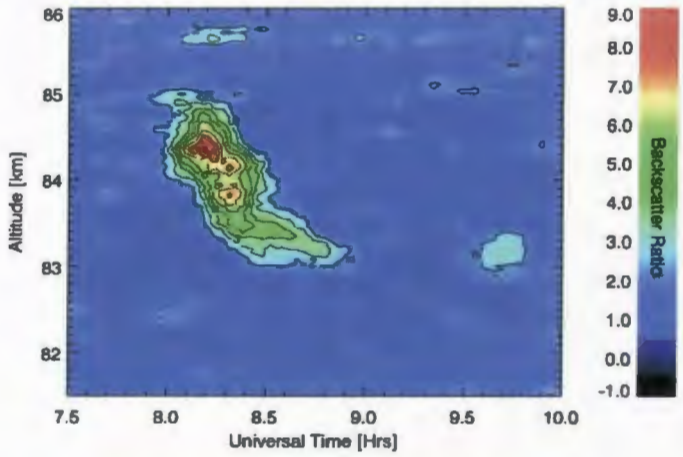


Figure 21. Backscatter ratios for the 22 June 1995 NLC. The inputs for the contour plot were created every 2 minutes using a 2-D running average with a width of 12 minutes and a height of 150 m applied to the raw data, which were measured every 2 minutes and every 37.5 m. A backscatter ratio of 1 indicates that there is no Mie-scatter enhancement. The time is in hours.

structure of the cloud. Accordingly, it is not possible to distinguish between a layer descending in the beam, a slanted layer being transported horizontally across the beam, or a combination of the two. Accordingly, the deduced descent rates are really apparent descent rates.

To compare these NLC observations to those made in 1999 [*Wickwar et al.*, 2002], the results from the 1999 NLC were re-analyzed using the same temporal and spatial averaging as for the 1995 NLC, Figure 22. The 1995 NLC maximum backscatter ratio occurs at a higher altitude, 84.4 versus 82.1 km, and has a greater maximum backscatter ratio. It was 9.6, 90% greater than the maximum of 5.1 reached by the 1999

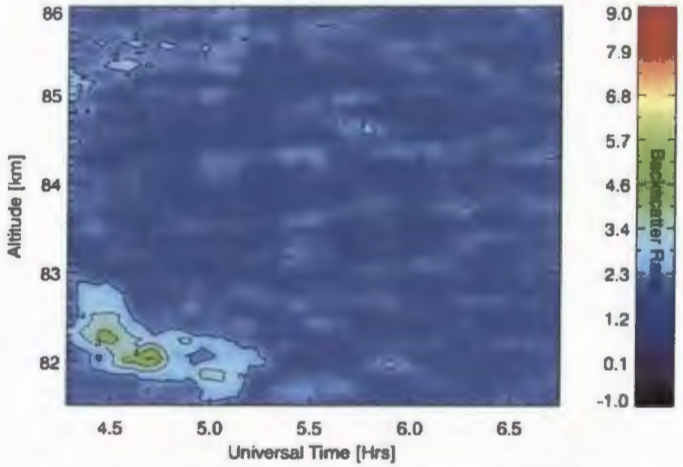


Figure 22. Backscatter ratios for the 1999 NLC [*Wickwar et al.*, 2002] analyzed and presented in the same way as for the 1995 NLC in Figure 21. It is at a lower altitude and the maximum backscatter ratio is smaller.

NLC. This does not mean that the 1995 NLC backscattered 90% more light. Part of this greater backscatter ratio occurs because the Rayleigh contribution to the backscatter ratio (the denominator in Equation 5.3.1) is smaller at the higher altitude. By using the observed relative density profile, the backscatter ratio of 9.6 at 84.4 km translates to 6.7 at 82.1 km, only 31% greater than that of the 1999 observation, assuming the same neutral densities at 82.1 km on both occasions. Thus, the biggest difference between the two NLCs is that the one in 1995 was 2.3 km higher.

In addition to these results concerning the NLC altitude, another significant difference occurred between the 1995 and 1999 observations. In 1995, the background signal was well behaved, which is extremely important for deriving temperatures,

especially at the highest altitudes (Chapter 3). And, the laser had more power, which is essential for deriving temperatures above the NLC altitude. This possibility of obtaining temperatures in 1995 provides an important additional dimension to the NLC observations.

To determine density and temperature profiles, the individual two-minute profiles are averaged together during three periods. The first period (06:30–08:00 UT) extends from the start of observations for the night to just prior to the start of the NLC observations; the second (08:00–09:00 UT) encompasses the period when the NLC was observed and extends a little on either end; and the third (09:00–10:56 UT) spans the time from just after the NLC to shortly before dawn.

The first period has no discernable NLC enhancement and was used to examine fitting routines for interpolating across the NLC. Several low-order polynomials were fitted over the same region used in calculating the backscatter ratio, but with independent points every 37.5 m. A 3rd order polynomial fitted to the density profiles, excluding the 82- to 85-km region of the NLC, produced a reasonable fit and higher orders did not significantly improve the χ^2 values. Similarly derived fits were used to interpolate across the NLC region for all three time periods to remove any effects from Mie scatter.

These curves were then smoothed in altitude with a running average over 81 points (3 km). The first two relative density profiles are shown in Figures 23(a) and (b). The wide black curves are the observed relative density. The narrow red curves are the combination of the observations and the fits. In Part (a) the red and black curves are

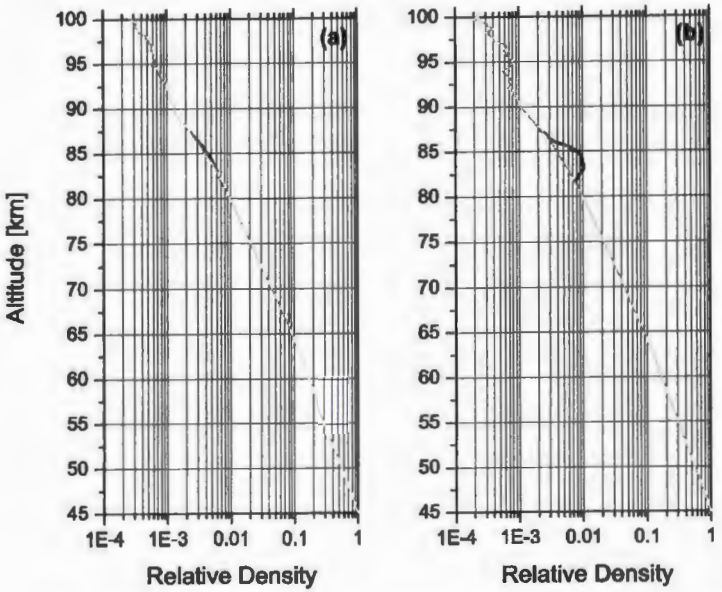


Figure 23. Relative density profiles before (4a) and during the NLC (4b). The thick black curves are the measured number density profiles; the thin red curves are the result of a 3rd order polynomial fitted to data in 3-km regions immediately above and below the NLC and then applied across the 3-km region in between. A 3-km running average was applied to both the measured number density profile and the profile with the polynomial fit. See the text for details about the fitting procedure.

almost indistinguishable, whereas in Part (b) the red curve smoothly bridges the region under the black NLC curve. (Because of the 3-km smoothing, the altitude gap bridged by the fit appears to be greater than the actual 3-km gap.) The fitted profiles are then used to calculate the corresponding temperature profiles, which are shown in Figure 24.

To our knowledge, this is the first time Rayleigh-scatter temperatures have been derived in the presence of an NLC. However, steps in this direction have been taken by

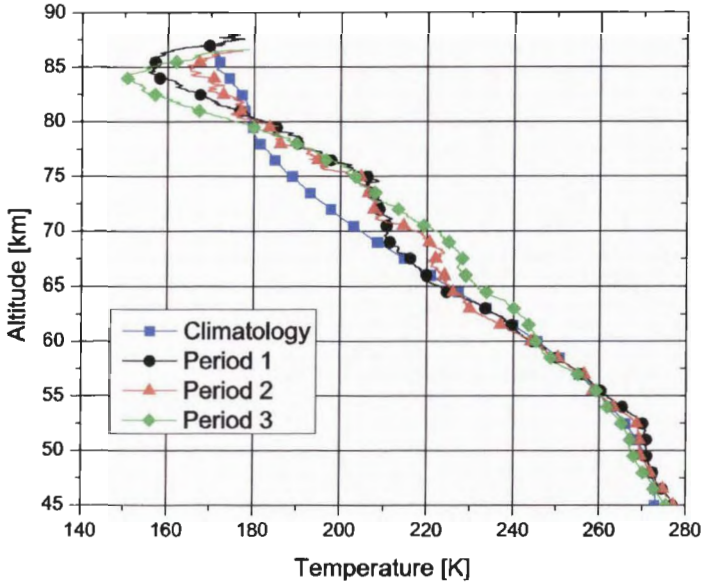


Figure 24. Temperature profiles before, during, and after the NLC on 22 June 1995. Period 1 is for 6:30-8:00 UT, period 2 for 8:00-9:00 UT, and period 3 for 9:00-10:56. The fourth profile is the average June temperature from the ALO climatology (Chapter 3). The corresponding density profiles for periods 1 and 2, from which the temperatures were derived, are shown in Figure 22.

others. *Collins et al.* [2003] interpolated across the NLC layer to calculate the backscatter ratio, but only calculated temperatures below the NLC layer. *Lübken et al.* [1996] interpolated lidar measurements across the NLC region to find the molecular signal for calculating the backscatter ratio when additional density measurements were not available from falling spheres. *Stebel et al.* [2004] interpolated across a possible wintertime aerosol layer at lower altitudes to calculate Rayleigh temperatures.

To derive absolute temperatures from the relative density profiles, a "best guess" temperature is needed at the highest altitude. The highest altitude, in this analysis, is determined to be the point where the signal has dropped to 20 times its one standard-deviation uncertainty. The "best guess" value was taken from the temperature climatology from the Colorado State University (CSU) sodium lidar [*She et al.*, 2000]. While this is a climatological value, it is still the best source available for a particular night. The temperature profiles for the three periods are shown in Figure 24 along with the 11-year, June climatological average for ALO (Chapter 3). The temperature uncertainties are from a full error propagation starting from the observed photocounts [*Gardner*, 1989; *Herron*, 2004], assuming Poisson statistics. The total variability, measurement plus geophysical, for an individual night in the 11-year average is not shown, but is fount to be, for example, 12 K at 84 km, 8.4 K at 71.5 km, and 3.7 K at 60 km. It is derived using the 103 nighttime June temperatures and their mean to calculate the standard deviation (Chapter 3). The total variability for the mean is 10% of those values.

The minimum temperatures for the three 22 June profiles are found near 84 km and are considerably colder than for the June climatological average. The differences between these temperature profiles and the climatological averages are presented in Figure 25. The first and third profiles reached minimum values between 150 and 160 K in this region and became 17–23 K cooler than the average. The second period was slightly warmer. In contrast, centered on 73 km, all three temperature profiles became significantly warmer by ~17 K than the climatological average. The negative and positive departures from the June average clearly have the appearance of a large vertical

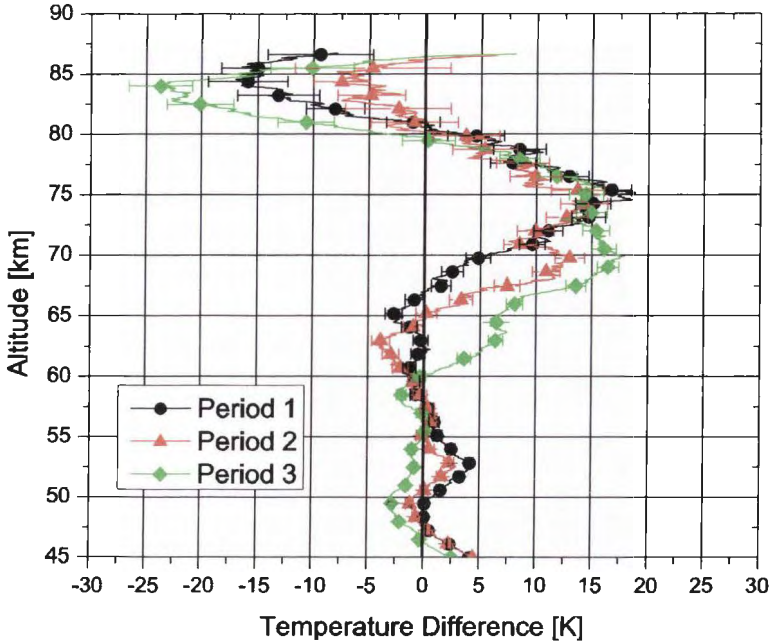


Figure 25. Temperature differences between the observed values on 22 June 1995 and the climatological June average for ALO. The temperature profiles are from Figure 5.

temperature oscillation or wave.

The properties of this wave were examined directly by overlaying profiles and by both autocorrelation and cross correlation of the profiles. The altitudes of the temperature minima occur between 85 and 83 km and of the maxima between 74 and 72 km. The best value for the vertical wavelength is ~22 km. The deduced phase velocity is highly variable. The average value for the three profiles varies from −0.6 to −0.8 km/hr depending on how it is derived. Overlaying small portions of one temperature profile

over another gives the best results. The minimum near 84 km has a relatively constant phase velocity of −0.6 km/hr and the maximum near 73 km has phase velocities that vary from −1.8 km/hr between periods 1 and 2 to −0.3 km/hr between periods 2 and 3, with a value of −0.9 km/hr between periods 1 and 3, which encompasses the NLC. The uncertainties are less than 0.2 km/hr. Part of these changes in the apparent phase velocity probably occurs because the shape of the maximum is changing with time. It is becoming thicker.

To provide context for the NLC observations, additional temperature measurements would be desirable. Unfortunately, very few good lidar observations exist in June 1995 and 1996. In 1995, the observations preceding the 22nd were plagued by cloud cover. On the following two nights the lidar was operated for a minimum of six hours providing reasonable temperature profiles. The all-night temperature profile from the 23rd is similar to the three profiles from the 22nd with a wave and a temperature minimum between 150 and 160 K. On the 24th, the temperature minimum is at 81 km, however it has no discernable positive departure from the June average near 73 km. The lidar was not operated in June 1996.

However, as discussed in the previous section, a Michelson Interferometer was operated at USU during June 1995 and 1996. Temperatures from these observations, nominally from 87 km [*Baker and Stair*, 1988], are shown in Figure 26. It is apparent that the all-night temperatures from 19 to 24 June 1995 are particularly cool and that the temperature for 22 June 1995 is significantly cooler than for all the other nights. In addition, the June 1995 nights are systematically cooler than the June 1996 nights by an average of 16 K. While this is a large amount, it is plausible when compared to the

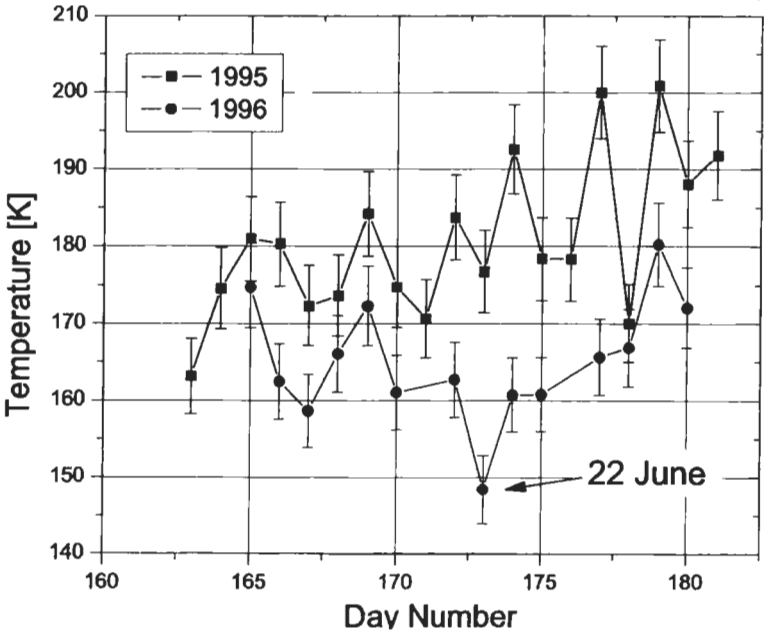


Figure 26. Nighttime OH rotational temperatures at ~87 km from the Michelson Interferometer located at USU. The red curve denotes the values from 1995; the blue curve denotes those from 1996. The NLC night is identified.

observed standard deviations for June in the ALO climatology (Chapter 3). That standard deviation contains the combined effects of day-to-day variability, interannual variability, and long-term trends. At 84 km, the highest altitude for which it was tabulated, the standard deviation is 12 K. That value is an underestimate because 84 km is close to the altitudes for which the initial values were found. A better estimate of the standard deviation can be found by extrapolating the values found at lower altitudes, far removed from the initial values. A linear extrapolation of the standard deviations

from 66 to 75 km gives a value of 14 K at 84 km and 16 K at 87 km. That the 13 nights in 1996 are all warmer than the corresponding nights in 1995 suggests that this difference arises from an interannual variation. Whether considering the 1995 data alone or in combination with the 1996 data, it is apparent that 22 June 1995 is an unusually cold night at 87 km.

Temperatures from the Michelson Interferometer are also available at sub-hour intervals, as shown for 22 June 1995 in Figure 27. The temperatures dropped quickly after 05:00 UT to a minimum at 06:11 UT and then returned to a level less than the initial one. Compared to this later level, the minimum temperature was ~30 K less. This variation suggests a wave in time with high temperatures initially, followed by low temperatures, which would be consistent with the descent of the type wave seen in the lidar profiles. The amplitude of the cold portion of the wave is greater than deduced for the lidar data. Ignoring holes in the data, the lowest temperatures were observed 1.07 hours before the first lidar temperature profile with its lowest temperature at 84.5 km and 1.84 hours before the appearance of the NLC in the lidar data at 84.4 km.

This large oscillation in time in the OH temperatures is at a slightly higher altitude and prior to the lidar observations of the vertical temperature wave and of the NLC observations. If these are two manifestations of the same wave, then the combined temperature observations indicate that it descends at a rate of 2.3 km/hr assuming the centroid of the OH emission is at 87 km or 1.4 km/hr if it is at 86 km. The time to the appearance of the NLC would indicate a descent rate of 1.4 km/hr for the OH originating from 87 km or 0.9 km/hr for it originating from 86 km.

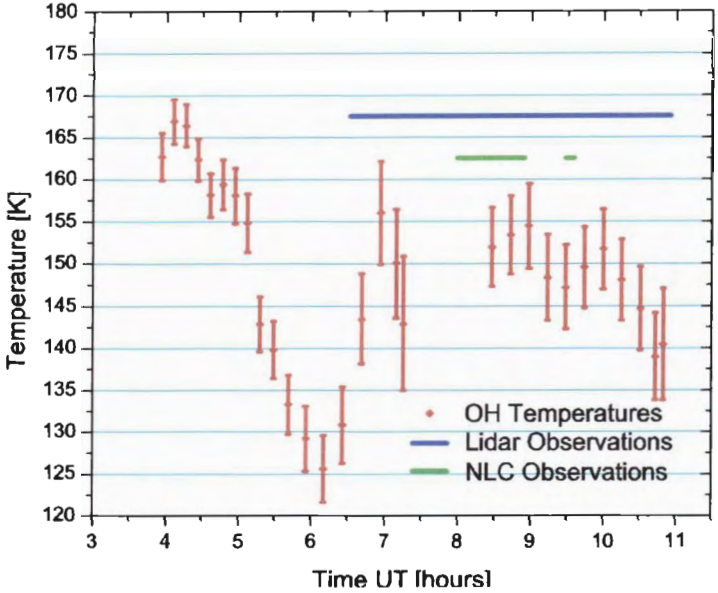


Figure 27. OH rotational temperatures at ~87 km for the night of 22 June 1995. In addition, the time period when the lidar was operated is indicated in black and when the NLC was observed is indicated in grey.

4. Discussion

4.1. NLC Characteristics

The magnitudes of both the 1995 and 1999 NLCs detected at ALO at 41.7°N are weak compared to those observed at higher latitudes where the backscatter ratio can be greater than 200 [e.g., *Hansen et al.*, 1989; *Langer et al.*, 1995; *Thayer et al.*, 1995; *Fiedler et al.*, 2003]. When adjusted for altitude, the 1995 NLC was about 30% stronger than the 1999 one.

A strong linear trend in NLC altitude versus latitude has been found for NLC events [*von Zahn and Berger*, 2003; *Chu et al.*, 2004]. The 1999 NLC shows a mean altitude of 82.1 km, which is in very good agreement with that linear trend. However, the mean altitude of the 1995 NLC observation was 83.8 km, 1.7 km higher and significantly above the linear trend. Whether this indicates different origins for the two NLCs is more than can be determined from the available data. However, what is clear from the lidar temperatures is that the 1995 NLC is unusual in that it occurs at the minimum of a large-amplitude vertical temperature wave. The main portion of NLC occurred between 7:54 and 8:58 UT. During that time it descended from 84.4 to 83.2 km, with its average height at 83.8 km. The minimum in the temperature profile integrated over this period is at 84.0 km.

This wave is the dominant feature in Figure 25. It shows a persistent, large, temperature oscillation or wave with a maximum amplitude of 23 K for the cold phase at 84 km and a maximum amplitude of 17 K for the hot phase at 73 km. The lowest temperature from these three profiles is ~150 K. From the minima and maxima in this wave, the inferred vertical wavelength is 22 km. In addition to the lidar data, a time series of OH temperatures from a Michelson Interferometer from ~87 km shows a large oscillation in time with a temperature minimum ~30 K below the subsequent temperatures at ~125 K. The temperature minimum occurs a little more than an hour prior to the beginning of the lidar observations and a little less than two hours prior to the NLC detection. Combining the Michelson and lidar observations, assuming the OH emission is centered at 87 km, leads to descent rates of −2.3 and −1.4 km/hr for these two intervals. However, if the OH emission were centered at 86 km, well within the range of

uncertainty and variability, the descent rates become −1.4 and −0.9 km/hr. The lidar results for these three integrations show a nearly constant descent rate of −0.6 km/hr for the temperature minima near 84 km between 06:30 and 10:56 UT (start and end times for the lidar data). In contrast, the temperature maxima, from ~11 km lower, show a rate that decreases with time from −1.7 km/hr between periods 1 and 2 to −0.3 km/hr between periods 2 and 3. Between periods 1 and 3, it has the average value of −0.9 km/hr. While the descent rate deduced from the minima is much slower than the two inferred values from the OH observations, the rate from the earliest two lidar periods for the maxima is consistent with the OH observations. Furthermore, while the minima appear to have a constant descent rate, the maxima show a descent rate that is slowing with time, which is consistent with what is inferred from the OH observations. If the minima and maxima are descending at the same rate, the wavelength should be constant, whereas if they are descending at different rates, the wavelength should vary. However, the amount is less than the 1-km precision of the wavelength determinations. Combining these observations concerning the descent rates, it appears that the altitude and magnitude of the temperature minima may be influenced by being close to the initial temperature. Because the initial temperature is based on climatological values it is probably higher than it should be for this particular day. The impact of this is that the temperature minimum would be either at a lower altitude than it should be or would not extend over as large an altitude region as it otherwise would, and that the minimum would have a higher temperature than it should have. Two other implications are that the layer would not appear to move downward as quickly as it should and that as it did move downward the minimum temperature would decrease. The point of this discussion is that the descent speed of the

minimum may be closer to that of the maximum than what was actually measured. In that case, it would be very similar to the value of −0.9 km/hr inferred by combining the OH and lidar measurements. This supports the idea that these two instruments are detecting different manifestations of the same wave.

As for NLCs being associated with temperature minima of large vertical waves, this observation appears to be a first. Previously, large waves with amplitudes of 20 K, similar to this wave, have been reported at high latitudes at NLC altitudes by *von Zahn and Meyer* [1989], but not in conjunction with an NLC.

Temperatures at high latitudes, derived from falling spheres released from rockets, have shown that NLCs typically occur when the temperature is 150 K or lower [*Thomas*, 1991; *Lübken et al.*, 1996; *Lübken*, 1999]. While, the June temperature climatology for ALO gives a much higher temperature, ~173 K, on average at the NLC altitude of 84 km, the wave observations for 22 June 1995 show the temperature at 84 km reaching the immediate vicinity of 150 K. The Michelson Interferometer temperatures even reach the vicinity of 125 K at ~87 km.

Combining the two sets of temperature results and the NLC results, it appears that the wave caused the temperatures to drop low enough to start forming ice crystals at 87 km or so. The growing particles probably descended initially at the same rate as the wave. However, shortly after they become large enough to backscatter detectable radiation, they became massive enough for sedimentation to occur at a faster rate. For 15 minutes in the middle of the hour when the NLC was detected, it descended at an apparent rate of −3.3 km/hr. When the cloud reached 83.5 km at 8:30 UT, the backscatter ratio started to decrease significantly and the descent slowed to −0.9 km/hr. The peak

BSR was not seen below 83.2 km. Presumably, the ice crystals were sublimating on the bottom side of the NLC. And, given this scenario, it is most likely that the small, detached NLC observed between 9:31 and 9:54 UT at 83.2 km was transported into the lidar field of view.

4.2. Relationship Between the NLC and Climate Change

The appearance of NLCs at latitudes <50° N suggests a manifestation of global climate change [*Thomas*, 1996b, 1997, 2003]. These predictions follow from model calculations based on large increases in greenhouse gases and methane leading, respectively, to a cooling in the upper mesosphere and an increase in water vapor concentration that would increase the temperature at which water vapor freezes spontaneously. However, NLCs were observed at 41.7° N at ALO in June 1995 and 1999, much sooner than predicted for the large increases in these gases to have occurred. And indeed, it is a period when the ALO temperature climatology shown in Figure 8 does not show evidence of such significant cooling. Nor is there evidence of a strong increase in water vapor. Among the few observations of mesospheric water vapor, *Chandra et al.* [1997] and *Nedoluha et al.* [2003] show an inverse correlation with the variation of Lyman α during the solar cycle. This would give a small maximum in water vapor concentration in the summer of 1995, but not in 1999. If increased water vapor were the explanation in 1995, a different explanation would be needed for 1999. While possible, this seems unlikely. Trend information for water vapor is not particularly clear, but appears to be considerably less than the solar cycle effect. As for episodic events, the closest Shuttle launch, which might have injected water vapor into the mesosphere, was

almost 4 months prior to this noctilucent cloud detection, 2 March 1995. Thus it is unlikely that either mesospheric cooling or increased water vapor could account for this NLC.

It may be noteworthy that this second NLC found equatorward of 50° latitude was also found at ALO and not at one of the other Rayleigh-scatter or Na lidars operating at mid latitudes. This raises the question as to whether there could be a longitudinal effect associated with the Mountain West where ALO is located. Such an effect might arise from orographically generated gravity waves, non-migrating tides, or stationary planetary waves over this extremely mountainous region. This is consistent with a suggestion made to account for NLC formation at higher latitudes over the Rockies [*Espy et al.*, 1995].

Furthermore, this second NLC observation at ALO confirms that NLCs are occurring at lower latitudes than previously. If their occurrence is related to global change, as opposed to better observations, then the generation of the wave associated with the NLC observed in 1995 would have to be a manifestation of that change. The generation of the wave would, needless-to-say, have to be from a more complicated mechanism than uniform mesospheric cooling. As suggested above, a mechanism might involve the interaction of winds with the topography of the Mountain West to generate gravity and mountain waves or to contribute to non-migrating tides or stationary planetary waves. If it has to do with gravity waves, they might interact with the diurnal tide, as discussed next, to enhance the tidal amplitude. In either case, more or stronger tropospheric winds would be needed.

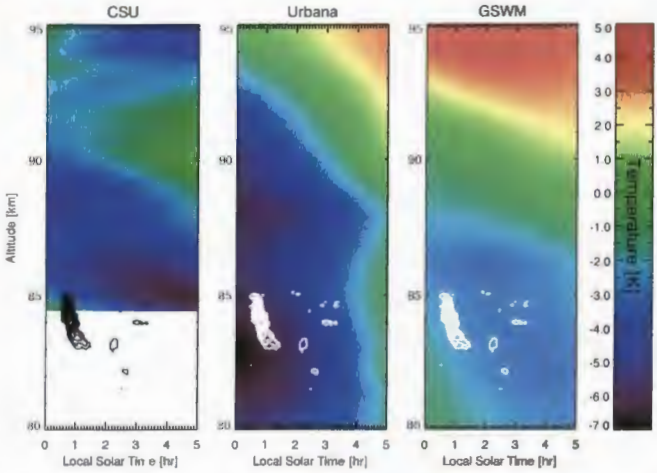


Figure 28. Amplitude and phase of the diurnal tide compared to the NLC. The tidal results were derived from the CSU sodium lidar measurements [*She et al.*, 2002], Urbana sodium lidar measurements [*States and Gardner*, 2000], and GSWM-00 model calculations [*Hagan et al.*, 1999; *Hagan et al.*, 2001]. Local solar midnight corresponds to 7:27 UT.

4.3 Comparison of Large Amplitude Waves and Tides

A potential seed for the observed wave might be an atmospheric tide. What is known about the diurnal and semidiurnal tides in this region can be compared to the observed NLC and the large-amplitude wave. Figure 28 shows contours of the June 1995 NLC (actually, all regions with a BSR $\geq$ 2) superimposed on the summer temperature structure from the diurnal tide derived from the mid-latitude sodium lidars at CSU (41°N) and Urbana (40.2°N) [*States and Gardner*, 2000a; *She et al.*, 2002] and the Global Scale Wave Model for 2000, GSWM-00, calculations for June at 42°N latitude [*Hagan et al.*, 1999; *Hagan et al.*, 2001]. Figure 29 is similar to Figure 28, but it shows contours of the

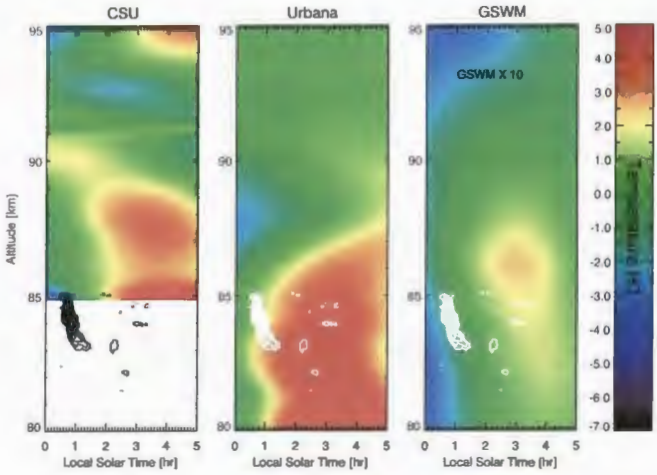


Figure 29. Amplitude and phase of the semi-diurnal tides in relation to the NLC occurrence. The tidal results are derived from the CSU sodium lidar measurements [She et al., 2002], Urbana sodium lidar measurements [States and Gardner, 2000], and GSWM-00 model calculations [*Hagan et al.*, 1999; *Hagan et al.*, 2001]. The model values had to be multiplied by 10 to use the same scale as the two sets of observations. Local solar midnight corresponds to 7:27 UT.

June 1995 NLC superimposed on the temperature structure from the semi-diurnal tide derived from observations at CSU and Urbana and calculated for GSWM-00. (The GSWM amplitudes have been multiplied by 10.) For the diurnal tide, the main body of the NLC is close in altitude and time to the temperature minima. For the semi-diurnal tide, the main body of the NLC is close to the zero amplitude point for GSWM and probably for CSU, but it is close to the temperature maximum for Urbana. These comparisons show the NLC and the ALO temperature minimum to be much more consistent with the phase of the diurnal tide than with the semidiurnal tide.

Additional comparisons can be made with other tidal parameters. Concentrating on the diurnal tide, vertical wavelengths can be compared. The vertical wavelength of the observed wave at ALO is ~22 km. For this to be related to a diurnal tide, the phase velocity would be −0.9 km/hr, which agrees well with the deduced phase velocity, showing great internal consistency. The diurnal component of the CSU temperatures [*She et al.*, 2002] gives a descent rate of ~−0.8 km/hr, which corresponds to a vertical wavelength of ~20 km. For GSWM it is ~−1.3 km/hr, giving a vertical wavelength of ~32 km. For Urbana it is also ~−1.3 km/hr above 88 km, but becoming indeterminate below that. Thus the ALO observations are in very close agreement to the CSU diurnal tidal observations. They are about 70% of the values found for GSWM and for Urbana.

Turning to the semi-diurnal tide, if the ALO descent rate of −0.9 km/hr is applied for 12 hours, it would give rise to a 12 km vertical wavelength instead of the observed 22 km. Thus, by themselves the ALO observations are not consistent with a semi-diurnal tide. Neither are the other observations and model calculation. Both CSU and GSWM show descent rates of ~−4 km/hr near 84 km, giving rise to a vertical wavelength of ~48 km. Urbana shows a much greater descent rate, which would give rise to an even longer vertical wavelength. These very rapid descent rates and long vertical wavelengths are inconsistent with the observations. Thus if one of these two tides is the seed for the NLC wave, then the diurnal tide is a much better candidate.

While the phase, phase velocity, and vertical wavelength of the diurnal tide are similar to the characteristics of the observed NLC wave, the amplitude of the diurnal tide is far smaller than the amplitude of the wave. The average amplitude of the two observed

and one modeled diurnal tidal results is ~4 K at the time of the wave, which has an observed maximum amplitude of 17 K at 73 km growing to 23 K at the minimum at 84 km. However, if the tidal amplitude could be enhanced or amplified, this difference could be accounted for. Several studies have examined the interaction of breaking gravity waves with the mean flow or the diurnal tidal winds. *Walterscheid* [1981] suggests a cooling high in the mesosphere. More recent works [*Liu and Hagan*, 1998; *Liu*, 2000; *Liu et al.*, 2000] have specifically looked at the interaction with tides. While their purpose was to try to explain the temperature enhancements in mesospheric inversion layers, their mechanism may also be very applicable in this situation. Like *Walterscheid* [1981], they produced a cooling at higher altitudes. However, in addition, they produced a warming at lower altitudes. This might account for an enhanced diurnal tide or, in this case, the large-amplitude wave.

Although speculative, this second NLC observation at ALO is consistent with the idea of increased gravity-wave generation in the troposphere in the Mountain West, and leads to a large enhancement of the diurnal tide in the upper mesosphere. The negative or cold portion of this enhanced tide then produces low enough temperatures to enable an NLC to develop. This could be a unique event from unusual local circumstances. Or, if these mid-latitude NLCs are truly a recent recurring phenomenon, this could be a manifestation of climate change in the troposphere that is coupled to the mesosphere via gravity waves.

5. Conclusions

Previously, we showed [*Wickwar et al.*, 2002] the first NLC detected by lidar

below 50° latitude. Here, we present the second NLC detected below 50° latitude. It was observed at the same location at 41.7°N on 22 June 1995, 4 years earlier. This detection was found during a systematic re-analysis of the ALO Rayleigh-scatter data searching for NLCs. While no visual observations could have been made, this is definitely another mid-latitude NLC: there is an enhanced backscatter ratio; it occurs near summer solstice; it occurs in the usual NLC altitude range; the enhancement is confined to a thin layer; this layer is located at a very low temperature minimum; and the layer descends slowly with time.

To date this is the second reported lidar observation of an NLC below 50°. It shows that the first observation was not an anomaly and further suggests that additional NLCs could have occurred at mid and lower latitudes, but were not detected. It is somewhat surprising that this second detection was from the same location in the Mountain West. To our knowledge, the June 1995 observation at ALO is the first time that Rayleigh lidar data have been analyzed for the coincident neutral temperatures. In an unexpected result, this second NLC was found at the minimum of a large-amplitude vertical temperature wave. The wave was characterized by a cold phase with an amplitude of ~23 K near 84 km and a warm phase, maximizing 11 km lower, with an amplitude of ~17 K, a vertical wavelength of 22 km, and a deduced downward phase velocity of ~—0.9 km/hr. The apparent wave modulation was probably essential for producing the low temperatures necessary for formation of the NLC ice crystals. The Michelson Interferometer observations suggest that the temperature minimum in the wave may have been further lowered by interannual variability. The phase, phase velocity, and vertical wavelength of this wave suggest that it is an enhanced diurnal tide.

Modeling results in the literature, performed for other reasons, suggest that the diurnal tide could be significantly enhanced by interactions with gravity waves propagating from below.

While the first NLC detection led to speculation about global change having either lowered mesospheric temperatures or increased mesospheric water vapor and its freezing point, the temperatures and the large-amplitude wave in this detection lead to different speculation. Below 60 km or so, the temperatures on 22 June 1995 were close to the climatological mean derived from lidar observations between 1994 and 2004. Above that altitude, the temperatures are dominated by a large-amplitude wave that appears to grow with altitude in both the lidar and Michelson Interferometer results. The climatological temperatures are not cold enough to produce NLCs. Thus, the NLC did not arise from overall mesospheric cooling. It was definitely helped by the large-amplitude wave, which lowered the temperatures to ~150 K at 84 km and ~125 K at ~87 km. These temperatures are typical of the higher temperatures observed at high latitudes at which NLCs are found. Possibly, its formation was also helped by increased water vapor, but we do not have information on that.

The speculation about the origin of the NLC has to turn from a significant mesospheric cooling to the origin of this large-amplitude wave or to the gravity waves that may have caused it by, perhaps, enhancing the diurnal tide. This large-amplitude wave might have been a unique event, although the temperatures on the next day, 23 June 1995, suggest otherwise, or it might be a very different manifestation of global change. If caused by a change in the gravity waves reaching the upper mesosphere, then either the gravity-wave source has to be enhanced or the filtering between the source region and the

upper mesosphere has to be reduced. Either of these possibilities suggests changes in wind systems. If large-amplitude mesospheric waves are localized in longitude to the Mountain West, as weakly suggested by the absence of mid-latitude NLC observations elsewhere, then perhaps it is the orographic gravity wave source that is enhanced. Another possibility would be the enhancement of the convection source, which is active considerably to the east and south of ALO. If that were the case, then we would predict that the Purple Crow lidar, another mid-latitude lidar, should also detect NLCs and these large vertical mesospheric waves.

Further investigating the origin of these mid-latitude NLCs will require more systematic, simultaneous, long-term observations with Rayleigh-scatter lidars at ALO and other locations. More sensitive lidars would improve the observations by obtaining data from higher altitudes, thereby minimizing uncertainties in the background and providing better time resolution. As demonstrated in this paper, significant additional information can be obtained by having a cluster of instrumentation providing more extensive observations. The Michelson Interferometer provided valuable, mesospheric temperature observations. It would be valuable if other instruments could provide mesospheric wind measurements, and if still others could provide temperature or density measurements from the upper troposphere into the mesosphere.

CHAPTER 6

SUMMARY AND FUTURE WORK

1. Summary and Conclusions

The Rayleigh-scatter lidar has proven a useful tool in making measurements of the middle atmosphere. The short pulse length of the transmitter and high repetition rate enable high temporal-resolution measurements of vertical profiles of relative density. These profiles are used to produce absolute temperatures. The Rayleigh-scatter lidar technique can provide accurate temperature measurements between 20, or a little above, and 110 km. The lowest altitude is dependent on the atmosphere's aerosol content, and the upper boundary is limited by the assumptions used in the temperature reduction. The Rayleigh-scatter lidar coverage of the middle atmosphere covers the gap in radar coverage and more importantly provides an absolute temperature measurement.

As previously mentioned, the Rayleigh-scatter temperatures are independent of any system calibration. The significance of this is two-fold. Temperatures derived in this manner are absolute, providing a gold standard for temperature comparisons. The second, and more subtle effect, is that the equipment used in making the temperature measurements can be continually updated and improved without affecting the data or the validity of the results as no calibration is needed. This is particularly important for long term temperature observations, during which equipment is likely to change or be replaced or improved. For example, the pass band of interference filters can drift in wavelength with age. For Rayleigh-lidar this results in a signal loss, but does not affect the

temperature calculation. The same cannot be said for instruments that rely on precise transmission profiles such as mesospheric temperature mappers or resonance lidars.

The nighttime temperature measurements from the ALO Rayleigh-scatter climatology spanning 11 years were combined into a single composite year. A 31-day window was used to combine the data, by day number, into approximate monthly averages. This average was performed with the window centered on each day of the year to generate a single composite year from the 11-year database of nighttime temperature measurements.

A comparison of the ALO climatology to a similar temperature climatology from the French lidar group showed good agreement in general. However, a couple of significant differences stood out. First, a systematic difference appeared in the summer temperatures in the lower mesosphere, which is when and where the geophysical variability is minimal. The ALO temperature climatology was found to be ~1.5 K cooler than the French climatology. Because the midpoint of the French climatology is 12.5 years prior to the midpoint of the ALO climatology, this suggests that the difference arises from a general mesospheric cooling at the rate of ~1.2 K/decade during this interval. While it is tempting to attribute this cooling to global change, especially when this value agrees well with other trend values in the literature [e.g., *Beig et al.*, 2003], it is difficult to do so when the comparison is not from the same time period or from a full trend analysis. A full trend analysis of the ALO temperatures is under way as a Ph.D. research project at USU.

Second, large temperature differences exist in the winter months, which may arise from averaging the temperature effects of large mesospheric inversion layers. Of

particular interest were regions during February and December where ALO temperatures were 7-9 K warmer than the French values. With inversion layers having a large influence on the temperature profiles between November and February, it is highly likely that the observed differences in the climatologies arise from averaging their effects above two sites. These differences might be longitudinal, reflecting differences in the dynamical features that lead to the inversion layers, or they might represent the effects of large inversion layers during a few winters distorting the averages at the two locations in different ways. More information on what may be happening will come from a study of inversion layers at ALO that is currently underway. Depending on what is found, it will take more observations or simultaneous observations to determine the origin of these differences.

The NRL MSIS–00 empirical model, which is composed of historical observations, is commonly used as a temperature reference. Comparing the global MSISe00 model to the absolute temperatures in the ALO mid-latitude climatology is a way of evaluating how good the model is at mid-latitudes. It was found that on average the model differed from the climatology by less than 5 K between 45 and 80 km. The sign of the temperature difference for an annual average varied with the model being warmer between 45 to 51 km, cooler from 51 to 61 km, and warmer from 61 to 78 km, and cooler from 78 to 85 km. This oscillatory temperature difference is possibly a result of harmonic fitting used in generating the model. The stratopause altitudes agreed well, but the onset of the summer maximum occurs earlier in the model.

On shorter time scales, the largest difference between the model and climatology are in the upper mesosphere during mid-summer when the mesopause temperatures reach

a minimum. The model was 17 K cooler than the climatology at 84 km in June and July. These very cold model temperatures are more appropriate for higher latitudes. This large difference could have a significant impact on, for instance, the conclusions deduced from a first principle model used to deduce energy sources and sinks in this region near the summer mesopause. Slightly smaller differences are also found during the winter in the region where mesospheric inversions are observed in the climatology. The use of the model would suggest that the mid-latitude mesosphere is much less variable than it is. Because these winter inversion layers are predominately observed at mid-latitudes their absence in the model again illustrates the minimal amount of detailed mid-latitude observations are included into the MSIS–00 model. The next revision should include more mid-latitude mesospheric data.

To further expand on the qualitative comparison of MSIS–00 to the ALO climatology, the annual, semi-annual and higher order oscillations were found for the two composite years. The annual amplitude in the model is smaller than the observed value over the majority of the compared region, up to about 75 km. A minimum in the annual amplitude is found in both the model and the climatology near 63 km. The model however has a near zero minimum compared to an observed minimum of 2 K. Below the minimum, the phase maximum is in summer reflecting the importance of radiative heating; above the minimum, the phase maximum is in winter reflecting the importance of dynamical heating. Compared to the observations, the phase change in the model is abrupt and progresses in the opposite direction. The contribution of inversion layers to the climatology is responsible for the direction of the phase change in the observations.

The amplitude of the semi-annual oscillation is smaller than the annual term in general. The exception in the climatology is a maximum near 63 km, at the minimum in the annual variation. This maximum is not observed in the model. Above 75 km the model shows a large increase in the amplitude of the semi-annual term that is not observed in the climatology. The phase of the semi-annual term shows good agreement at 45 km. However, above this altitude the model lags the climatology and at some points is 125 degrees out of phase with it giving rise to some of the observed differences. In the climatology the higher-order terms are found to make small but statistically significant contributions to the temperature structure, but are not included in the model.

The all-night averages and 31-day averages have averaged the short-period gravity waves out of the temperature climatology. However, the location of the ALO facility is in the Rocky Mountains and places it in a strong source region of orographically generated gravity waves. During the winter, these gravity waves can propagate into the mesosphere, possibly contributing to the inversion layers and affecting the planetary waves.

On two separate occasions NLCs were observed by the ALO Rayleigh-scatter lidar. This initial observation was the first lidar detection of NLCs equatorward of 50° N and was taken as a significant indicator of global change. An examination of the lidar database revealed that a prior NLC event occurred in 1995. During the night of the 1995 observation a large amplitude oscillation was observed in the temperature profile, suggesting a more complicated situation than simple cooling from global change.

As evident in the ALO temperature climatology, the cool temperatures in the summer mesopause region are insufficient for the formation of NLCs, which typically

occur at temperatures less than 150 K. The presence of this wave suggests that it played a key role in lowering the temperature, enabling the generation and growth of this mid-latitude NLC. A comparison of this wave to tides, from model and lidar observations, shows very good agreement to the phase and vertical wavelength of the diurnal tide. However, the observed amplitude of the diurnal tide is much smaller than that of the observed oscillation, suggesting that if the diurnal tide were associated with this wave it was greatly amplified. The amplification mechanism is a topic of debate in the literature, but interaction of gravity waves with the tides is a possibility.

While there are several mid-latitude lidar facilities, to date NLCs have only been observed over the ALO facility. This suggests that the presence of NLCs is linked to the observing conditions above ALO. It therefore seems reasonable to suspect that the orographically generated gravity waves over the Mountain West are involved in generating the large amplitude wave. However, these waves should be strongly filtered by the westward directed background winds in the upper stratosphere and lower mesosphere. That suggests that convectively generated gravity waves may be responsible for producing the conditions leading to the large amplitude wave. However, if this were the case, then NLCs should be observed at other locations closer to where heavy convection occurs. Given the limited information presented by this single observation it is not possible to determine the gravity wave source. However, a large database of lidar observations at ALO is available and may possess additional information.

2. Future Work

With the development of the ALO climatology, a set of reference temperatures

has been created. These average temperature profiles can be used to further study the database of nighttime temperatures at ALO. For instance, for a given day number, the average temperature profile from the climatology can be subtracted from an individual nighttime average. In this manner the deviations can be examined for a variety of phenomena. It can be examined for additional large amplitude oscillations, such as the one attributed to the formation of the 1995 NLC and, perhaps, the 1999 NLC. This approach could also be used to examine mesospheric inversion layers. Previous studies have examined the temperature profiles, particularly the regions with a positive temperature gradient, instead of the departures from the average behavior. These differences could also be the starting point for examining temporal and spatial frequencies for portions of the spectra of wave behavior.

Examination of these temperature differences as a function of time would facilitate the investigation of medium term variations such as might arise from the 81-day solar rotation, sudden stratospheric warmings, and long-period planetary waves. The effects of planetary waves are already being investigated with the ALO data. In addition, at the lowest altitudes, near 45 km, differences between the nightly temperatures and the climatology are already showing significant differences on the scale of one to several days. These are being investigated in another ALO research project at USU and they appear to be related to effects from weather systems in the troposphere.

Temperature differences found between the ALO and French climatologies, particularly in the summer, were used to derive cooling trends at several altitudes. In compiling the ALO climatology, a 31-day average was formed using only the day number. Averaging the data in this manner could influence the trend values found. If for

example the majority of the summertime values were collected during solar minimum at one site and solar maximum at the other, then the results might be biased. This initial comparison needs to be the starting point for more detailed analyses. A comparison of overlapping data needs to be made and a full trend analysis performed. The latter is already underway at USU on the ALO data.

While the absolute measurements from the Rayleigh-scatter lidar are temperatures in the middle atmosphere, a significant dataset of relative density measurements also exists. It was the first step in the temperature analysis. Whereas the temperature calculations require long integration times, which average out the short-period gravity waves, the relative densities do not. Gravity wave spectra can be analyzed from the density data using integrations times as short as 2 minutes. In addition, density fluctuations would also enable the study of potential energy carried upward by the waves.

The accuracy of the temperature measurements is dependent on the magnitude of the returns and the accuracy in the initialization temperature. Increasing the collecting area of the lidar telescope, the laser power, or both, would significantly increase the maximum range, improve the altitude and time resolutions, and increase the precision. The greater range would lead to better accuracy at the highest altitudes reported here. Large aperture telescopes are possible, but the material costs and associated manufacturing labor increase dramatically with the diameter. However, for lidar measurements there is no need to image a distant object: the telescope is basically a light bucket. Therefore, multiple telescopes can be coupled together to create an equivalent large collecting area without the need to match wavefronts from each telescope. To increase the collecting area of the ALO facility four 50-inch parabolic mirrors have been

purchased and installed in a steerable telescope mount close to present lidar. The author has obtained the first light from one of the mirrors. When properly aligned, the four mirrors will increase the effective collecting area of the receiver by a factor of 30 extending the altitude range by at least 20 km. In addition, a second, slightly more powerful Nd:YAG laser has been acquired. The 30-Hz pulses from the two lasers can be interleaved to more than double the emitted power. The author has already developed the software needed to control the timing to interleave the pulses. The combined effect of greater collecting area and laser power would increase the lidar sensitivity by a factor of 60. The power-aperture product would increase from 2.6 W/m^2 to 213 W/m^2, making this the most powerful Rayleigh lidar in the world. Alternately put, a factor of 60 would give the same signal-to-noise ratio at 110 km as is now obtained at 85 km. This would open the possibility for many new scientific studies of phenomena that would extend across the transition from the mesosphere to the thermosphere. It may then become necessary to examine the effect of changing neutral composition on the data interpretation at the highest altitudes.

The dependence of the Rayleigh-scatter temperature on the initialization temperature adds uncertainty to the top 10 km. In addition to a larger telescope and greater power, another way to reduce this uncertainty is to add a resonance lidar to the facility. An alexandrite laser, set up to operate at the potassium resonance line, has been added to the ALO facility. The author did much of that set up. Its simultaneous operation would enable temperature measurements between 80 and 110 km. These temperatures with their associated small uncertainties could then be used to more accurately initialize the Rayleigh-scatter temperatures than climatological or model

temperature values. Moreover, these would be simultaneous temperatures that would take into account variations caused by transient events. This would be much better than using climatological values. The upgraded system would enable accurate temperatures to be derived from 30 km to 110 km.

This greater range would also enable better comparisons with temperatures derived from observations of airglow emissions from OH, $O(^1S)$, and O_2 Atmospheric band. Initial comparisons with the current system suggest the possibility of systematic differences that need to be more fully examined [*Herron*, 2004]. In principle, these comparisons could enable the altitudes of the airglow emissions to be determined.

The use of this new steerable telescope would also enable studies of horizontal spatial structures in addition to vertical structures. Coupled with the potassium resonance lidar, it would also enable wind measurements between 80 and 110 km.

REFERENCES

Baker, D. J., and A. T. Stair, Jr. (1988), Rocket measurements of the altitude distributions of the hydroxyl airglow, *Physica Scripta*, *37*, 611–622.

Barnett, J., and M. Corney (1985), Temperature data from satellites, in *MAP Handbook*, edited by K. Labitzke, et al., pp. 3–11, SCOSTEP, Urbana, Ill.

Beig, G., P. Keckhut, R. P. Lowe, R. G. Roble, M. G. Mlynczak, J. Scheer, V. I. Fomichev, D. Offermann, W. J. R. French, M. G. Shepherd, A. I. Semenov, R. E. E., C. Y. She, F. J. Lubken, J. Bremer, B. R. Clemesha, J. Stegman, F. Sigernes, and S. Fadnavis (2003), Review of mesospheric temperature trends, *Reviews of Geophysics*, *41*(4), 1015, doi:10.1029/2002RG000121.

Burns, G. B., T. D. Kawahara, W. J. R. French, A. Nomura, and A. R. Klekociuk (2003), A comparison of hydroxyl rotational temperature from Davis (69°S, 78°E) with sodium lidar temperatures from Syowa (69°S, 39°E), *Geophys. Res. Lett.*, *30(1)*(1025), doi:10.1029/2002GL016413.

Chandra, S., C. H. Jackman, E. L. Fleming, and J. M. Russell (1997), The seasonal and long term changes in mesosphere water vapor, *Geophys Res. Lett.*, *24*(6), 639-642, doi: 10.1029/1997GL00546.

Chanin, M.-L. (1984), Review of lidar contributions to the description and understanding of the middle atmosphere, *J. Atmos. Terr. Phys.*, *46*, 987–993.

Chanin, M.-L., and A. Hauchecorne (1984), Lidar studies of temperature and density using Rayleigh scattering, in *Ground-Based Techniques*, edited by R. A. Vincent, pp. 87–98, SCOSTEP Secretariat, University of Illinois, Urbana, Ill.

Christensen, A. B., L. J. Paxton, S. Avery, J. Craven, G. Crowley, D. C. Humm, H. Kil, R. R. Meier, C.-I. Meng, D. Morrison, B. S. Ogorzalek, P. Straus, D. J. Strickland, R. M. Swenson, R. L. Walterscheid, B. Wolven, and Y. Zhang (2003), Initial observations with the Global Ultraviolet Imager (GUVI) in the NASA TIMED satellite mission, *J. Geophys Res.*, *108*(A12), 1451, doi: 10.1029/2003JA009918.

Chu, X., C. Gardner, and R. G. Roble (2003), Lidar studies of interannual, seasonal, and diurnal variations of polar mesospheric clouds at the South Pole, *J. Geophys. Res*, *108*(D8), 8447, doi:10.1029/2002JD002524.

Chu, X., G. J. Nott, P. J. Espy, C. S. Gardner, J. C. Diettrich, M. A. Clilverd, and M. J. Jarvis (2004), Lidar observations of polar mesospheric clouds at Rothera, Antartica (67.5°S, 68.0°W), *Geophys Res. Lett.*, *31*(L02114), doi:10.1029/2003GL018638.

Clancy, R. T., and D. W. Rusch (1989), Climatology and trends of mesospheric (58–90 km) temperatures based upon 1982–1986 SME limb scattering profiles, *J. Geophys. Res.*, *94*, 3377–3393.

Clancy, R. T., D. W. Rusch, and M. T. Callan (1994), Temperature minima in the average thermal structure of the middle mesosphere (70–80 km) from analysis of 40– to 92–km SME global temperature profiles, *J. Geophys. Res.*, *99*, 19001–19020, doi: 10.1029/93JD03471.

Collins, R. L., M. C. Kelly, M. J. Nicolls, C. Ramos, T. Hou, T. E. Stern, K. Mizutani, and T. Itabe (2003), Simultaneous lidar observations of a noctilucent cloud and an internal wave in the polar mesosphere, *J. Geophys. Res*, *108*(D8), 8435, doi:8410.1029/2002JD002427.

Espy, P. J., R. Huppi, and A. Manson (1995), Large-scale, persistent latitude structures in the mesospheric temperature during ANLC-93, *Geophys. Res. Lett.*, *22*(20), 2801–2804, doi: 10.1029/95GL02873.

Espy, P. J., and J. Stegman (2002), Trends and variability of mesospheric temperature at high latitudes, *Phys. and Chem. of the Earth*, *28*, 531.

Fiedler, J., G. Baumgarten, and G. von Cossart (2003), Noctilucent clouds above ALOMAR between 1997 and 2001: Occurrence and properties, *J. Geophys. Res*, *108*(D8), 8453, doi: 10.1029/2002JD002419.

Fiedler, J., G. Von Cossart, U. Von Zahn, and W. Eriksen (1999), Stratospheric/mesospheric temperature profiles obtained by ALOMAR RMR lidar over Andøya, paper presented at 14th ESA Symposium on European Rocket and Balloon Programmes and Related Research, ESA SP-437.

Fleming, E. L., S. Chandra, J. J. Barnett, and M. Corney (1990), Zonal mean temperature, pressure, zonal wind and geopotential height as functions of latitude, *Adv. Space Res.*, *10*, (12)11–(12)59.

Gadsden, M., and W. Schroder (1989), *Noctilucent Clouds*, 190 pp., Springer-Verlag, New York.

Gardner, C. S. (1989), Sodium resonance fluorescence lidar applications in atmospheric science and astronomy, *Proceedings of the IEEE*, *77*(3), 408-418.

Gardner, C. S., J. M. C. Plane, W. Pan, T. Vondra, B. J. Murray, and X. Chu (2005), Seasonal variations of the Na and Fe layers at the South Pole and their implications for the chemistry and general circulation of the polar mesosphere, *J. Geophys. Res.*, *110*(D10302), doi:10.1029/2004JD005670.

Gardner, C. S., D. C. Senft, T. J. Beatty, R. E. Bills, and C. A. Hostetler (1989), Rayleigh and sodium lidar techniques for measuring middle atmosphere density,

temperature and wind perturbations and their spectra, in *World Ionosphere/Thermosphere Study, WITS HANDBOOK*, edited by C. H. Liu, pp. 148–187, SCOSTEP Secretariat, University of Illinois, Urbana, Ill.

Hagan, M., M. D. Burrage, J. M. Forbes, J. Hackney, W. J. Randel, and X. Zhang (1999), GSWM-98: Results for migrating solar tides, *J. Geophys. Res.*, *104*(A4), 6813-6827, doi: 10.1029/1998JA900125.

Hagan, M., R. G. Roble, and J. Hackney (2001), Migrating thermospheric tides, *Journal of Geophysical Research*, *106*(A7), 12739-12752, doi: 10.1029/2000JA000344.

Hansen, G., M. Serwazi, and U. von Zahn (1989), First detection of a noctilucent cloud by lidar, *Geophys. Res. Lett.*, *16*, 1445–1448.

Hauchecorne, A., M.-L. Chanin, and P. Keckhut (1991), Climatology and trends of the middle atmospheric temperature (33–87 km) as seen by Rayleigh lidar over the south of France, *J. Geophys. Res.*, *96*, 15297–15309.

Hauchecorne, A., and M. L. Chanin (1980), Density and temperature profiles obtained by lidar between 35 and 70 km, *Geophys. Res. Lett.*, *7*, 565-568.

Hauchecorne, A., M. L. Chanin, and R. Wilson (1987), Mesospheric temperature inversion and gravity wave breaking, *Geophys. Res. Lett.*, *14*, 933-936.

Hedin, A. (1996), MSIS model limitations, edited by V. Wickwar, Logan, Utah.

Hedin, A. E. (1987), MSIS-86 thermospheric model, *J. Geophys. Res.*, *92*, 4649-4662.

Hedin, A. E. (1991), Extension of the MSIS thermosphere model into the middle and lower atmosphere, *J. Geophys. Res.*, *96*(A2), 1159-1172.

Hedin, A. E., N. W. Spencer, and T. L. Killeen (1988), Empirical global model of upper thermosphere winds based on atmosphere and dynamics explorer satellite data, *J. Geophys. Res.*, *93*, 9959-9978.

Herron, J. P. (2004), Mesospheric Temperature Climatology Above Utah State University, M.S. thesis, 156 pp., Utah State University, Logan.

Herron, J. P., V. B. Wickwar, P. J. Espy, and J. W. Meriwether (2007), Observations of a Noctilucent Cloud above Logan, Utah (41.7 N, 111.8 W) in 1995, *J. Geophys Res.*, in press, doi: 10.1029/2006JD007158.

Hervig, M., R. E. Thompson, M. McHugh, L. L. Gordley, J. Russell, and M. E. Summers (2001), First confirmation that water ice is the primary component of polar mesospheric clouds, *Geophys. Res. Lett.*, *28*(6), 971-974, doi: 10.1029/2000GL012104.

Huang, F. T., H. G. Mayr, C. A. Reber, J. M. Russell, M. Mlynczak, and J. Mengel (2006), Zonal-mean temperature variations inferred from SABER measurements on TIMED compared with UARS observations, *J. Geophys. Res.*, *111*, A10S07, doi: 10.1029/2005JA011427.

Keckhut, P. (1995), Mid-latitude summer response of the middle atmosphere to short-term solar UV changes, *Annales Geophysicae*, *13*(6), 641–647.

Keckhut, P., A. Hauchecorne, and M.-L. Chanin (1993), A critical review of the database acquired for the long-term surveillance of the middle atmosphere by the French Rayleigh lidars, *J. Atm. Oceanic Tech.*, *10*, 850–867.

Keckhut, P., A. Hauchecorne, and M. L. Chanin (1995), Midlatitude long-term variability of the middle atmosphere: Trends and cyclic and episodic changes, *J. Geophys. Res.*, *100*(D9), 18887–18897, doi: 10.1029/95JD01387.

Kofman, W., F. Bertin, J. Rottger, A. Cremieux, and P. J. S. Williams (1984), The EISCAT mesospheric measurements during the CAMP campaign, *J. Atmos. Terr. Phys.*, *46*, 565-575.

Langer, M., K. P. Müller, and K. H. Fricke (1995), Rayleigh lidar detection of aerosol echos from noctilucent cloud altitudes at the Arctic circle, *Geophys. Res. Lett.*, *22*(4), 381–384, doi: 10.1029/94GL02903.

Lathuillere, C., V. B. Wickwar, and W. Kofman (1983), Incoherent-scatter measurements of ion-neutral collision frequencies and temperatures in the lower thermosphere of the auroral region, *J. Geophys. Res.*, *88*, 10137-10144.

Leblanc, T., A. Hauchecorne, M.-L. Chanin, C. Rogers, F. Taylor, and N. Livesey (1995), Mesospheric temperature inversions as seen by ISAMS in December 1991, *Geophys Res. Lett.*, *22*(12), 1485–1488, doi: 10.1029/94GL03274.

Leblanc, T., I. S. McDermid, P. Keckhut, A. Hauchecorne, C. Y. She, and D. A. Krueger (1998), Temperature climatology of the middle atmosphere from long-term lidar measurements at middle and low latitudes, *J. Geophys. Res.*, *103*(D14), 17191–17204, doi: 10.1029/98JD01347.

Leblanc, T., I. S. McDermid, and D. A. Ortland (1999), Lidar observations of the middle atmospheric thermal tides and comparison with the High Resolution Doppler Imager and Global-Scale Wave Model: 1. Methodology and winter observations at Table Mountain (34.4°N), *J. Geophys. Res.*, *104*(D10), 11917–11929, doi: 10.1029/1999JD900007.

Liu, G., and G. G. Shepherd (2006), An empirical model for the altitude of the OH nightglow emission, *Geophys. Res. Lett.*, *33*, L09805, doi: 10.1029/2005GL025297.

Liu, H.-L. (2000), Temperature changes due to gravity wave saturation, *J. Geophys. Res.*, *105*(D10), 12329-12336, doi: 10.1029/2000JD900054.

Liu, H.-L., and M. E. Hagan (1998), Local heating / cooling of the mesosphere due to gravity wave and tidal coupling, *Geophys Res. Lett.*, *25*(15), 2941–2944, doi: 10.1029\98GL02153

Liu, H.-L., M. E. Hagan, and R. G. Roble (2000), Local mean state changes due to gravity wave breaking modulated by the diurnal tide, *J. Geophys. Res.*, *105*(D10), 12381–12396, doi: 10.1029/1999JD901163.

Liu, H.-L., and J. W. Meriwether (2004), Analysis of a temperature inversion event in the lower mesopshere, *J. Geophys. Res.*, *109*, D02S07, doi: 10.1029/2002JD003026.

Lübken, F.-J. (1999), Thermal structure of the Arctic summer mesosphere, *J. Geophys. Res.*, *104*(D8), 9135–9149, doi: 10.1029/1999JD900076.

Lübken, F.-J., K.-H. Fricke, and Langer (1996), Noctilucent clouds and the thermal structure near the Arctic mesopause in summer, *J. Geophys. Res.*, *101*(D5), 9489–9508, doi: 10.1029/96JD00444.

Lübken, F.-J., and U. von Zahn (1991), Thermal structure of the mesopause region at polar latitudes, *J. Geophys. Res.*, *96*, 20841–20857.

Measures, R. M. (1992), *Laser Remote Sensing Fundamentals and Applications*, 510 pp., Krieger Publishing Company, Malabar, FL.

Meier, R. R., J. M. Picone, D. P. Drob, and R. G. Roble (2001), Similarity transformation-based analysis of atmospheric models, data, and inverse remote sensing algorithms, *J. Geophys. Res.*, *106*(A8), 15519-15532, doi: 10.1029/2001JA000062.

Meriwether, J. W., X. Gao, V. B. Wickwar, T. D. Wilkerson, K. C. Beissner, S. C. Collins, and M. E. Hagan (1998), Observed coupling of the mesosphere inversion layer to the thermal tidal structure, *Geophys. Res. Lett.*, *25*, 1479–1482 & 2127, doi: 10.1029/98GL00756.

Meriwether, J. W., and A. J. Gerrard (2004), Mesosphere Inversion Layers and Stratosphere Temperature Enhancements, *Reviews of Geophysics*, *42*, RG3003, doi:10.1029/2003RG000133.

Nedoluha, G. E., R. M. Bevilacqua, R. M. Gomez, B. C. Hicks, J. M. Russell, and B. J. Connor (2003), An evaluation of trends in middle atmosphere water vapor as measured by HALOE, WVMS, and POAM, *J. Geophys. Res*, *108*(D13), 4391, doi: 10.1029/2002JD003332.

Nelson, K., and V. B. Wickwar (2007), Detection of tidal, planetary and secondary waves in nighttime lidar data. Technique and application to winter mesospheric temperatures above Logan, Utah (to be submitted).

Picone, J. M., A. E. Hedin, D. P. Drop, and A. C. Aikin (2002), NRLMSISE-00 empirical model of the atmosphere: Statistical comparisons and scientific issues, *J. Geophys. Res.*, *107*(A12), 1468, doi: 10.1029/2002JA009430.

Remsberg, E. E., G. Lingenfelser, V. L. Harvey, W. Grose, J. M. Russell, M. Mlynczak, L. L. Gordley, and B. T. Marshall (2003), On the verification of quality of SABER temperature, geopotential height, and wind fields by comparison with Met Office assimilated analyses, *J. Geophys Res.*, *108*(D20), 4628, doi: 10.1029/2003JD003720.

Roble, R. G. (1996), The NCAR thermosphere-ionosphere-mesosphere-electrodynamics general circulation model (TIME-GCM), in *STEP: Handbook of ionospheric models*, edited by R. W. Schunk, pp. 281–288, Utah State University/SCOSTEP, Logan, Utah.

Roble, R. G., and E. C. Ridley (1994), A thermosphere-ionosphere-mesosphere-electrodynamics general circulation model (time-GCM): Equinox solar cycle minimum simulations (30-500 km), *Geophys. Res. Lett.*, *21*(6), 417-420, doi: 10.1029/93GL03391.

Schmidlin, F. J. (1976), Temperature inversions near 75 km, *Geophys. Res. Lett.*, *3*, 173-176.

She, C. Y., S. Chen, Z. Hu, J. Sherman, J. D. Vance, V. Vasoli, M. A. White, J. R. Yu, and D. A. Krueger (2000), Eight-year climatology of nocturnal temperature and sodium density in the mesopause region (80 to 105 km) over Fort Collins, CO (41°N, 105°W), *Geophys. Res. Lett.*, *27*(20), 3289-3292, doi: 10.1029/2000GL003815.

She, C. Y., S. Chen, B. P. Williams, Z. Hu, and D. A. Krueger (2002), Tides in the mesopause region over Fort Collins, Colorado (41°N, 105°W) based on lidar temperature observations covering full diurnal cycles, *J. Geophys. Res.*, *107*(D18), 4350, doi: 10.1029/2001JD001189.

She, C. Y., and R. P. Lowe (1998), Seasonal temperature variations in the mesopause region at mid-latitude: comparison of lidar and hydroxyl rotational temperatures using WINDII/UARS OH height profiles, *J. Atmos. Solar Terr. Phys.*, *60*, 1573–1583.

She, C. Y., S. W. Thiel, and D. A. Krueger (1998), Observed episodic warming at 86 km and 100 km between 1990 and 1997: Effects of Mount Pinatubo eruption, *Geophys. Res. Lett.*, *28*(9), 1899-1902, doi: 10.1029/98GL00178.

She, C. Y., and U. von Zahn (1998), The concept of two-level mesopause: Support through new lidar observation, *J. Geophys. Res.*, *103*(d5), 5855-5863, doi: 10.1029/97JD03450.

Shepherd, M. G., W. F. J. Evans, G. Hernandez, D. Offermann, and H. Takahashi (2004a), Global variability of mesospheric temperature: Mean temperature field, *J. Geophys Res.*, *109*, D24117, doi: 10.1029/2004JD005054.

Shepherd, M. G., B. Prawirosoehardjo, S. Zhang, B. H. Solheim, G. G. Shepherd, V. B. Wickwar, and J. P. Herron (2001), Retrieval and validation of mesospheric temperatures from WINDII observations, *J. Geophys. Res.*, *104*(A11), 24813-24829, doi: 10.1029/2000JA000323.

Shepherd, M. G., J. Stegman, W. Singer, and R. G. Roble (2004b), Equinox transition in wind and airglow observations, *J. Atmos Terr. Phys.*, *66*, 481–491.

Sica, R. J., S. Sargoytchev, P. S. Argall, E. F. Borra, L. Girard, C. T. Sparrow, and S. Flatt (1995), Lidar measurements taken with a large-aperture liquid mirror. 1. Rayleigh-scatter system, *Appl. Optics*, *34*(30), 6925–6936.

States, R. J., and C. S. Gardner (2000a), Thermal structure of the mesopause regioin (80–105 km) at 40°N latitude. Part II: Diurnal Variations, *J. Atmos. Sci.*, *57*(1), 78–92, doi: 10.1175/1520-0469(2000)57<078:TSOTMR>2.0.CO;2.

States, R. J., and C. S. Gardner (2000b), Thermal structure of the mesopause region (80–105 km) at 40°N latitude. Part I: Seasonal Variations, *J. Atmos. Sci.*, *57*(1), 66–77, doi: 10.1175/1520-0469(2000)57<066:TSOTMR>2.0.CO;2.

Stebel, K., U. Blum, K.-H. Fricke, S. Kirkwood, N. J. Mitchell, and A. Osepain (2004), Joint radar/lidar observations of possible aerosol layers in the winter mesosphere, *J. Atmos Terr. Phys.*, *66*, 957-970.

Taori, A., M. J. Taylor, and S. Franke (2005), Terdiurnal wave signatures in the upper mesospheric temperature and their association with the wind fields at low latitudes (20 N), *J. Geophys Res.*, *110*, D09S06, doi: 10.1029/2004JD004564.

Taylor, F. W. (2005), *Elementary Climate Physics*, 212 pp., Oxford University Press, New York.

Taylor, M. J., W. R. Pendleton, H.-L. Liu, C. Y. She, C. Gardner, R. G. Roble, and V. Vasoli (2001), Large amplitude perturbations in mesospheric OH Meinel and 87-km Na lidar temperatures around the autumnal equinox, *Geophys. Res. Lett.*, *28*(9), 1899-1902, doi: 10.1029/2000GL012682.

Tepley, C. A., J. D. Mathews, and S. Ganguly (1981), Incoherent scatter radar studied of mesospheric temperatures and collision frequencies at Arecibo, *J. Geophys Res.*, *86*(A13), 11330-11334.

Thayer, J. P., N. Nielsen, and J. Jacobsen (1995), Noctilucent cloud observations over Greenland by a Rayleigh lidar, *Geophys. Res. Letts.*, *22*(21), 2961-2964, doi: 10.1029/95GL02126.

Thomas, G. E. (1991), Mesospheric clouds and the physics of the mesopause region, *Rev. Geophys.*, *29*, 553–576.

Thomas, G. E. (1996a), Global change in the mesophere-lower thermosphere region: Has it already arrived?, *J. Atmos. Terr. Phys.*, *58*, 1629–1656.

Thomas, G. E. (1996b), Is the polar mesosphere the miner's canary of global change?, *Adv. Space Res.*, *18*(3), 49–58.

Thomas, G. E. (1997), Introduction to special section: Noctilucent cloud workshop, *J. Geophys. Res.*, *102*(D2), 1957–1958, doi: 10.1029/96JD02513.

Thomas, G. E. (2003), Are noctilucent clouds harbringers of global change in the middle atmosphere?, *Adv. Space Res.*, *32*(9), 1737-1746.

Thomas, G. E., and J. J. Olivero (1989), Climatology of polar mesospheric clouds, 2. Further analysis of Solar Mesosphere Explorer data, *J. Geophys Res.*, *94*, 14673–14681.

Thomas, G. E., J. J. Olivero, E. J. Jensen, W. Schröder, and O. B. Toon (1989), Relation between increasing methan and the presence of ice at the mesopause, *Nature*, *338*, 490–492.

Thomas, L., A. K. P. Marsh, D. P. Wareing, and M. A. Hassan (1994), Lidar observations of ice crystals associated with noctilucent clouds at middle latitudes, *Geophys. Res. Lett.*, *21*, 385–388.

von Cossart, G., J. Fiedler, and U. von Zahn (1999), Size distribution of NLC particles as determined from 3-color observations of NLC by ground lidar, *Geophys. Res. Lett.*, *26*(11), 1513–1516, doi: 10.1029/1999GL900226.

von Zahn, U. (2003), Are noctilucent clouds truly a "miner's canary" for global change?, *EOS Trans. AGU*, *84*(28), 261, doi: 10.1029/2003EO280001.

von Zahn, U., and U. Berger (2003), The altitude of noctilucent clouds: Groundbased observations and their interpretation through numerical modeling, paper presented at The 16th ESA symposium on European Rocket and Balloon Programmes and Related Research.

von Zahn, U., K. H. Fricke, R. Gerndt, and T. Blix (1987), Mesospheric temperatures and the OH layer height as derived from ground-based lidar and OH* spectrometry, *J. Atmos. Terr. Phys.*, *49*, 863-869.

von Zahn, U., and W. Meyer (1989), Mesopause temperature in polar summer, *J. Geophys. Res.*, *94*, 14647–14651.

Walterscheid, R. L. (1981), Dynamical cooling induced by dissipating internal gravity waves, *Geophys Res. Lett.*, *8*, 1235–1238.

Whiteway, J. A., A. I. Carswell, and W. E. Ward (1995), Mesospheric temperature inversions with overlying nearly adiabatic lapse rate: an indication of a well-mixed turbulent layer, *Geophys. Res. Lett.*, *22*(10), 1201-1204, doi: 10.1029/95GL01109.

Wickwar, V. B., M. J. Taylor, J. P. Herron, and B. A. Martineau (2002), Visual and lidar observations of noctilucent clouds above Logan, Utah, at 41.7°N, *J. Geophys. Res.*, *107*(D7), 10.1029/2001JD002280.

Wickwar, V. B., T. D. Wilkerson, M. Hammond, and J. P. Herron (2001), Mesospheric temperature observations at the USU/CASS Atmospheric Lidar Observatory (ALO), paper presented at Remote Sensing of the Atmosphere, Environment, and Space, Proceedings of SPIE.

APPENDICES

APPENDIX A

Permission Letter AGU

We are pleased to grant permission for the use of the material requested for inclusion in your thesis. The following non-exclusive rights are granted to AGU authors:

- All proprietary rights other than copyright (such as patent rights).
- The right to present the material orally.
- The right to reproduce figures, tables, and extracts, appropriately cited.
- The right to make hard paper copies of all or part of the paper for classroom use.
- The right to deny subsequent commercial use of the paper.

Further reproduction or distribution is not permitted beyond that stipulated. The copyright credit line should appear on the first page of the article or book chapter. The following must also be included, "Reproduced by permission of American Geophysical Union." To ensure that credit is given to the original source(s) and that authors receive full credit through appropriate citation to their papers, we recommend that the full bibliographic reference be cited in the reference list. The standard credit line for journal articles is: "Author(s), title of work, publication title, volume number, issue number, page number(s), year. Copyright [year] American Geophysical Union."

If an article was placed in the public domain, in which case the words "Not subject to U.S. copyright" appear on the bottom of the first page or screen of the article, please substitute "published" for the word "copyright" in the credit line mentioned above.

Copyright information is provided on the inside cover of our journals. For permission for any other use, please contact the AGU Publications Office at AGU, 2000 Florida Ave., N.W., Washington, DC 20009.

Michael Connolly
Journals Publications Specialist



BRITISH ANTARCTIC SURVEY
NATURAL ENVIRONMENT RESEARCH COUNCIL
Physical Science Division
Dr. Patrick J. Espy

2007.04.24

Mr. Joshua P. Herron
Center for Atmospheric and Space Sciences
Utah State University
Logan, UT 84322-4405
USA

Dear Josh,

I am pleased to grant permission for you to use the Journal of Geophysical Research-Atmospheres article entitled: "Observations of a Noctilucent Cloud above Logan, Utah (41.7° N, 111.8° W) in 1995", by Herron, Wickwar, Espy, and Meriwether (manuscript number 2006JD007158) for inclusion in your thesis. I wish you the best of luck!

Yours Sincerely,

Patrick J. Espy

Address
British Antarctic Survey
Physical Science Division
High Cross, Madingley Road
Cambridge CB3 0ET, UK

Phone
+44-1223-22 12 55

Fax
+44-1223 22 12 26

E-mail
pje@bas.ac.uk

Dear Josh

I am pleased to grant permission for the use of the material requested for inclusion in your thesis.

Congratulations!

Best wishes,

John Meriwether

Professor of Physics

Clemson University
Clemson, SC 29634

APPENDIX B

Temperature Reduction Algorithms

The following algorithms are to reduce to the 2 minute relative density profiles measured by the ALO Rayleigh-scatter. These programs produce hourly and nightly temperature averages. These programs are written in IDL.

```
Pro TemperatureReduction
    ; Program written to calculate the temperature based upon the raw data files
    ;Written by Joshua Herron, Utah State University 2002
    Time        =   30          ;Number of 2 minute profiles
                to average
    Threshold   =   1.0/16.0    ;Maximum Percent Error
                allowed
    GeoLat      =   41.742      ;Latitude
    GeoLong     =   241.19      ;Longitude
    AvgBins     =   81          ;Number of range bins for a 3
                km smoothing of the data
    MMM         =   28.9415     ;Average Mean Molecular
                Mass for the region
    RRR         =   8.31432     ;Ideal gas constant
    Altres      =   0.0375      ;Width of range bins
    Hour        =   7           ;Hour to run MSIS–00, (local
                midnight)
    BKLO        =   5000        ;start of background region
                (given as bin #)
    BKHI        =   9000        ;end of background region
                (given as bin #)
    DateInput, Timestring       ;Returns the date to be opened
    ReadBinary, TimeString, Date, Data, Headers, BKLO, BKHI     ;routine to
                open the binary files from the data acquisition system and sparse
                out the data and the header files. Also includes user input of bklo
                and bkhi
    CalculateTimes, Headers, Time, TimeProfiles, RayleighTimes  ;routine to
                calculate the hourly and nighttime averages. The indices are stored
                in RayleighTimes.
    Length      =(size(data))(2)    ; length of data arrays (should be 14005)
    Width       =(size(data))(1)    ; number of 2 minute profiles recorded
    Altprof     =Findgen(Length)*Altres+1.47+Altres/2.0  ;calculating an altitude
                axis for the data (1.47 is the altitude above sea level for the lidar)
    DayofYear, Timestring, DOY      ;routine to calculate the day of the year,
                which is needed to run MSIS
```

```
        RUNMSISe00, Geolat, Geolong, DOY, Hour, Altres, Atmosphere ;routine
                    that runs the MSIS–00 model for a given day number, hour and
                    stores the returned values in Atmosphere
        RayleighError, Data, RayleighTimes, Avgbins, CntError, PctError, Signal,
                    AvgSignal, Altprof, Bklo, Bkhi      ;Routine that averages the
                    returns together using the indices stored in RayleighTimes and also
                    calculated the count error and the percentage uncertainty.
        CalculateDensity, AvgSignal, Altres, Density      ;Routine to take the average
                    signal and calculate relative density profiles.
        Gravity, GeoLat, Geolong, Length, Altres, Gnew    ;Routine to calculate the
                    variation of gravity with altitude and produce a profile for the
                    temperature reduction.
        TopCalculation, CntError, PctError, AvgSignal, Threshold, DOY, Altprof,
                    Atmosphere, Topbin, TopTemp, Rayleightimes, timeprofiles
                        ;Routine to take the avgsignals and determine from the
                    error profiles the starting altitude for the temperature reduction.
                    This value is then associated to the MSIS–00 model of the CSU
                    temperature climatology depending on its altitude.
        TempCalculation, Altprof, Density, Gnew, RRR, MMM, Altres, Topbin,
                    Toptemp, Temperatures      ;Routine to calculate the absolute
                    temperatures from the density profile given a starting altitude and
                    temperature.
        TempError, Temperature, Altprof, PctError, Topbin, TempErr      ;Routine to
                    calculate the temperature uncertainty given the percent uncertainty
                    in the photon count rate
End

PRO DateInput, Temp
        ;Short program to prompt user for the date'
        Print, 'Enter the date'
        Print, 'Example enter 011228 for Dec 28, 2001'
        Read, Temp
        Return
END

PRO ReadBinary, Timestring, Date, Data, Headers, Bklo, Bkhi
        Year        =       STRMID(TimeString, 0,2)    ;parses out the year
        Month       =       STRMID(TimeString, 2,2)    ;parses out the month
        Day         =       STRMID(TimeString, 4,2)    ;parses out the day
        Tempname    =       FINDFILE('c:\mcs\sav\'+timestring+'.dat') ;check to
        see if raw data has already been recorded into and IDL datafile.
        IF (Tempname eq '') THEN BEGIN
                Restore, Tempname
                Length=(size(data))(1)
                Goto, jump
```

```
ENDIF
Filedir     ='c:\mcs\'+Year+Month+'\Rayleigh\'      ;file directory
Filename    =     Year+Month+Day    ;create filename
File        =     STRUPCASE(Filedir+'*'+Filename+'*.*')
Filenames   =     FINDFILE(File)
Length      =     (size(filenames))(1)   ;number of files found
Headers     =     STRARR(Length,12)
Header      =     ''
Time        =     STRARR(Length,2)
Data        =     FLTARR(Length, 14005)
Line        =     FLTARR(7)
FOR i=0, Length-1 DO BEGIN
      CD, 'c:\mcs\temp\'    ;directory for temporary files
      SPAWN, 'readmcs'+Filenames(i) +' >
      '+'c:\mcs\temp\'+Filename+'asc.'+STRTRIM(String(i),1),/hide ;call to
      binary to text conversion for mcs files
      GET_LUN, LUN
      OPENR,LUN,'c:\mcs\temp\'+Filename+'asc.'+STRTRIM(String(i),1)
      FOR j=0, 11 DO BEGIN
            READF, LUN, Header
            Headers(i,j)=Header
      ENDFOR
      k=0
      WHILE (~ EOF (LUN)) DO BEGIN
            READF, LUN, LINE
            Data(i,k:k+5)=Line(1:6)
            k=k+5
            ;text file is in five columns but is in actuality a single profile
      ENDWHILE
      Close, Lun
      File_Delete, 'c:\mcs\temp\'+Filename+'asc.'
      +STRTRIM(STRING(i),1)
      Print, i
      Width=i
      Free_lun, lun
ENDFOR
JUMP:
Date=STRMID(headers(0,4),31,8)
FOR i=0, Length-1 DO BEGIN
      Time=STRMID(headers(I,4,18,8)
      Hours=FIX(STRMID(time,0,2))
      Minutes=FIX(STRMID(time,3,2))
      Seconds=FIX(STRMID(time,6,2))
ENDFOR
Temp  = FLTARR(14005)
```

```
        FOR i=0, 14005-1 DO BEGIN
              Temp(i)=Mean(data(*,i))
        ENDFOR
        Plot, 'temp(*),ylog=1,yrange=[.1,1e7]
        Print, 'Please enter the starting point for the background'
        Read, bklo
        Pring, 'Please enter the ending point for the background'
        Read, bkhi
        Wdelete, 0
        Return
End

PRO CalculateTime  ,Headers,Time,TimeProfiles,RayleighTimes
  Length          =  (SIZE(HEADERS))(1)
  TimeProfiles    =  FLTARR(Length,4)
  FOR i=0, Length-1 DO BEGIN
    Temp          =  STRMID(Headers(i,4),18,8)
    TimeProfiles(i,0) =  STRMID(Temp,0,2)
    IF (Timeprofiles(i,0) GT 20) THEN Timeprofiles(i,0)=Timeprofiles(i,0)-24.0
    TimeProfiles(i,1) =  STRMID(Temp,3,2)
    TimeProfiles(i,2) =  STRMID(Temp,6,2)
    TimeProfiles(i,3) =  TimeProfiles(i,0)*3600.0+TimeProfiles(i,1)*60.0
                         +TimeProfiles(i,2)
    print, timeprofiles(i,0),timeprofiles(i,1),timeprofiles(i,2)
  ENDFOR
  StartTime     = TimeProfiles(0,3)   ;Initial time of the lidar run
  StartHour     = TimeProfiles(0,0)   ;Initial hour of the lidar run
  IntTime       =  Time*2.0*60.0    ;Seconds to start integration time
  IF ((StartTime) GT (StartHour*3600.0+1800.0)) THEN BEGIN
    FirstHour   = (StartHour+1.0)*3600+1800
  ENDIF ELSE BEGIN
    FirstHour   = StartHour*3600+1800
  ENDELSE
  RayleighTimes  =  INTARR(35,3)
  RayleighTimes(0,0) =  0
  Length        =  (SIZE(TimeProfiles))(1)
  HRS           =  ((TimeProfiles(Length-1,3)-TimeProfiles(0,3))/3600)
  IF (HRS LT 1.0) THEN BEGIN
    PRINT, 'There is less than an hours worth of data'
    PRINT, 'Hours =',HRS
  ENDIF
  i=0
  WHILE (TimeProfiles(i,3) LE FirstHour) DO i=i+1   ;Find the point for the first hour
  RayleighTimes(1,0) =  i
  HourRecord      = i
```

```
  k        =  1
  FOR i=HourRecord+1,Length-1 DO BEGIN
    IF ((TimeProfiles(HourRecord,3)+IntTime*k) LE (TimeProfiles(i,3))) THEN
              BEGIN
     RayleighTimes(k+1,0)=i
     k       =  k+1
    ENDIF
  ENDFOR
  RayleighTimes =  RayleighTimes(0:k+1,*)
  k =  (SIZE(RayleighTimes))(1)-2
  FOR j=0,k-1 DO BEGIN
    Temp       = RayleighTimes(j+1,0)
    RayleighTimes(j,1)  = Temp-1
    RayleighTimes(j,2)  = Temp-RayleighTimes(j,0)
  ENDFOR
  RayleighTimes(k,1)   = Length-1
  RayleighTimes(k,2)   = Length-RayleighTimes(k,0)
  RayleighTimes(k+1,0)  = 0
  RayleighTimes(k+1,1)  = Length-1
  RayleighTimes(k+1,2)  = Length-1
  RETURN
END

PRO DAYOFYEAR  ,Date,DOY
  MD   = [0,31,28,31,30,31,30,31,31,30,31,30]
  Month =  FIX(STRMID(Date,2,2))
  Year  = FIX(STRMID(Date,0,2))
  Day     = FIX(STRMID(Date,4,2))
  DOY     = TOTAL(MD(0:Month-1))+Day
END

PRO RUNMSISE90  ,GEOLAT, GEOLONG,DAY,HOUR,ALTRES,ATMOSPHERE
  DATA   =  FLTARR(4,1)
  ATMOSPHERE =  FLTARR(4,15000)
  FIRSTPOINT =  5
  DayOfYears =  FIX(DAY)
  Flux   =  150.0
  Seconds     = FIX(Hour*3600)
  OMEGA  =  7.292e-5
  GET_LUN     , LUN
  OPENW  ,  LUN,'c:\mcs\model\msisi.in'
  PRINTF   , LUN,DayOfYears
  PRINTF   , LUN,0,0,Seconds
  PRINTF   , LUN,0,0,0
  PRINTF   , LUN,0,0,0
```

```
  PRINTF    , LUN,'kman'
  PRINTF    , LUN,'1.46 300',AltRes
  PRINTF    , LUN,GeoLat,GeoLong
  PRINTF    , LUN,Flux,Flux
  PRINTF    , LUN,' 4 0 0 0 0 0 0'
  PRINTF    , LUN,'000 000'
  PRINTF    , LUN,'msisi.out'
  PRINTF    , LUN,'000'
  CLOSE  ,  LUN
  FREE_LUN  , LUN
  CD        , 'c:\mcs\model\'
  SPAWN  ,   'Msisi.exe',/hide
  ON_ERROR  , 1
  GET_LUN     , LUN
  OPENR  ,   LUN,'c:\mcs\model\msisi.out'
  POINT_LUN  ,   LUN,FirstPoint
  PRINT  ,   'Accessing the Model Information'
  j     = 0
  WHILE NOT EOF(LUN) DO BEGIN
    READF ,   LUN,DATA
    ATMOSPHERE(*,j)  =DATA
    j=j+1
  ENDWHILE
  CLOSE     , LUN
  FREE_LUN    ,   LUN
  Atmosphere    = Atmosphere(*,0,j-1)
END

Pro RayleighError  ,Data,RayleighTimes,add,AvgBins,CntError,PctError
                   ,Signal,AvgSignal,altprof,BKLO,BKHI
  ;-------------------------------------------------------------
  ;-------------------------------------------------------------
  Length          =     (Size(Data))(2)
  Width           =     (Size(Data))(1)
  Twidth          =     (Size(RayleighTimes))(1)
  Background      =     FLTARR(Width)
  SignalError     =     FLTARR(Width,Length)
  CntError        =     FLTARR(TWidth,Length)
  Signal          =     FLTARR(Width,Length)
  PctError        =     FLTARR(TWidth,Length)
  AvgSignal       =     FLTARR(TWidth,Length)
  AvgRayleigh     =     FLTARR(TWidth,Length)
  AvgBackground   =     FLTARR(Twidth)
  Temp            =     FLTARR(Length)
  Temp2           =     0.0
```

```
    FOR i=0,Width-1 DO BEGIN
        Background(i) =     TOTAL(DATA(i,BKLO:BKHI))/(BKHI-BKLO+1.0)
        Signal(i,*)   =     Data(i,*)-Background(i)
    ENDFOR
    FOR i=0,Twidth-1 DO BEGIN
        a     =     rayleightimes(i,0)
        b     =     rayleightimes(i,1)
        c     =     rayleightimes(i,2)
        temp(*)=    0.0
        temp2 =     0.0
        k     =  0
        FOR l=a,b do begin
            IF ((signal(l,1100) GE 60.0) AND (background(l) LT 20)) THEN BEGIN
                temp(*)=    temp(*)+data(l,*)
                temp2 =     temp2+background(l)
                k     =     k+1.0
            ENDIF
        ENDFOR
        Rayleightimes(i,2)          =     c
        AvgSignal(i,*)      =     Temp(*)/k
        AvgBackground(i)    =     temp2/k
        IF (i EQ (twidth-1)) Then begin
            AvgSignal(i,*)          =     AvgSignal(i,*)+add
            AvgBackground(i)        =     AvgBackground(i)+add
        ENDIF
        AvgSignal(i,1120:14004)     =     Smooth(AvgSignal(i,1120:14004)
                                          Avgbins,/edge_truncate)
        Cnterror(i,*)           =     AvgSignal(i,*)/(Avgbins*k)+
                                      AvgBackground(i)/(k*(BKHI-BKLO+1.0))
        AvgSignal(i,*)          =     AvgSignal(i,*)-AvgBackground(i)
        Pcterror(i,*)           =     SQRT(Cnterror(i,*))/AvgSignal(i,*)
    ENDFOR
    RETURN
END

PRO CALCULATEDENSITY ,Rayleigh,Altprof,Fitbin,Density,Altres
        SumLength =   (SIZE(Rayleigh))(2)
        SumWidth  = (SIZE(Rayleigh))(1)
        DENSITY     = FLTARR(SumWidth,SumLength)
        Range  =  findgen(sumlength)*Altres+Altres/2.0
        FOR i=0, SumWidth-1 DO BEGIN
                Density(i,*) =   Rayleigh(i,*)*range(*)*range(*)
                Density(i,*)  =  Density(i,*)/Density(i,Fitbin)
        ENDFOR
END
```

```
PRO GRAVITY      ,GEOLAT,GEOLONG,LENGTH,ALTRES,GNEW
      ,-----------------------
      gm          =     3986004.418e8
      omega       =     7292115.0e-11
      a           =     6378137.0
      b           =     6356752.3142
      e           =     8.1819190842622e-2
      EE          =     5.2185400842339e5
      k           =     0.00193185265241
      m           =     0.00344978650684
      f           =     1/298.257223563
      gge         =     9.7803253359
      ggp         =     9.8321849378
      phi         =     GeoLat*!DTOR
      si          =     atan(((1-f)^2)*tan(phi))
      lambda      =     GeoLong*!DTOR
      alpha       =     phi-si
      ho          =     1460
      N           =     a/sqrt(1-e*e*sin(phi)*sin(phi))
      gnew        =     fltarr(length)
      FOR i=0, length-1 DO BEGIN
            h     =     1460+altres*1000.0*i
            x     =     (N+h)*cos(phi)*cos(lambda)
            y     =     (N+h)*cos(phi)*sin(lambda)
            z     =     ((b*b)/(a*a)*N+h)*sin(phi)
            u     =     sqrt((1.0/2.0)*(x*x+y*y+z*z-
            EE*EE)*(1.0+sqrt(1.0+4.0*EE*EE*z*z/(x*x+y*y+z*z-EE*EE)^2)))
            beta  =     atan(z*sqrt(u*u+EE*EE)/(u*sqrt(x*x+y*y)))
            w           =     sqrt((u*u+EE*EE*sin(beta)*sin(beta))
                              /(u*u+EE*EE))
            q           =     (1.0/2.0)*((1.0+3.0*u*u/(ee*ee))
                              *atan(EE/u)-3.0*u/EE)
            qo          =     (1.0/2.0)*((1.0+3.0*b*b/(ee*ee))
                              *atan(EE/b)-3.0*b/EE)
            qp          =     3.0*(1.0+u*u/(ee*ee))
                              *(1.0-u/ee*atan(ee/u))-1.0
            gu          =     (-1.0/w)*(gm/(u*u+ee*ee)
                        +(omega*omega*a*a*ee*qp)
                        /((u*u+ee*ee)*qo)*(1.0/2.0*sin(beta)*sin(beta)-
                        1.0/6.0))+omega*omega*u*cos(beta)*cos(beta)/w
            gb          =     (1/w)*(omega*omega*a*a*q)
                        /(sqrt(u*u+ee*ee)*qo)*sin(beta)*cos(beta)-
                        omega*omega*sqrt(u*u+ee*ee)*sin(beta)*cos(beta)/w
            gae         =     [gu,gb,0]
            R2          =     [[cos(phi)*cos(lambda),cos(phi)
```

```
                        *sin(lambda),sin(phi)] [-sin(phi)*cos(lambda),-
                        sin(phi)*sin(lambda),cos(phi)] [-
                        sin(lambda),cos(lambda),0]]
            R1          =[[u*cos(beta)*cos(lambda)
                        /(w*sqrt(u^2+EE^2)),-1/w*sin(beta)*cos(lambda),-
                        sin(lambda)], [u*cos(beta)*sin(lambda)/
                        (w*sqrt(u^2+EE^2)),-1/w*sin(beta)*sin(lambda),
                        cos(lambda)] [sin(beta)/w,u*cos(beta)
                        /(w*sqrt(u^2+EE^2)),0]]
            gs          =       R2#(R1#gae)
            gphi        =       -gs(0)*sin(alpha)+gs(1)*cos(alpha)
            gh          =       -gs(0)*cos(alpha)+gs(1)*sin(alpha)
            gnew(i)     =       sqrt(gh^2+gphi^2)
        ENDFOR
        gnew=smooth(gnew,81)    ;smoothing is to match that done in the data
END

PRO TopCalculation ,TavgCntError,PCTERR,TavgRayleigh,Threshold,DOY,
            AltProf,Atmosphere,Topbin,TopTemp,rayleightimes,timeprofiles
        ;----------------------------------------
        Length      =       (Size(TavgCntError))(2)
        Width       =       (Size(TavgCntError))(1)
        TopBin      =       FLTARR(Width)
        TopTemp     =       FLTARR(Width)
        Restore,'c:\mcs\programs\lidar project\sodium.sav'
        XX      =       [-16,15,46,74,105,135,166,196,227,258,288,319,349,380]
        FOR i=0, Width-1 DO BEGIN
            FOR Start=1500,2350 DO BEGIN
                Error       =       Total(PctErr(i,Start-5:Start+5))/11.0
                Topbin(i)   =       Start
                IF  (Error GE Threshold) THEN BEGIN
                    Start   =       2350
                ENDIF
            ENDFOR
            High    =       AltProf(Topbin(i))
            IF (High LT 83) THEN BEGIN
                Below       =       105-FIX(High)
            IF (Below GT 22) THEN Below=22
                Above       =       Below-1
                Ydown       = [SheTemp(12,Below),SheTemp(1:12,Below)
                              ,SheTemp(1,Below)]
                NaTemp      =       SPLINE(XX,YDOWN,DOY,0.1)
                Temp1       =       Atmosphere(2,2175)
                Temp2       =       Atmosphere(2,TopBin(i))
                TopTemp(i)  =       NaTemp-(Temp1-Temp2)
```

```
            ENDIF ELSE BEGIN
                  Below       =     105-FIX(High)
                  IF (BELOW GT 22) THEN BELOW=22
                  Above =     Below-1
                  Yup   = [SheTemp(12,Above),SheTemp(1:12,Above)
                        ,SheTemp(1,Above)]
                  YDown= [SheTemp(12,Below),SheTemp(1:12,Below)
                        ,SheTemp(1,Below)]
                  TempLow     =     SPLINE(XX,YDown,DOY,0.1)
                  TempHigh    =     SPLINE(XX,YUp,DOY,0.1)
                  P           =     [TempLow,TempHigh]
                  LL          =     [SheTemp(0,Below),
                                    SheTemp(0,Above)]
                  NaTemp      =     Interpol(P,LL,High)
                  TopTemp(i)  =     NaTemp
            ENDELSE
   ENDFOR
   RETURN
END

PRO TempCalculation ,Altprof,Density,Gnew,MMM,RRR,Altres,
                  TopBin,TopTemp,Temperature
      ;-------------------------------------------------------------------------
      Length      =     (Size(Density))(2)
      Width       =     (Size(Density))(1)
      Temperature =     FLTARR(Width,Length)
      FOR i=0, Width-1 DO BEGIN
            C1    =     Density(i,Topbin(i))/Density(i,*)
            C2    =     TopTemp(i)
            C3    =     Altres/(2.0*RRR*Density(i,Topbin(i)))
            Upper =     MMM*Gnew(Topbin(i))*Density(i,Topbin(i))*C3
            Integral=   Double(0.0)
            FOR  j=Topbin(i)-1,1160,-1 DO BEGIN
                  Lower       =     MMM*GNEW(j)*Density(i,j)*C3
                  Integral    =     Integral+Upper+Lower
                  Temperature(i,j)  =  C1(j)*(C2+Integral)
                  Upper       =     Lower
            ENDFOR
      ENDFOR
      RETURN
END

Pro TempErrors      ,Temperature,Altprof,TavgPctErr,Topbin,TempErr
      ;-----------------------------------------------------
      Length      =     (Size(Temperature))(2)
```

```
        Width       =       (Size(Temperature))(1)
        TempErr     =       FLTARR(Width,Length)
        FOR i=0, Width-1 DO BEGIN
                FOR j=Topbin(i),1000,-1 DO BEGIN
                        TempErr(i,j)= Temperature(i,j)^2.0*TavgPctErr(i,j)^2.0
                        +Temperature(i,TopBin(i))2*TavgPctErr(i,Topbin(i))^(2.0)
                        *EXP(-2.0*(AltProf(TopBin(i))-AltProf(j))/7.0)
                        TempErr(i,j)  =       SQRT(TempErr(i,j))
                ENDFOR
        ENDFOR
        RETURN
END

Pro Day_31_average
        ;--------------------
        ; This is a program to average the nightly data into 31 day averages
        ; This program accesses a list of good/bad nights
        ; It may require that some listings be reworked to accound for a lower altitude
        ;--------------------
        Month       =       ['01','02','03','04','05','06','07','08','09','10','11','12']
        Get_lun,Lun1
        OPENR,Lun1,'c:\work\sav\goodfiles.txt'
        Line        =       ''
        Chk1        =       ''
        Chk2        =       ''
        Length      =       14005
        Altres      =       0.0375
        Geolat      =       41.742
        Geolong     =       241.19
        MMM         =       28.9415
        RRR         =       8.31432
        Avgbins     =       81
        Add         =       0.0
        Check       =       STRARR(7,1000)
        YearAvg     =       FLTARR(365,5,3000)
        Altprof     =       findgen(3000)*0.0375+1.46+0.0375/2.0
        yearavg(*,*,*)=!values.f_nan
        j           =       0
        WHILE NOT EOF(LUN1) DO BEGIN
                READF, LUN1, Line
                CHK1 =   STRMID(Line, 36)
                Check(0,j)=Line
                Check(1,j)=STRMID(Line,21,6)
                Check(2,j)=STRMID(Line,36,4)
                j=j+1
```

```
ENDWHILE
close, lun1
free_lun, lun1
Check =  Check(*,0:j-1)
;-----------------
; This section of code double checks the database and what is included
redo  = ''
Print, 'Do you wish to review the data?'
Read, redo
IF ((redo eq 'Y') or (redo eq 'y')) THEN BEGIN
        R2      =       ''
        Print, 'Do you wish to restart from the last point?'
        Read, r2
        IF ((r2 eq 'y') or (r2 eq 'Y')) then restore, 'c:\work\sav\newlist2.sav'
        jump=i-5
        NightNumber  = j    ; Number of nights in database
        Window, 1, xsize=900,ysize=800
        !P.Multi=[0,3,1]
        FOR i=850, NightNumber-1 DO BEGIN
                Filename1='c:\work\sav\'+check(1,i)+'short.dat'
                result=file_search(filename1)
                    IF (result eq filename1) THEN BEGIN
                            restore, filename1
                            NHours  =  (Size(Temperature))(1)
                            IF (check(5,i) eq '0.0') THEN Check(5,i)='45'
                            IF (check(4,i) eq '0.0') THEN Check(4,i)='95'
                            IF (check(4,i) eq '') THEN Check(4,i)='94'
                            IF (check(5,i) eq '') THEN Check(5,i)='45'
                            Min1=(Fix(Check(5,i))-1.46-0.0375/2.0)/0.0375
                            Max1=(Fix(Check(4,i))-1.46-0.0375/2.0)/0.0375
                            Savg = FLTARR(length)
                                FOR j=0,Length-1 DO BEGIN
                                    Savg(j)=mean(Data(*,j))
                                ENDFOR
                            Savg(1050:14004)=Smooth(Savg(1050:14004),81)
                            xyouts,100,200,check(4,i)
                            xyouts,100,180,check(5,i)
                            xyouts,100,160,check(3,i)
                            xyouts,100,140,check(2,i)
                            a1=''
                            a0=''
                            a2=''
                            Print, 'Do you think this is a good night'
                            READ,a1
                            IF ((a1 eq 'Y') or (a1 eq 'y')) THEN BEGIN
```

```
                        check(3,i) =  'Good'
                        Print, 'Do you whish to change the max alt?'
                        read, a0
                        Check(4,i) ='95'
                        IF ((a0 eq 'y') or (a0 eq 'Y')) Then begin
                        Print, What is new max alt?'
                        read,a1
                        check(4,i)   = a1
                    ENDIF
                    Check(5,i) =  '45'
                    Print, 'Do you wish to change the min alt?'
                    Read, a1
                    IF ((a1 eq 'y') or (a1 eq 'Y')) Then begin
                        Print, 'What is the new min alt?'
                        read, a2
                        Check(5,i)=a2
                    ENDIF
                ENDIF ELSE BEGIN
                    Check(3,i) =  'Bad'
                    Check(4,i) =  '95'
                    Check(5,i) =  '45'
                ENDELSE
                Save, Check,i, Filename='c:\work\sav\newlist2.sav'
            ENDIF
        ENDFOR
ENDIF ELSE BEGIN
        restore, 'c:\work\sav\newlist2.sav'
ENDELSE
;------------------
;------------------
TestDOY   = ''
Print, 'Do you wish to redo the DOY calculations?'
READ, TestDOY
testdoy='y'
NumDays   = (size(check))(2)
IF ((TestDOY eq 'y') or (TestDOY eq 'Y')) THEN BEGIN
        FOR i=0, NumDays-1 DO BEGIN
            NightDay    = STRMID(Check(1,i),4,2)
            NightMonth  = STRMID(Check(1,i),2,2)
            NightYear   = STRMID(Check(1,i),0,2)
            IF (NightYear eq '96') THEN NightYear='1996'
            IF (NightYear eq '95') THEN NightYear='1995'
            IF (NightYear eq '94') THEN NightYear='1994'
            IF (NightYear eq '93') THEN NightYear='1993'
            IF (NightYear eq '97') THEN NightYear='1997'
```

```
                IF (NightYear eq '98') THEN NightYear='1998'
                IF (NightYear eq '99') THEN NightYear='1999'
                IF (NightYear eq '00') THEN NightYear='2000'
                IF (NightYear eq '01') THEN NightYear='2001'
                IF (NightYear eq '02') THEN NightYear='2002'
                IF (NightYear eq '03') THEN NightYear='2003'
                IF (NightYear eq '04') THEN NightYear='2004'
                IF (NightYear eq '05') THEN NightYear='2005'
                NightMonth    = FIX(NightMonth)
                NightYear     = FIX(NightMonth)
                NightDay      =  FIX(NightDay)
                Check(6,i)    = JULDAY(NightMonth,NightDay,NightYear)-
                                JULDAY(1,1,NightYear)+1
                Print, Check(1,i),Check(6,i)
        ENDFOR
        save, check,filename='c:\work\sav\newlist2.sav'
ENDIF
;------------------
;This section of the code will re-do the temperatures taking
;into account the new minimum and maximum altitudes.
;------------------
ch12=''
Print, 'Do you with to redo the nights with changed altitudes?'
read, ch12
IF ((ch12 eq 'y') or (ch12 eq 'Y')) THEN BEGIN
        FOR zz=0, NumDays-1 DO BEGIN
                print, zz,' ',Check(1,zz), ' Is good'
                Restore, 'c:\work\sav\'+check(1,zz)+'.dat'
                NewTop = (Fix(Check(4,zz))-1.46-0.0375/2.0)/0.0375
                NewBottom  =(Fix(Check(5,zz))-1.46-0.0375/2.0)/0.0375
                TempDay =  STRMID(check(1,zz),4,2)
                TempMonth  = STRMID(check(1,zz),2,2)
                TempYear   = STRMID(check(1,zz),0,2)
                Nighthour=(size(temperature))(1)
                IF (NewTop LT Topbin(Nighthour-1) and (fix(check(4,zz))
                        LT 88.5)) THEN BEGIN
                        Topbin(nighthour-1)=NewTop
                        NEWTOPS,Check(6,zz),Check(4,zz),NewTemp
                        TopTemp(nighthour-1)=NewTemp
                        RayleighError, Data,Rayleightimes,add,avgbins,$
                        cnterror,pcterror,signal,avgsignal,altprof,bklo,bkhi
                        CalculateDensity, AvgSignal,Altres,Density
                        Gravity, Geolat, Geolong,Length,Altres,Gnew
                        Tempcalculation, altprof,density,gnew,mmm,rrr,$
                        altres,topbin,toptemp,temperature
```

```
                ENDIF
                file  = 'c:\work\sav\'+check(1,zz)+'short.dat'
                save, temperature, temperr,topbin,toptemp,filename=file
        ENDFOR
        print, 'end of data redo'
ENDIF
Print, 'Do you wish to redo thenights with MSIS as the start altitude?'
ch14=''
READ, ch14
IF ((ch14 eq 'y') or (ch14 eq 'Y')) THEN BEGIN
        FOR zz=0, NumDays-1 DO BEGIN
                restore, 'c:\work\sav\'+check(1,zz)+'.dat'
                Nighthour=(size(temperature))(1)
                NewTop=(Fix(check(4,zz))-1.46-0.0375/2.0)/0.0375
                IF (NewTop LT Topbin(Nighthour-1) and (fix(check(4,zz))
                LT 88.5)) THEN BEGIN
                        Print, 'We have lowered the starting altitude'
                ENDIF ELSE BEGIN
                        Newtop=Topbin(nighthour-1)
                ENDELSE
                NewBottom  =(Fix(Check(5,zz))-1.46-0.0375/2.0)/0.0375
                TempDay =  STRMID(check(1,zz),4,2)
                TempMonth  = STRMID(check(1,zz),2,2)
                TempYear   = STRMID(check(1,zz),0,2)
                l2  =  (size(headers))(1)-1
                hourstart  = fix(strmid(headers(0,4),18,2))
                        +(fix(strmid(headers(0,4),24,2))/60.0
                        +fix(strmid(headers(0,4),21,2)))/60.0
                hourend =  fix(strmid(headers(l2,4),18,2))
                        +(fix(strmid(headers(l2,4),24,2))/6.0
                        +fix(strmid(headers(l2,4),21,2)))/60.0
                hour     = fix((hourend-hourstart)+hourstart)
                Nighthour  = (size(temperature))(1)
                Topbin(nighthour-1)=NewTop
                day=check(6,zz)
                RUNMSISe00,Geolat,Geolong,Day,Hour,Altres,Atmosphere
                file_delete, 'b:\msisi.out'
                Newtemp=Atmosphere(2,Newtop)
                Toptemp(nighthour-1)=NewTemp
                RayleighError,Data,Rayleightimes,add,avgbins,cnterror,
                pcterror,signal,avgsignal,altprof,bklo,bkhi
                CalculateDensity, AvgSignal,Altres,Density
                Gravity, Geolat,Geolong,Length,Altres,Gnew
                Tempcalculation, altprof,density,gnew,mmm,rrr,alters
                ,topbin,toptemp,temperature
```

```
                file='c:\work\sav\'+check(1,zz)+'msis.dat'
                save,temperature, temperr,topbin,toptemp,filename=file
        ENDFOR
ENDIF
;------------------
;this section opens each day of data and copies out the night-time average
;------------------
ch123=''
Print, 'Do you wish to re-read the nightly averaged?'
READ, Ch123
numnights=0
numdata=0
IF ((ch123 eq 'y') or (ch123 eq 'Y')) then begin
        NightlyData=FLTARR(Numdays,2,3000)
        NightlyTime=strARR(Numdays,2)
        NightlyData(*,*,*)=!values.f_nan
        For i=0, NumDays-1 DO BEGIN
                IF ((Check(2,i) eq 'Good') or (Check(2,i) eq 'good')) THEN
                BEGIN
                        numnights=numnights+1
                        numdata=numdata+(size(data))(1)
                        restore, 'c:\work\sav\'+check(1,i)+'.dat'
                        Numhours=(size(temperature))(1)
                        IF (fix(Check(5,i)) LT 45) then Check(5,i)='45'
                        IF (check(4,i) eq '') then Check(4,i)='95'
                        Min1    =(Fix(Check(5,i))-1.46-0.0375/2.0)/0.0375
                        Max1    =(Fix(Check(4,i))-1.46-0.0375/2.0)/0.0375
                        NightlyData(i,0,Min1:(Topbin(numhours-1)-1))=
                                        Temperature((Numhours-
                                        1),min1:(Topbin(numhours-1)-1))
                        NightlyDAta(i,1,Min1:(Topbin(numhours-1)-1))=
                                        Temperr((Numhours-1)
                                        ,min1:(Topbin(numhours-1)-1))
                        NightlyTime(i,0)=headers(0,4)
                        endtime=(size(headers))(1)
                        NightlyTime(i,1)=headers(endtime-1,4)
                        print, strmid(headers(0,4),18,6),
                                strmid(headers(endtime-1,4),18,6)
                ENDIF
        ENDFOR
        save,nightlydata,nightlytime,filename='c:\work\sav\nightlydataold.sav'
ENDIF
;------------------
check3=''
Print, 'Do you wish to recalucate the year averages?'
```

```
read,check3
get_lun, lun9
openw,lun9,'c:\work\sav\altsout.txt'
IF ((check3 eq 'y') or (check3 eq 'Y')) THEN BEGIN
        NumDatabase=(size(check))(2)
        restore, 'c:\work\sav\nightlydataold.sav'
        FOR DOY=1,365 DO BEGIN
                StartDay = DOY-15
                EndDay  = DOY+15
                IF (StartDay LT 1) THEN StartDay=StartDay+365
                IF (EndDay GT 365) THEN EndDay=EndDay-365
                Print, StartDay,'-',DOY,'-',EndDay
                MonAvg=FLTARR(200,3000)
                MonAvg(*,*)=!values.f_nan
                MonAvgE=FLTARR(200,3000)
                MonAvgE(*,*)=!values.f_nan
                AvgIndex=0
                i=0
                FOR i=0,NumDatabase-1 DO BEGIN
                        Include='n'
                        DOYINT =   FIX(Check(6,i))
                        IF ((DOY GE 16) AND (DOY LT 351)) THEN BEGIN
                                IF ((DOYINT GE StartDay) and
                                (DOYINT LE EndDay)) THEN Include='y'
                                ENDIF
                        IF (DOY GT 350) THEN BEGIN
                                IF (DOYINT GE StartDay) THEN Include='y'
                                IF (DOYINT LT EndDay) THEN Include='y'
                        ENDIF
                        IF (DOY LT 16) THEN BEGIN
                                IF (DOYINT LE EndDay) THEN Include='y'
                                IF (DOYINT GE StartDay) THEN Include='y'
                        ENDIF
                        IF (check(3,i) eq 'Bad') then Include='n'
                        IF (Include eq 'y') THEN Begin
                                file1=check(1,i)
                                MonAvg(AvgIndex,0:2999)=
                                        Nightlydata(i,0,0:2999)
                                MonAvgE(AvgIndex,0:2999)=
                                        Nightlydata(i,1,0:2999)
                                AvgIndex=AvgIndex+1
                                IF (Check(5,i) GT 45) THEN BEGIN
                                        IF (fix(check(4,i)) LT 45)
                                        Then check(4,i)='45'
                                        minbin=((fix(check(4,i))-1.46
```

```
                                -0.0375/2.0)/0.0375)
                        Monavg(avgIndex,0:minbin)=
                                !values.f_nan
                        monavge(avgindex,0:minbin)=
                                !values.f_nan
                ENDIF
        ENDIF
ENDFOR
MonAvg=Monavg(0:AvgIndex-1,*)
nn=fltarr(3000)
FOR ll=0,2999 DO BEGIN
        avgnum=0
        FOR index2=0,avgindex-1 Do begin
                IF (finite(monavg(index2,ll))) then avgnum=
                avgnum+1
        ENDFOR
        nn(ll)=avgnum
ENDFOR
switch1=0
switch2=0
For ll=2999,0,-1 Do begin
        maxnum=fix(max(nn)/2.0)
        IF (switch1 eq 0) THEN BEGIN
                IF (nn(ll) GT 0) THEN BEGIN
                        talt=altprof(ll)
                        switch1=1
                ENDIF
        ENDIF
        IF (switch2 eq 0) THEN BEGIN
                IF (nn(ll) eq maxnum) THEN BEGIN
                        Endbin=ll
                        malt=altprof(ll)
                        switch2=1
                ENDIF
        ENDIF
        IF (nn(ll) GE maxnum*2) THEN BEGIN
                balt=altprof(ll)
                break
        ENDIF
ENDFOR
printf, lun9,doy, talt,malt,balt
FOR ll=0,Endbin DO BEGIN
        avgnum=0
        FOR index2=0,AvgIndex-1 do begin
                if (finite(monavg(index2,ll))) then avgnum=
```

```
                    avgnum+1
                ENDFOR
                YearAvg(DOY-1,0,ll)=mean(MonAvg(*,ll),/nan)
                YearAvg(DOY-1,1,ll)=mean(Monavg(*,ll),/nan)
                /sqrt(avgnum)
                YearAvg(DOY-1,3,ll)=Avgnum
                IF (avgnum GE 2) THEN YearAvg(DOY-1,2,ll)-
                stddev(monavg(*,ll),/nan)
            ENDFOR
            altprof=findgen(3000)*0.0375+1.46+0.0375/2.0
            max1=Endbin
            min1=(45.0-1.46-0.0375/2.0)/0.0375
        ENDFOR
        close, lun9
        free_lun, lun9
        save,yearavg,filename='c:\work\sav\yearavgold.sav'
ENDIF
;------------------
check4=''
Print, 'Do you wish to review the nightly data against the yearly average?'
read, check4
IF ((check4 eq 'y') or (check4 eq 'Y')) THEN BEGIN
        numbernights=(size(check))(2)
        restore, 'c:\work\sav\nightlydata072202.sav'
        restore, 'c:\work\sav\yearavg072202.sav'
        altprof=findgen(3000)*0.0375+1.46+0.0375/2.0
FOR i=230,numbernights-1 do begin
        jump3:
        tempdoy=Fix(check(6,i))
        max1=(fix(check(4,i))-1.46-0.0375/2.0)/0.0375
        min1=(fix(check(5,i))-1.46-0.0375/2.0)/0.0375
        IF (min1 LT 1160) then Min1=1160
        IF (tempdoy GT 365) then tempdoy=365
        IF (max1 LT 1160) then max1=1161
        Print, 'Do you wish to change anything about this night?'
        check9=''
        read,check9
        IF ((check9 eq 'Y') or (check9 eq 'y')) THEN BEGIN
                check8=''
                inone=''
                Print, 'Do you think this is a good night?'
                read, inone
                IF ((inone eq 'y') or (inone eq 'Y')) THEN BEGIN
                        Check(3,i)='Good'
                        Save, Check, Filename='c:\work\sav\newlist2.sav'
```

```
ENDIF
IF ((inone eq 'n') or (inone eq 'N')) THEN BEGIN
        Check(3,i)='Bad'
        Save, Check, Filename='c:\work\sav\newlist2.sav'
ENDIF
Print, 'Do you wish to change the maximum altitude?'
read,check8
IF ((check8 eq 'Y') or (check8 eq 'y')) THEN BEGIN
        Print, 'What do you think is the appropriate max alt?'
        read,a1
        check(4,i)    =  a1
        Save, Check, Filename='c:\work\sav\newlist2.sav'
        max1=(fix(check(4,i))-1.46-0.0375/2.0)/0.0375
ENDIF
Print, 'Do you wish to change the minimum altitude?'
read, check8
IF ((check8 eq 'Y') or (check8 eq 'y')) THEN BEGIN
        Print, 'What do you think is the appropriate min alt?'
        read, a1
        check(5,i) =  a1
        Save, Check, Filename='c:\work\sav\newlist2.sav'
        min1=(fix(check(5,i))-1.46-0.0375/2.0)/0.0375
ENDIF
;----------
print, i,'  ',Check(1,i), ' Is good'
Restore, 'c:\work\sav\'+check(1,i)+'.dat'
Restore, 'c:\work\sav\'+check(1,i)+'msis.dat'
NewTop = (Fix(Check(4,i))-1.46-0.0375/2.0)/0.0375
NewBottom  =(Fix(Check(5,i))-1.46-0.0375/2.0)/0.0375
TempDay =  STRMID(check(1,i),4,2)
TempMonth  = STRMID(check(1,i),2,2)
TempYear   = STRMID(check(1,i),0,2)
Nighthour=(size(temperature))(1)
IF (NewTop LT Topbin(Nighthour-1) and
       (fix(check(4,i)) LT 88.5)) THEN
       Topbin(nighthour-1)=NewTop
IF (Check(4,i) NE '95') THEN Topbin(nighthour-1)=NewTop
Hour=7
Day=fix(Check(6,i))
RUNMSISe00,Geolat,Geolong,Day,Hour,Altres,Atmosphere
NewTemp=Atmosphere(2,Topbin(nighthour-1))
TopTemp(nighthour-1)=NewTemp
RayleighError2,data,Rayleightimes,add,avgbins,cnterror
       ,pcterror,signal,avgsignal,altprof,bklo,bkhi
CalculateDensity, AvgSignal,Altres,Density
```

```
                    Gravity, Geolat, Geolong,Length,Altres,Gnew
                    Tempcalculation, altprof,density,gnew,mmm,rrr,alters
                          ,topbin,toptemp,temperature
                    file   = 'c:\work\sav\'+check(1,i)+'msis.dat'
                    save, temperature, density, temperr,altprof,topbin,toptemp
                          ,headers,date,data,rayleightimes,bkhi,bklo,timestamp
                          ,filename=file
                    nightlydata(i,0,*)=!values.f_nan
                    nightlydata(i,0,min1:(topbin(nighthour-1)-1))=
                          Temperature(nighthour-1,min1:(topbin(nighthour-1)-1))
                    nightlydata(i,1,min1:(topbin(nighthour-1)-1))=
                          temperr(nighthour-1,min1:(topbin(nighthour-1)-1))
                    goto, jump3
                    ;----------
                    ENDIF
      ENDFOR
      Save, Check,i, Filename='c:\work\sav\newlist2.sav'
      ENDIF
      ;--------------------
      Print, 'End of Line'
End
```

CURRICULUM VITAE

Curriculum Vitae
Joshua P. Herron
232 Sunstone Circle
Logan, UT 94321
Work: 435-797-3350
Cell: 435-755-5763
Email: jpherron@comcast.net

1) Professional Preparation

Undergraduate Institutions	**Major**	**Degree & Year**
Brigham Young University Idaho	Physics	AS Science 1997
Utah State University	Physics	BS Physics 1999

Graduate Institution(s)	**Major**	**Degree & Year**
Utah State University	Physics	MS Physics 2004
Utah State University	Physics	PhD Physics 2007

2) Employment

Research Assistant	Utah State University	2000 to 2006
Teaching Assistant	Utah State University	2000 to 2005

3) Teaching Experience

Teaching Assistant	Physics 2100 & 2200	2000 to 2005
Instructor	Physics 2220	Summer 2005

4) Honors, Awards

Fellowship	Rocky Mountain NASA Space Grant	2002 to 2005
Recipient	Outstanding Student Presentation (Fall AGU)	2005

5) Membership

American Geophysical Union

6) Publications

Herron, J. P., V. B. Wickwar, P. J. Espy, and J. W. Meriwether (2007), Observations of a Noctilucent Cloud above Logan, Utah (41.7 N, 111.8 W) in 1995, *J. Geophys Res.*, in press, doi: 10.1029/2006JD007158.

Herron, J. P., and V. B. Wickwar (2007), Temperature climatology above logan UT from Rayleigh-scatter lidar, *J. Atmos. Solar Terr. Phys.*, (to be submitted).

Herron, J. P., and V. Wickwar (2007), A comparison of mid-latitude mesospheric temperatures: the ALO lidar climatology and the NRL MSIS empirical model, *J. Geophys. Res.*, (to be submitted).

Herron, J. P. (2004), Mesospheric Temperature Climatology Above Utah State University, M.S. Thesis, 156 pp, Utah State University, Logan, Utah.

Wickwar, V. B., M. J. Taylor, J. P. Herron, and B. A. Martineau (2002), Visual and lidar observations of noctilucent clouds above Logan, Utah, at 41.7°N, *J. Geophys. Res.*, *107*(D7), 10.1029/2001JD002280,

Wickwar, V. B., T. D. Wilkerson, M. Hammond, and J. P. Herron (2001), Mesospheric temperature observations at the USU / CASS Atmospheric Lidar Observatory (ALO), paper presented at Remote Sensing of the Atmosphere, Environment, and Space, Proceedings of SPIE.

Shepherd, M. G., B. Prawirosoehardjo, S. Zhang, B. H. Solheim, G. G. Shepherd, V. B. Wickwar, and J. P. Herron (2001), Retrieval and validation of mesospheric temperatures from WINDII observations, *J. Geophys. Res.*, *104*(A11), 24813-24829, doi: 10.1029/2000JA000323.

7) Synergistic Activities

Made significant contributions to the development of the upgraded USU Rayleigh lidar. Responsibilities included the selection, purchase, testing and calibration of many of the opto-mechanical components.

Developed the data analysis routines used by the ALO lidar group. A direct result of this effort was the analysis of over 11 years of lidar data and the development of a database of lidar observations from ALO.

Due to the highly visible nature of Rayleigh lidar, considerable public interest in the research exists. I was responsible for giving guided tours of the lidar facility in addition to presentation of the research to the general public.

The operation of the Rayleigh lidar is conducted by undergraduate students. I was responsible for their training to operate the lidar. In addition to basic training I assisted several undergraduates with their senior research projects that involved some aspect of research with the lidar.